STABILITY, DYNAMICS AND CHANGE-OF-STATE IN LIQUID DROP-BRIDGE SYSTEMS

A Dissertation

Presented to the Faculty of the Graduate School

of Cornell University

in Partial Fulfillment of the Requirements for the Degree of

Doctor of Philosophy

by

Henrik Bernhard van Lengerich

May 2011

STABILITY, DYNAMICS AND CHANGE-OF-STATE IN LIQUID DROP-BRIDGE SYSTEMS

Henrik Bernhard van Lengerich, Ph.D.

Cornell University 2011

A capillary based adhesion device motivates the study of coupled free-interface shapes and the transition from the drop to bridge shape. When a large number of drops, pinned at circular contact lines, are touched to a surface they form liquid bridges, and these bridges create an adhesive force. Alternatively, if the drops are not brought to the surface quickly enough the drops will coarsen, forming instead one large drop.

Consider first the coarsening process. The dissipation occurs primarily in the conduits, the drop retain their equilibrium shape – the spherical cap. Drops scavenge volume from one another based on pressure differences, proportional to the surface tension, and arising from curvature differences. This process minimizes the total surface energy. All fixed points and their linear stabilities, obtained analytically, are found to be independent of connectivity. The system coarsens in the sense that, with time, volume is increasingly localized and ends up in a single 'winner' drop. To determine which of the stable fixed points will be the winner, manifolds separating the attracting regions are found using a method which combines local information (eigenvectors at fixed points) with global information (invariant manifolds due to symmetry). The coarsening rate is predicted heuristically, with the Lifshitz-Slyozov-Wagner (LSW) model and compared against numerical simulations for a variety of networks. Distributions of large drop volumes from LSW are independent of network topology; in

contrast, simulation results depend weakly on the network dimension.

When a pinned drop touches a solid surface it forms a liquid bridge; here the energy is dissipated within the bridge. The dissipated energy is equal to the loss of surface energy, which can also be expressed in terms of forces along the interface using a geometric relation. This energy balance provides an extra relation which determines the microscopic nature of the contact line. Boundary integral method simulations are used to compute the flow field and viscous bending of the free interface. The energy balance is applied to simulations to find slip lengths. The energy balance is used to bound the microscopic contact angle analytically.

BIOGRAPHICAL SKETCH

Henrik is an ordinary man who spent a lot of time in the office. He graduated from Wayzata High School in 2002 and received a bachelors in chemical engineering from the University of Minnesota in 2005.

ACKNOWLEDGEMENTS

I would like to thank my family for their support. I would also like to thank my friends for the distractions they provide in a world that is otherwise filled with equations.

I received a lot of help early on from Michael Vogel; it was his idea to study the interacting drops and he provided the experimental motivation as well. I learned a lot about experiments and coding from him. I received a lot of help from fellow group members, particularly Brenton Cox, Anthony Altieri and Chun-Ti Chang. Finally, I would like to thank my advisor Paul Steen who has always been enthusiastic about my work.

TABLE OF CONTENTS

1 Liquid drop-bridge systems **1**
- 1.1 Introduction . . . 1
  - 1.1.1 Thermodynamic, mathematical and fluid-dynamics perspective . . . 4
- 1.2 Motivation . . . 6
  - 1.2.1 Engineering applications . . . 6
  - 1.2.2 Scientific and mathematical motivation . . . 8

2 Stability of coupled drops **11**
- 2.1 Introduction . . . 11
- 2.2 The family of dynamical systems . . . 15
  - 2.2.1 Connectivity networks . . . 15
  - 2.2.2 Governing dynamical system . . . 18
- 2.3 Global phase flow, fixed points and their stability . . . 20
  - 2.3.1 Deformation example . . . 26
- 2.4 Generalized gradient systems . . . 27
  - 2.4.1 Proof . . . 28
  - 2.4.2 Remarks on the proof . . . 30
- 2.5 Conclusions . . . 31

3 Volume-Scavenging **33**
- 3.1 Introduction . . . 33
- 3.2 Motivational observations . . . 33
  - 3.2.1 Simulations . . . 33
  - 3.2.2 Probability-of-winning . . . 35
  - 3.2.3 Change-of-winner . . . 35
- 3.3 Domains of attraction . . . 36
  - 3.3.1 Eigenvectors and eigenvalues . . . 38
  - 3.3.2 Symmetry manifolds . . . 38
  - 3.3.3 Separatrix manifolds . . . 40
- 3.4 Explanation of computational results . . . 42
  - 3.4.1 Probability-of-winning . . . 42
  - 3.4.2 Change-of-winner . . . 43
- 3.5 Higher dimensional results . . . 45
  - 3.5.1 No symmetry . . . 46
  - 3.5.2 Some or full symmetry . . . 46
- 3.6 Conclusions . . . 48

4 Coarsening dynamics **51**
4.1 Introduction . . . 51
4.2 Governing Equations . . . 59
4.2.1 Orthogonal networks . . . 59
4.2.2 Porous media . . . 61
4.2.3 Fractal networks . . . 62
4.3 Coarsening Rates: Heuristic predictions and simulation results . . 64
4.3.1 Orthogonal networks: large drop growth . . . 64
4.3.2 Porous medium: large drop growth . . . 66
4.3.3 Orthogonal networks and porous media: prediction and simulation . . . 67
4.3.4 Fractal network: prediction and simulation . . . 71
4.4 Distribution of large drop volumes and self-similar coarsening rates 73
4.5 Discussion and Summary . . . 78

5 Bridge-drop change-of-state **82**
5.1 Introduction . . . 82
5.2 Overview: Spreading bridges and drop-bridge changes-of-state . 86
5.2.1 Rate of energy decay . . . 88
5.2.2 Experiment and computation for pinned contact-lines . . . 91
5.3 Formulation . . . 93
5.4 Energy decay rate . . . 96
5.4.1 Surface energy relation . . . 96
5.4.2 Working of the interface . . . 97
5.4.3 Viscous dissipation . . . 99
5.5 Experiments . . . 101
5.6 Numerical simulations . . . 104
5.6.1 Boundary integral method . . . 104
5.6.2 Microscopic region . . . 106
5.6.3 Slip-length . . . 107
5.7 Simulation results . . . 108
5.7.1 Energy loss due to viscous dissipation . . . 109
5.8 Microscopic contact-angle relation . . . 116
5.9 Relation to Voinov-Hocking-Cox model . . . 119
5.10 Concluding Remarks . . . 121

6 Summary and future Work **126**
6.1 Stability of coupled drops (Chapter 2) . . . 126
6.2 Volume-scavenging (Chapter 3) . . . 127
6.3 Coarsening dynamics (Chapter 4) . . . 127
6.4 Bridge-drop change-of-state (Chapter 5) . . . 128

A Equilibrium and stability using the methods of Weierstrass and Poincare **131**
A.1 Equilibrium minimizing area with a conserved volume 131
A.2 Method of Weierstrass 135
A.2.1 Determinant criterion 135
A.2.2 Relation to turning points 137
A.3 Method of Poincare 139
A.4 Equivalence of Weierstrass and Poincare results 140

B Example of a complete to ring network deformation **144**

C Number of fixed points **145**

D Eigenvalues and eigenvectors of the star configuration **146**

E Flow types in adhesion device **148**

F Reynolds' transport theorem on a surface **150**

G Analytic evaluation of terms in BIM **152**

Bibliography **154**

LIST OF TABLES

3.1 Symmetry manifolds and eigenvalues and eigenvectors of source fixed point for various $N = 3$ networks with conductances given in Section 3.3.2. Eigenvalues are scaled by $-P'(\overline{V})$, where the prime denotes differentiation with respect to volume. Eigenvectors are expressed in triangular reduced space $(x, y) = (V_1 - V_3, \sqrt{3}(V_2 - \overline{V}))$ and $0 \leq \theta \leq \pi$. 40

4.1 Comparison of heuristic and LSW coarsening rates as well as δ values used to fit the data for orthogonal networks (ON), porous media, and fractal networks. LSW predicts a pre-exponential factor of $\delta = 3^3/4^4 \approx 0.105$ for all networks. 77

4.2 Time scales for orthogonal networks (ON), porous media (PM) and fractal networks (FN). 79

5.1 $\dot{\mathcal{A}} = \mathcal{P} = -\mathcal{D}$; equivalent expressions for the rate of energy loss in a system with a moving contact-line. Find derivations in section 5.4 (equation numbers in parenthesis). 90

D.1 Eigenvalues and eigen-directions for a fixed point with n_L large drops in the reduced space ($N - 1$ components). The vector type and the amount (number) of times that type of vector appears are listed. All eigenvectors of a given type have the same eigenvalue. 147

LIST OF FIGURES

1.1 Thermodynamic bridge-drop cycle for a constant length equal to the pinning radius $L = R_0$. 4
1.2 Schematic of capillary adhesion device. Initial condition of drops (Top). Device may coarsen (bottom left) or adhere to substrate (bottom right). 7

2.1 Dynamics of a 4 x 6 array of drops protruding from 500 μm holes sitting above a frit with 4-5.5 μm pore diameter. Elapsed time i = 0s, ii = 2.0 s, iii = 21.3 s iv = 31.9 s. 12
2.2 Dimensionless drop volume V against pressure P (in units of $\tilde{\sigma}/\tilde{B}$. The curve is parametrized by the height of the drop $h = \tilde{H}/\tilde{B}$. 14
2.3 Top: Two drops coupled by a single conduit. Middle: The phase space is 1-dimensional with state variable $(V_2 - V_1)$. The closed circles are stable fixed points and the open circle is unstable. Bottom: Each fixed point corresponds to the arrangement of drops shown schematically. 15
2.4 Various connectivity networks. Numbering convention indicated when necessary. Diagrams can be generalized to arbitrary N. 16
2.5 The fixed points for $N = 4$ arranged in a hierarchy of energy levels with heteroclinic connections indicated (arrows). 22
2.6 A deformation from center drop large to center drop small. Left: The original star network with center drop large (solid lines). The dotted lines are the new connections made. Right: The solid lines that are not used are taken away. The network is now star with a small center drop. The network remains connected throughout the deformation. 27

3.1 Histograms showing the probability for a given drop to win in a linear system for $N = 5, 6, 7, 8$ (as indicated by the abscissa range). The 10,000 initial conditions are uniformly distributed close to the point of identical 1.5 hemispherical drops. 36
3.2 Phase diagram showing which drop wins for a fixed initial disturbance. 37
3.3 Top: Three dimensional phase-space for $\overline{V} > 1$ with branches of fixed points (dashed lines). Bottom: A constant volume slice gives the triangular reduced space. Eigenvectors shown are for a skew network with $\overline{V} = 2$. 39
3.4 Top: Symmetry manifolds (dashed) and eigenvectors of LLL (arrows) in triangular reduced space. Middle: Separatrix manifolds found numerically for $\overline{V} = 2$. Bottom: Probability of winning found numerically as described in Section 3.2.2 (10,000 runs). . . 41

3.5 Separatrix manifolds computed numerically (solid) and approximated (dashed line), projected onto triangular reduced space. Top is $\overline{V} = 1.66$ and bottom is $\overline{V} = 2$. The initial condition (dot) has been shifted for clarity (actual value: $V_1(0) - V_3(0) = 0.002$). . 45
3.6 Probability of winning for three random conduit networks (no symmetry) for $N = 3, 4$ and 5. The probability of winning is proportional to the arclength along the dotted circle. 47
3.7 Interaction of symmetry manifold with the plane perpendicular to the most unstable manifold centered about the most unstable fixed point. 49

4.1 Exact pressure-volume response of a single spherical-cap drop (solid/blue). Approximate response of a full sphere works well at large volumes (red/dashed). In this figure only, pressure is scaled by σ/B and volume by $2\pi B^3/3$. 52
4.2 A single numerical simulation of a linear network with 100 drops, where the initial disturbance is randomly chosen from a hypersphere of radius $r_0 = 0.1$ centered about identical drop volumes of five hemispheres. Inset: n_ℓ/n against time. Volume is in hemispheres, time in scale T_{on}, defined in text. 54
4.3 Linear ($d = 1$), square ($d = 2$), complete ($d = n - 1$), and fractal (fractal dimension d_f) networks of conduits connecting drops. Complete network has been flattened from $d = 6$, therefore the conduits appear to have unequal lengths; periodic boundary conditions for this network means each line represents two conduits. 56
4.4 Sketch of adhesion device while coarsening. The height of the frit is H_F; reservoir depth H_R; distance between nearest drops L; and distance between nearest large drops W. For flow horizontal through the a porous media region, the pressure of the drop is applied at a radius A to account for the vertical flow entering from the orifice of radius B. 57
4.5 Network resistance for flow between two drops in square network: continuous (solid) vs discrete (squares) resistance. The continuous curve is fit to the discrete curve with a value of $\ln(a) = -1.7$. Inset: diamond-shaped domain through which flow travels for $w = 4$. 66
4.6 Coarsening of linear network according to equation (4.21). Simulations for $n = 100$, $r_0 = 0.1$, and $v_0 = 5$ (typical), unless otherwise noted in legend. Each simulation curve is an average of 100 simulations each with random initial condition. Simulations are cut off before they reached steady state for presentation purposes 69

4.7 Coarsening of complete network according to equation (4.22). Simulations for $n = 100$, $r_0 = 0.1$, and $v_0 = 5$ (typical), unless noted in legend. Each simulation curve is an average of 100 simulations each with random initial condition. Simulations are cut off before they reached steady state for presentation purposes. . 70
4.8 Coarsening of square network ($d = 2$) according to equation (4.23). Simulations for $n = 100$, $r_0 = 0.1$, and $v_0 = 5$ (typical), unless noted in legend. The predicted coarsening rate does not have a $-3/4$ exponent due to the non-zero value of a. 71
4.9 Coarsening of fractal network (various d_f). Simulations for $n = 128$, $v_0 = 5$, and $r_0 = 0.1$. Simulations are averaged over 100 random initial conditions. Predictions according to equation (4.25). 73
4.10 Probability distribution of large drop volumes. Simulations of complete, square and linear networks done with 2500 drops, Fractal network ($d_f = 2$) with 2048 drops. Only data between $500 > n_\ell > 200$ is used. All simulations had an initial volume of $v_0 = 5$ and a perturbation size of $r_0 = 0.1$. One standard deviation for the completely connected network is shown; error for other networks is of similar magnitude. 75
4.11 A complete network with $n = 1000$ and a random initial condition chosen such that it matches the self-similar distribution. . . 76

5.1 Macroscopic view (left) of a liquid bridge, pinned along a circle at the bottom, spreading along a substrate at the top. Microscopic view (right) of the moving contact-line region, illustrating the macroscopic and microscopic contact-angles (θ_d and θ_m) and speeds (U_d and U_m). 83
5.2 Bridge-drop force-length thermodynamic cycle for a constant half-volume $V = 2\pi R_0^3/3$. Solid lines are equilibrium states generated using branch-tracing code [27]. Arrows indicate non-equilibrium transitions at limits of stability. The shapes are for pinned-pinned contact-lines and spreading on a solid with 90° equilibrium contact-angle (indicated by dotted line). 87
5.3 Energy loss for pinned-pinned coalescence: Measured surface energy $\mathcal{A}$ (equation 5.19), measured work done by interface $\bar{\mathcal{P}} \equiv \int_0^t \mathcal{P} dt$ (equation 5.22) and accumulated viscous dissipation $-\bar{\mathcal{D}} \equiv -\int_0^t \mathcal{D} dt$ calculated by the BIM according to equation 5.24 (no fitting). Volume is $V/R_0^3 = 2.88$. The first $0.03s$ have been omitted. 92
5.4 Work done on the boundary of the control volume is equal to the rate of surface energy lost within it. 100

5.5 Measured contributions to surface energy, $\mathcal{A} = \mathcal{A}_{free} + \mathcal{A}_{solid}$ (equation 5.19), and to cumulative work done, $\bar{\mathcal{P}} = \bar{\mathcal{P}}_{free} + \bar{\mathcal{P}}_{solid}$ (equation 5.22). Spreading on a hydrophobic substrate, $\theta_e = 68.5 \pm 3.7^\circ$ and $V/R_0^3 = 1.24$ (left) and on a hydrophilic substrate, $\theta_e = 14 \pm 5^\circ$ and $V/R_0^3 = 1.70$ (right). No fitting. 103
5.6 Schematic of iteration for computation of microscopic shapes and slip-lengths. 108
5.7 Calculated contributions to energy dissipated $\bar{\mathcal{D}} = \bar{\mathcal{D}}_{free} + \bar{\mathcal{D}}_{solid}$ (equation 5.24) for the local slip (LS) and Navier slip (NS) boundary conditions. Loss of surface energy $\mathcal{A}$ (equation 5.19) is almost exactly equal to dissipation $\bar{\mathcal{D}}$ for both NS and LS. Slip-length is used as a fitting parameter. 110
5.8 Fraction of total viscous dissipation within radius R_v of contact-line for local slip (LS) and Navier slip (NS) models at subsequent times $t_1 = 0.096s$ (early), $t_2 = 0.304s$ (intermediate) and $t_3 = 1.008s$ (late). The wedge model predicts a linear relation. 111
5.9 Entire flow field for $t_1 = 0.096s$ (left), $t_2 = 0.304s$ (middle) and $t_3 = 1.008s$ (right) under constant $b = 135nm$ local slip condition. 113
5.10 Velocity fields and slip conditions at t_1 in a reference frame moving with the contact-line (solid velocity indicated by top arrow). The top row is for local slip (LS) where $b = 135nm$ is indicated by the square. The bottom row is for the Navier slip (NS) condition where $\beta = 35nm$ is indicated by the dashed line. Velocity vector lengths have been scaled to the plot range ($O(1\mu m)$ left column and $O(0.1\mu m)$ right column). 114
5.11 Along the solid-liquid and free interface in the moving frame (a), tangent velocity (b), normal traction (c) and tangential traction (d) at times $t_1 = 0.096s$, $t_2 = 0.304s$ and $t_3 = 1.008s$ for local slip (LS) and Navier slip (NS) boundary conditions. 115
5.12 Left: Measured dynamic angle (θ_d) and computed microscopic contact angle (θ_m) for Navier (NS) and local (LS) slip for constant slip-length parameters and for those adjusted frame-by-frame to satisfy the energy balance. Numerical accuracy of θ_m is $\pm 1^\circ$. Right: Necessary ordering of the angles for the case of an advancing contact-line. 119

5.13 Left: dynamic contact-angle θ_d against Ca, as measured and predicted by Voinov-Hocking-Cox (VHC) model, where $\theta_m = \theta_e$, $L_{in} = b$ and L_{out} is the viscous bending length. Right: L_{in} needed to make the VHC model match the experimental data exactly. Slip-lengths b for LS and β for NS conditions with the energy balance (equation 5.24) satisfied at each frame. The slip-length for the NS model is multiplied by ten for visual purposes. The length along the solid-liquid boundary at which the velocity is 10% of the contact-line velocity is shown for the NS boundary condition (NS 10%). 121

A.1 Pressure-volume response of a liquid bridge. Inset figures show disturbances which make the bridge go unstable. 134
A.2 Change in stability for constant pressure turning points 142
A.3 Change in stability for constant volume turning points 143

B.1 Complete and ring networks for $N = 4$. 144

CHAPTER 1

LIQUID DROP-BRIDGE SYSTEMS

1.1 Introduction

Two immiscible fluids meet along a free interface. Due to the greater affinity of fluid molecules to other molecules of the same kind (like attracts like), fluid molecules along the interface have a higher energy from intermolecular forces than those in the bulk [84]. This higher intermolecular energy means that energy is required to create more free interfacial area. The constant that relates the interfacial area to the surface energy is the surface tension γ. A decrease in area results in a decrease of energy, therefore the interface is in tension at all times.

The forces across a free interface must balance [26]. In the absence of surface tension gradients, the force balance tangent to the interface requires that the shear stresses of the two fluids are equal. Constant surface tension will be assumed throughout, therefore no surface-tension gradient induced flow will be considered (no Marangoni or thermo-capillary effects). The force balance normal to the interface requires that, in the absence of any flow, the pressure difference between the two fluids is balanced by the surface tension through the curvature of the surface according to the Young-Laplace equation

$$P_1 - P_2 = \gamma \left(\frac{1}{r_1} + \frac{1}{r_2} \right) \tag{1.1}$$

where P_1 and P_2 are the pressures of fluids 1 and 2 and r_1 and r_2 are the principle radii of curvature of the interface. The normal force balance in the presence of flow is

$$\boldsymbol{\sigma}_2 \cdot \boldsymbol{n} \cdot \boldsymbol{n} - \boldsymbol{\sigma}_1 \cdot \boldsymbol{n} \cdot \boldsymbol{n} = \gamma (\frac{1}{r_1} + \frac{1}{r_2}) \tag{1.2}$$

where $\boldsymbol{\sigma}$ is the total stress tensor, defined as $\boldsymbol{\sigma} = -P\boldsymbol{I} + \boldsymbol{\tau}$ where $\boldsymbol{I}$ is the identity matrix and $\boldsymbol{\tau}$ is the deviatoric stress tensor ($\boldsymbol{\tau} \equiv \mu(\nabla \boldsymbol{v} + (\nabla \boldsymbol{v})^T)$). Equation 1.1 is recovered when $|(\boldsymbol{\tau}_2 - \boldsymbol{\tau}_1) \cdot \boldsymbol{n} \cdot \boldsymbol{n}| \ll |P_1 - P_2|$.

In axi-symmetric coordinates, the sum of the principle radii of curvature can be related to the shape of the interface $R(z)$ according to the tangent-angle formulation [58]

$$\frac{dR}{dz} = \cot(\theta) \tag{1.3a}$$

$$\frac{d\theta}{dz} = \frac{-1}{\sin\theta}\left(\frac{1}{r_1} + \frac{1}{r_2}\right) - \frac{1}{R} \tag{1.3b}$$

where θ is the angle between the tangent of $R(z)$ and the horizontal line $z = constant$.

A few simple examples illustrate the Young-Laplace equation. For a sphere of radius r both principle radii of curvature are equal to the radius of the sphere. The inside of a stagnant sphere of liquid has a pressure that is higher than the outer fluid by a value $2\gamma/r$. For a flat interface both principle radii of curvature are infinite and the pressures of both fluids are equal. A cylinder has one principle radii of curvature equal to r and the other diverges, therefore the fluid inside a cylinder has a pressure that is γ/r greater than the outer fluid (in the absence of flow).

The interface may be subject to boundary conditions, for example, solid surfaces at which it is attached or along which it will move. Consider a free interface pinned at a circular contact-line. The minimum surface area is achieved with a planer free interface. If volume is pushed slowly through the circular contact line (so that normal shear stresses can be neglected and the inner and outer pressures are constant), then the Young-Laplace equation must be solved

along with a volume constraint. The solution is a spherical cap, or "drop". This solution can also be obtained by minimizing surface energy with the volume constraint through the calculus of variations [86]. Trigonometry relates the area, volume, and pressure [47].

If a free interface is pinned at two circular contact lines, which lie in parallel planes and whose centers both lie along a line perpendicular to the planes, an axi-symmetric liquid bridge is formed. The shape of the bridge, which has a specified volume, length and radius, can be found by solving the Young-Laplace equation or minimizing the surface area with a constrained volume and length. The shape of the bridge can be expressed in terms of incomplete elliptic integrals [37], although it is sometimes more practical to solve the system 1.3 numerically and use a look-up table to relate the volume, pressure, force, and length of bridge.

Consider any number of drops, where liquid can be exchanged between drops through a network of conduits. Volume is transferred due to pressure differences between drops until the surface area is minimized. This is will be referred to as a "drop system" or a network of drops. The tools developed in this thesis to study this network of drops can also be applied to a system of bridges coupled by a conduit network. A large amount of coupled bridges was not studied as the transcendental nature of the pressure-volume relationship of bridge makes it more cumbersome. Networks of bridges have an added difficulty because bridges break when the volume is too small and become axi-symmetric when the volume is too large.

Consider two drops, opposing each other along the same axis of symmetry. When the drops are enlarged they touch and form a liquid bridge. When

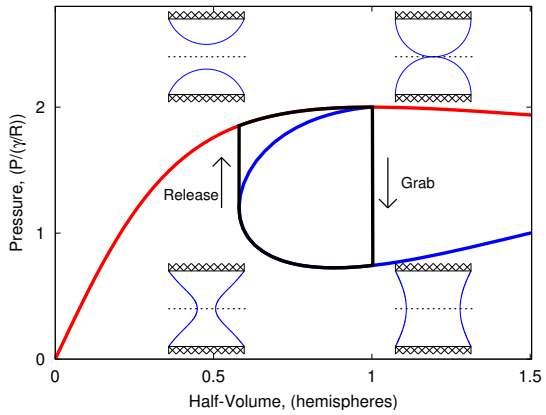

Figure 1.1: Thermodynamic bridge-drop cycle for a constant length equal to the pinning radius $L = R_0$.

volume is taken out of the bridge it, at some critical volume, becomes unstable and breaks, forming two drops. This "bridge-drop system" is illustrated in figure 1.1. The cycle can also be performed using only a single drop and a solid substrate. This is shown in figure 1.1 where the dotted line represents a solid which makes a fixed angle of 90° with the free interface.

1.1.1 Thermodynamic, mathematical and fluid-dynamics perspective

From a thermodynamic perspective, static liquid drops and bridges assume shapes that minimize the energy given the constrained volume and boundary conditions. In the absence of body forces, only the surface tension contributes to the energy. Often, the volume of the drops and bridges can be changed quasi-statically, such that they retain the shape that minimizes the energy. In this process the work done (such as adding volume against the pressure of a drop) is

stored in the surface energy (surface tension times the area). If the shape of the drop or bridge changes quickly then the quasi-static assumption breaks down, and energy is lost as heat.

The the static shapes are described mathematically as the minimum of the energy, found using the Euler-Lagrange equations. For a constant volume and a single contact line about a circular orifice or nozzle, a spherical cap is formed. For a constant volume constrained by two circular contact lines, a liquid bridge forms between the circles ([37]). The stability of the shapes can be found from the second variation. The change in stability can alternatively be found by identifying the turning points in a plot showing the equilibrium curve [14, 66]. When a liquid bridge becomes too large the stability changes, and it breaks to form two drops. When two drops are brought close together (or a drop is brought close to a solid substrate) a liquid bridge forms. Methods used to find the static shapes and their stabilities are reviewed in appendix A.

Static drop-bridge shapes can be thought of in terms of fluid dynamics as systems with small capillary number so that the presssure within the drop/bridge is constant. The shape is determined by the Young-Laplace equation, given a constrained liquid volume and contact line boundary conditions. When two drops touch they form a liquid bridge. In the 'neck' region where the bridge forms the curvature of the interface has a very negative curvature, the pressure is extremely low due to the Young-Laplace equation. The low pressure drives fluid into the 'neck' region of the bridge until the pressure of the bridge is constant, and a static shape is reached.

Consider a coupled drop network. The pressure of a drop depends on its volume, and volume is exchanged between drops according to the pressure drop

across a conduit. Drops lose surface energy due to the decrease of total surface area and this energy is dissipated by viscosity in the conduits. The total energy of the drops decreases monotonically with time until all the pressures are equal and only one of the drops is large (super-hemispherical) with all others being small (sub-hemispherical). The stability and dynamics of such systems of drops is explored in this thesis.

When a bridge spontaneously changes shape to become two drops, no intermediate equilibrium shapes exist. This process is irreversible; the decrease in surface energy is lost through the viscous dissipation within the fluid. The intermediate shape can be determined by solving the hydrodynamic equations of the liquid given an initial condition. The shape must still satisfy the balance of surface energy and viscous dissipation at all times. For two pinned drops which form a liquid bridge this energy balance is trivially satisfied. For a drop which touches a substrate and then spreads, this constraint provides insight into the microscopic behavior of the moving contact line.

1.2 Motivation

1.2.1 Engineering applications

This study is motivated by a reversible capillary adhesion device [97]. A schematic of the device is shown in figure 1.2. The device consists of a water reservoir above which is a porous membrane (or frit) which connects to a plate with a large number of holes (or orifices). The liquid is pumped through the orifices by electro-osmosis to form liquid drops. Ideally, all drops will make contact

with a solid substrate to form liquid bridges. These bridges exert a pulling force, and this causes the device to stick to the substrate. The adhesion can be turned off by reversing the voltage on the electroosmotic pump until the volume of the bridges has decreased so that they become unstable.

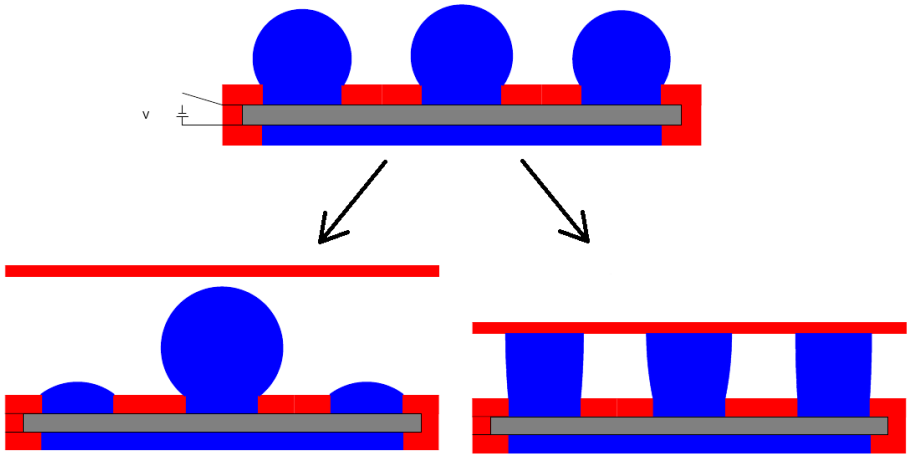

Figure 1.2: Schematic of capillary adhesion device. Initial condition of drops (Top). Device may coarsen (bottom left) or adhere to substrate (bottom right).

The drops can interact with one another through the reservoir, the membrane or between the membrane and the top plate due to possible manufacturing defects. If the device is not attached to the substrate quickly enough, it has been observed that the drops will exchange volume until only one drop large drop remains (cf. figure 1.2). In chapter 2 it is shown that there is no way to avoid this state for spherical-cap drops. The identity of the end-state large drop is studied in chapter 3. It is also of interest how long it would take for a certain fraction (say half or a quarter) of the drops to make contact; this is answered in chapter 4.

The coarsening of the drops may not always be detrimental to the applica-

tion. An application that uses the surface tension of the drops to drive flow through a microfluidic device is benefited by coarsening [103, 70]. Exchange of volume between bridges may increase the strength of the adhesion device. Consider a system of bridges in the domain of attraction of a stable fixed point of all bridges. The surface energy decreases throughout the dynamics, therefore the final state is at a lower potential energy than the initial state. More work will be required to remove the device from the substrate due to this lower potential energy, often this is due to an increase in the force.

The coarsening of drops follows the same dynamics as many other coarsening processes, such as those in spinodal decomposition [12, 88], dewetting of thin films [39, 91], granular mechanics [94, 69, 106], image enhancement [79] and population dynamics [78].

Another aspect of the adhesion device is the transition from drop to bridge. For multiple grab-release cycles it is desired to know how long this process takes and the energy required for such a cycle. These questions are addressed in chapter 5. Here the details of the moving contact-line must be understood, and insights into this problem has a variety of applications such as enhancing heat transfer [21] coating flows [105], microfluids and inkjet printing [8].

1.2.2 Scientific and mathematical motivation

The tools developed to find the stability and dynamics of drop systems can be transferred to systems with different kinds of pressure-volume responses, such as rubber balloons [73], drops with surfactants and liquid bridges [37].

Some of the results are even more general than this, for example, it is shown that the dynamic stability (the number of characteristic stable and unstable directions in phase space) and energy stability (the number of stable and unstable directions of the energy landscape) are equivalent. As a result the dynamic stability of any fixed point can be found from the Hessian of the Lyapunov function. This is of interest to the thermodynamicist - the stability of a system is known if the entropy (a Lyapunov function) is known. If two systems have the same Lyapunov function, the stabilities are the same even if the dynamics are different.

Determining which drop takes all the volume involves the interaction of a dynamical system with the symmetry of the network. Many previous studies have used symmetry to find the equilibrium states [40] of a system. In this study symmetry is used to find the domains of attraction and thus predict the long-term dynamics of a system from the initial condition.

Determining time to coarsen requires finding a pre-exponential factor of the coarsening rate. This prefactor can be determined by finding a self-similar distribution of drop volumes [63, 102] (LSW model), however verification with experiments has been difficult [83]. Orthogonal networks and fractal networks with varying dimension are studied and these are found to have different pre-exponential factors, although the LSW model predicts pre-exponential factors independent of the network dimension.

The behavior of the contact-line has a rich history of scientific contributions (see [52] or [4]) yet many new effects are still being discovered ([8]). In chapter 5 the fluid dynamics of the full domain of a spontaneously spreading bridge are resolved using simulations, and an energy balance is used to obtain information

about the microscopic behavior of the contact-line region. The energy balance is also used to determine the different contributions to the energy of the spreading bridge. It is shown that the viscous bending of the contact region also dissipates energy, a term which has been omitted from many previous studies ([24]).

CHAPTER 2

STABILITY OF COUPLED DROPS*

2.1 Introduction

Consider a system consisting of a plate with N identical holes, where liquid is pushed up through each hole to form a spherical drop with a pinned contact line. That is, a drop of area A_j and volume V_j protrudes from an orifice j where $j = 1 \dots N$. Here, area is scaled by $\frac{2}{3}\pi\tilde{B}^2$ and volume by $\frac{2}{3}\pi\tilde{B}^3$, where $\tilde{B}$ is the dimensional hole radius. A network of conduits under the plate allows volume to be exchanged amongst the drops. The flow through the pipes is assumed to be laminar, although this is not necessary. The capillarity of the drops causes a pressure difference between drops whose curvatures are imbalanced. Inertia of the drops and the effect of gravity are neglected. The coupled drops compete for volume based on a minimization of total exposed drop surface area,

$$A_T \equiv \sum_{i=1}^{N} A_i, \tag{2.1}$$

subject to the constraint of fixed average-volume,

$$\overline{V} \equiv V_T/N \equiv \sum_{i=1}^{N} V_i/N. \tag{2.2}$$

Note that surface area is proportional to surface energy (with surface tension as constant of proportionality), so we may speak of energy and area minimizations interchangeably.

Snapshots of an experiment with a 6×4 array of drops (figure 2.1) illustrate the stability and dynamics. A Delrin® plate with holes is clamped on top

*H.B. van Lengerich, M.J. Vogel and P.H. Steen, Dynamics and Stability of Volume-Scavenging Drop Arrays: Coarsening by Capillarity *Physica D* **238** (2009) pp531-539 Reprinted with permission

of a porous frit (modeled as a network of conduits) which sits above a water reservoir. A syringe is used to quickly push liquid from below through the frit and holes so that the drops initially have nearly identical super-hemispherical volumes, as seen in figure 2.1 i. The system is then left to equilibrate. Initially, the drops scavenge volume from their nearest neighbors. Later, the drops that are large, and therefore have volume to lose, are separated by many different lengths and hence are differently coupled, figure 2.1 ii. The remaining few drops exchange volume until there are only two left (figure 2.1 iii) and finally the dynamics stop when there is only one large drop remaining (figure 2.1 iv).

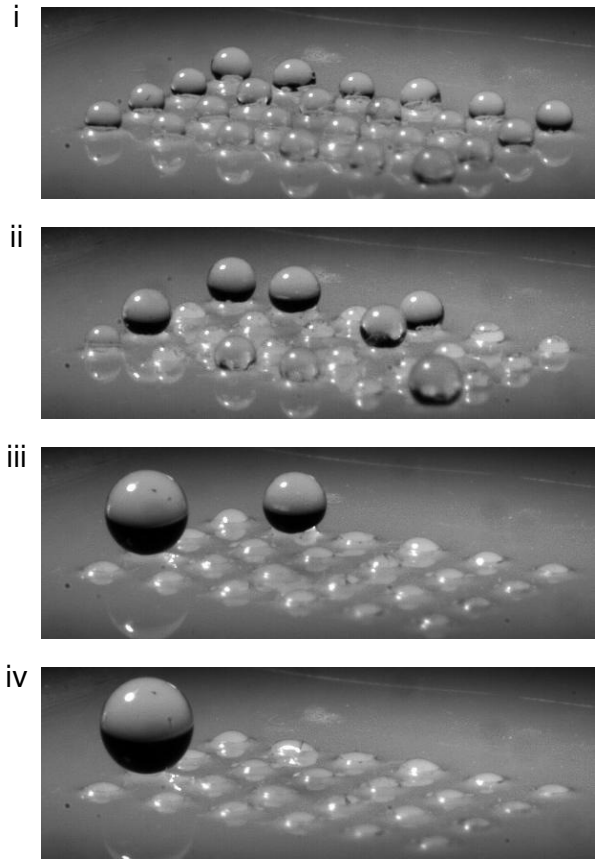

Figure 2.1: Dynamics of a 4 x 6 array of drops protruding from 500 μm holes sitting above a frit with 4-5.5 μm pore diameter. Elapsed time i = 0s, ii = 2.0 s, iii = 21.3 s iv = 31.9 s.

Volume-scavenging is an example of a coarsening or ripening phenomena. These phenomena are of interest to a broad range of physico-chemical problems such as solidification of alloys [13] [83], dynamics of emulsions [88], evolution of hydrophobic thin films [39], and image enhancement [36]. Our interest in volume-scavenging arises from a specific microfluidic application inspired by the extraordinary adhesion exhibited by the palm beetle [33]. If a flat plate were placed on top of the drops in figure 2.1 i, then 24 liquid bridges could be formed, each acting as a bond. The adhesion could be turned on or off by manipulating the volume of the drops with an electro-osmotic pump [96]. Volume-scavenging can be detrimental or advantageous for the adhesion of arrays of drops to various types of substrates, depending on circumstances. Systems of coupled drops are also important to other applications, such as lab-on-a-chip devices [70].

The binary nature of the static drop shapes is due to the nonlinear pressure-volume constitutive relation for spherical-cap drops (figure 2.2). Here, pressure P (scaled by $\tilde{\sigma}/\tilde{B}$ where $\tilde{\sigma}$ is surface tension) is related to the volume through the drop curvature and the Young-Laplace law. Trigonometry gives the pressure, volume and surface area in terms of the height of the drop, $h = \tilde{H}/\tilde{B}$,

$$P = 4/(h + 1/h) \tag{2.3a}$$

$$V = h(h^2 + 3)/4 \tag{2.3b}$$

$$A = 3(h^2 + 1/4)/2. \tag{2.3c}$$

For a given pressure, one drop can have either a sub-hemispherical S (small) or super-hemispherical L (large) volume. For N drops, the condition for system static equilibrium is that all drops share a common pressure (see Section 2.3). Thus, in the absence of any volume constraint, there will typically be 2^N families of equilibria parametrized by total volume(branches), corresponding to the

static shapes given by any choice of S and L for each position.

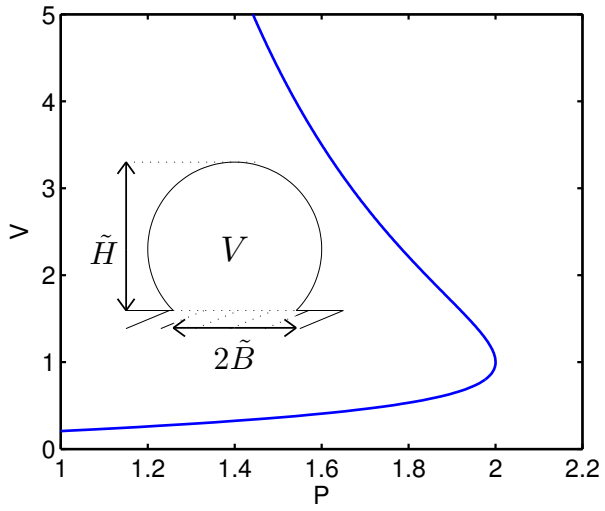

Figure 2.2: Dimensionless drop volume V against pressure P (in units of $\tilde{\sigma}/\tilde{B}$. The curve is parametrized by the height of the drop $h = \tilde{H}/\tilde{B}$.

Consider, for example, a system of two coupled drops. The network here is trivial, see figure 2.3 (top). The two-dimensional phase space has only one branch (SS) when $\overline{V} < 1$. At $\overline{V} = 1$, a supercritical pitchfork bifurcation occurs and for $\overline{V} > 1$ three equilibrium branches (SL, LL, and LS) exist. For arbitrary $\overline{V} > 1$, at any state near the LL fixed point, one drop will have slightly larger volume than the other. The larger drop has a smaller pressure, so this drop will take volume from the smaller one until it wins (the SL or LS equilibrium is reached). The dynamics for the constrained problem are indicated in the 'phase-line' plot, figure 2.3 (middle). The corresponding shapes are sketched in figure 2.3 (bottom).

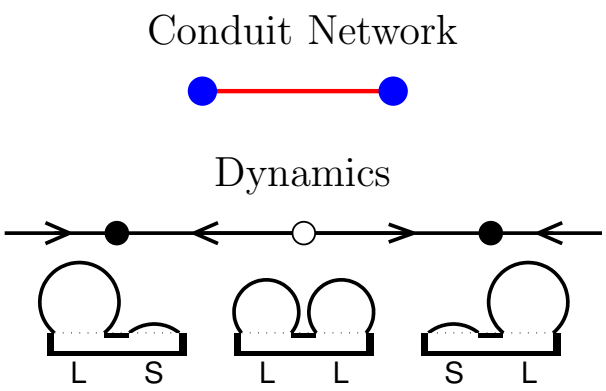

Figure 2.3: Top: Two drops coupled by a single conduit. Middle: The phase space is 1-dimensional with state variable $(V_2 - V_1)$. The closed circles are stable fixed points and the open circle is unstable. Bottom: Each fixed point corresponds to the arrangement of drops shown schematically.

2.2 The family of dynamical systems

2.2.1 Connectivity networks

The connectivity network can be defined by an $N \times N$ connectivity matrix c_{ij}, similar to an adjacency matrix for networks [46]. An element of c_{ij} gives the conductance of the conduit between drops i and j (see figure 2.4 top left). Three assumptions restrict the c_{ij} matrix,

$$c_{ii} = 0 \tag{2.4a}$$

$$c_{ij} = c_{ji} \tag{2.4b}$$

$$c_{ij} \geq 0. \tag{2.4c}$$

These assumptions ensure that (2.4a) the drops do not connect to themselves, (2.4b) the resistance between drops is the same regardless of flow direction, and (2.4c) all conductances have the same sign. When two drops i and j are not

directly connected then the conductance is zero ($c_{ij} = 0$). When conductances are equal between all directly connected drops, we can set $c_{ij} = 1$ for these, absorbing the details of the conductance into the dimensionless time. This is done for four of the five networks considered (figure 2.4): 'complete'; 'ring'; 'linear'; and 'star' (adopting the graph theory terminology [46]). For the 'skew' network, a slight generalization is needed as different conduits have different conductances.

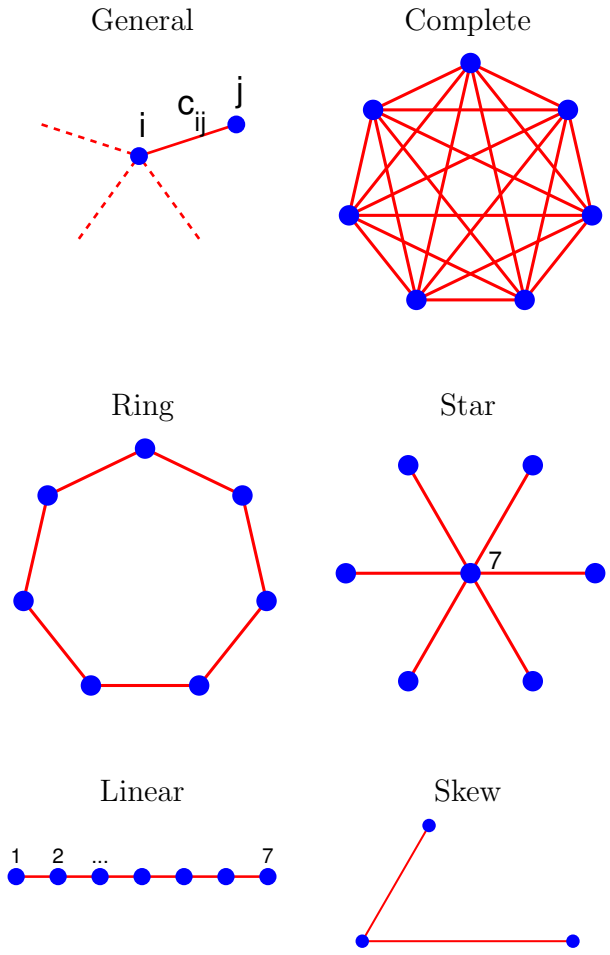

Figure 2.4: Various connectivity networks. Numbering convention indicated when necessary. Diagrams can be generalized to arbitrary N.

The complete network has equal conductivity between all drops. This net-

work has symmetry of the symmetric group, S_N (cf. [40]). All permutations of the drop indices leave the system unchanged. Here, the c_{ij} matrix is all ones except for zeros on the diagonal. The ring network has the drops connected in a circle with equal conductivity between neighbors. The ring has symmetry of the dihedral group (D_N), and there are ways to switch indices so that any drop can have any index that leaves the system unchanged. The ring network is made into a linear network by setting one of the conductances to zero. Switching from ring to linear is analogous to changing a periodic boundary condition into two no-penetration boundary conditions. Symmetry is lost; the only remaining symmetry is the line that goes through the center drop(s). The skew configuration, where no two conductivities are equal, is distinguished as the simplest network without any symmetry. Here, non-unity entries in the c_{ij} matrix are allowed, as mentioned above. The star network plays a central role in the stability analysis because it is the only network that yields a gradient system in the reduced phase space of the dynamical system (see Section 2.3).

For some of the networks shown above, the probability of winning can be predicted without detailed analysis. Since all indices are interchangeable for the complete and ring networks, one expects $p^N = (1/N, 1/N, \ldots, 1/N)$. This has been confirmed using numerical simulations similar to those described in Section 3.2.2. For the star with the center drop labeled N, all but the center drop have interchangeable indices, and one expects $p^N = (b_1, b_1, \ldots, b_1, b_2)$. Indeed, numerical simulations confirm this result, giving $b_1 = 1/(2N-2)$ and $b_2 = 1/2$.

2.2.2 Governing dynamical system

System (3.1) is now generalized with regard to connectivity network and flow law. Consider a set of N drops. For an incompressible liquid, conservation of mass at node j in a network requires the volume of drop j to change as,

$$\dot{V}_j = \sum_{i=1}^{N} q_{ij}, \quad \text{for } j = 1 \dots N, \tag{2.5}$$

where q_{ij} is the volumetric flow rate from node i into node j. Here, the dot indicates differentiation with respect to dimensionless time. Flow is driven by pressure differences between drops i and j,

$$\Delta P_{ij} \equiv P(V_i) - P(V_j), \tag{2.6}$$

according to, (no summation)

$$q_{ij} = c_{ij} f(\Delta P_{ij}), \tag{2.7}$$

where c_{ij} is the connectivity matrix of the network (Section 2.2.1), and $f(s)$ is the flow law. The Young-Laplace response for spherical-cap drops, $P(V)$, is plotted in figure 2.2 and is displayed in closed-form in Appendix C. Here, surface tension $\tilde{\sigma}$ is presumed constant.

Restrictions on the c_{ij} matrix were set forth in Section 2.2.1. In conjunction with these, the function $f(s)$ must also satisfy a few restrictions. It turns out that the following three restrictions are sufficient to give the stability results found in Section 2.3,

$$f(-s) = -f(s), \tag{2.8a}$$

$$f(s) > 0 \text{ for } s > 0, \text{ and} \tag{2.8b}$$

$$\left.\frac{df(s)}{ds}\right|_{s=0} \neq 0. \tag{2.8c}$$

Changing the sign of the pressure drop changes the direction of the flow, equation (2.8a), flow is along the pressure gradient, equation (2.8b), and the slope of the flow law does not vanish at equilibrium states, equation (2.8c). These assumptions are quite general. Hagen-Poiseuille flow $f(s) = s$ meets the above criteria. In this case the time scale is chosen to be $\tilde{\tau} = 16/3(\tilde{\eta}\tilde{B}/\tilde{\sigma})$ where $\tilde{D}$ is the conduit diameter, and $\tilde{\eta}$, the liquid viscosity. With this choice, conductances c_{ij} are proportional to $\tilde{D}^4/(\tilde{L}\tilde{B}^3)$ where $\tilde{L}$ is the conduit length. Many other flow laws including friction-factor Reynolds-number relationships and non-Newtonian laws also satisfy Eqs. (2.8a), (2.8b), and (2.8c).

Two forms of equivalent governing systems are shown below. Their difference lies in how the volume constraint (equation (2.2)) is handled; it can be left in, or eliminated by direct substitution. Each form is useful for different types of calculations.

Full system: N dimensional

Substituting equation (2.7) into equation (2.5) gives,

$$\dot{V}_j = \sum_{i=1}^{N} c_{ij} f(\Delta P_{ij}) \tag{2.9a}$$

with initial conditions,

$$V_j(0) = \overline{V} + \epsilon_j. \tag{2.9b}$$

This N variable system will be referred to as the 'full' system. This system depends on $N(N-1)/2$ parameters from c_{ij}. Inserting Eqs. (2.9a) into equation (2.2) and taking account of equation (2.8a) and (2.4b) shows that total volume is independent of time. The volume constraint restricts the dynamics to an $N-1$ dimensional hyper-plane orthogonal to the N-vector $[1, 1, \ldots, 1]$.

Reduced system: $N-1$ dimensional

An alternative form is obtained by eliminating one of the variables directly. Choosing to eliminate V_N yields

$$\dot{V_j} = \hat{c}_{Nj} f(P(V_T - \sum_{i=1}^{N-1} V_i) - P(V_j)) + \sum_{i=1}^{N-1} \hat{c}_{ij} f(\Delta P_{ij}) \tag{2.10a}$$

with initial conditions,

$$V_j(0) = \overline{V} + \epsilon_j. \tag{2.10b}$$

for $j = 1...N-1$. This will be referred to as the 'reduced' system. The reduced connectivity matrix is defined by $\hat{c}_{ij} = c_{ij}$ for all $i = 1...N$ and $j = 1...N-1$. Hence, $\hat{c}_{ij}$ is an $N \times (N-1)$ matrix. Note that c_{ij} can be reconstructed from $\hat{c}_{ij}$ using the relations $c_{ij} = \hat{c}_{ij}$ for all $i = 1...N$ and $j = 1...N-1$, $c_{NN} = 0$, and $c_{iN} = \hat{c}_N i$ for $i = 1...N-1$. In summary, there exists a *one-to-one relationship between* $\hat{c}_{ij}$ *and* c_{ij} which yields an invertible mapping between the full and reduced systems.

2.3 Global phase flow, fixed points and their stability

Proposition 1. *Total area A_T is a Lyapunov function.*

Starting with the Gauss relationship between dimensional surface area and volume $d\tilde{A} = 2\tilde{\kappa} d\tilde{V}$ where $\tilde{\kappa}$ is the dimensional mean curvature of a surface, one can eliminate the mean curvature using the Young-Laplace equation. Then, scaling area, volume, and pressures as done previously, one can write $A_i = \int_0^{V_i} P(V) dV$ for each drop $i = 1, \ldots N$. Summing gives an alternate expression

to equation (2.1),

$$A_T = \sum_{i=1}^{N} \int_0^{V_i} P(V) dV. \tag{2.11}$$

Taking the time derivative, substituting from equation (2.9a), and using equation (2.4b) and (2.8a) yields

$$\dot{A_T} = \sum_{j=1}^{N} \sum_{i=j+1}^{N} -c_{ij}(\Delta P_{ij}) f(\Delta P_{ij}). \tag{2.12}$$

In view of equation (2.4c) and (2.8b),

$$\dot{A_T} \leq 0; \quad \dot{A_T} = 0 \text{ if and only if } \Delta P_{ij} = 0 \text{ for all pairs } i, j. \tag{2.13}$$

That is, area is strictly decreasing along trajectories and is stationary only at fixed points. Thus, A_T is a Lyapunov function. Note that although A_T is a function on all phase space, the substitution of (equation (2.9a)) also results in A_T being Lyapunov on the constrained space. Thus the Lyapunov property holds for both full and reduced systems. A_T is bounded from below by the area of one large and $N-1$ small drops.

Because the Lyapunov function is constant only at fixed points, there can be no recurrent dynamical behavior. That is, neither periodic solutions nor chaos is possible. In the absence of recurrent orbits, one may anticipate that the fixed points of system (2.9) will provide a framework for the heteroclinic connections, which in turn will provide a framework for the separatrix boundaries of the domains of attraction. That a common pressure characterizes the equilibrium states may be anticipated by the variational structure of this classical mechanics problem. The first variation of A_T leads to a force balance whose static solutions require all forces in the system to be equilibrated.

Proposition 2. *For $\overline{V} > 1$, there are exactly $2^N - 1$ fixed points of system(2.9) and, for each fixed point, all drop pressures are equal.*

When $P(V_i) - P(V_j) = 0$ for all pairs i, j (an equilibrium state), it follows that $\dot{V_j} = 0$ by equation (2.9a), while from equation (2.13) it follows that this condition is also necessary. For a fixed pressure, it can be seen from figure 2.2 that all small drops must have the same volume $V_S < 1$ as well as all large drops $V_L > 1$. Here there are 2^N possible arrangements of S and L drops. It is left to show that for a fixed $\overline{V} > 1$ there is exactly one solution satisfying $P(V_i) - P(V_j) = 0$ for all pairs i, j, for each arrangement, except for the case of all small drops. All small drops ($n_S = N$) cannot occur since then $V_S = \overline{V}$, contradicting $\overline{V} > 1$. For each value of n_S, $0 \leq n_S \leq N - 1$, the volumes must satisfy $P(V_S) = P(V_L)$ along with the constraint $(n_S/N)V_S + (n_L/N)V_L = V_T/N = \overline{V}$ for any $\overline{V} > 1$. Using the parametric form of $(P(h), V(h))$ one can show that these equations have exactly one solution. The proposition follows. Find details in Appendix C. Because systems (2.9) and (2.10) are equivalent, the proposition also holds for system (2.10).

For any number of small n_S and large n_L drops, each of the $2^N - 1$ fixed points falls on one of N levels of total area depending on n_L. The area of a n_L fixed point is labeled A_{n_L}, as illustrated for $N = 4$ in figure 2.5. The number of fixed points on the same area level A_{n_L} is given by the binomial coefficient $N!/(n_S!n_L!)$.

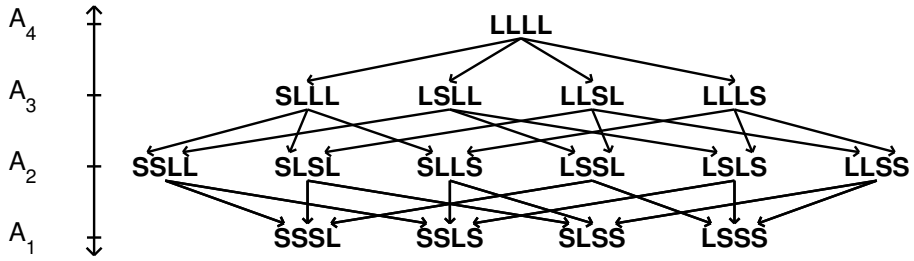

Figure 2.5: The fixed points for $N = 4$ arranged in a hierarchy of energy levels with heteroclinic connections indicated (arrows).

Proposition 3. *For the star network with drop N at the center ($\hat{c}_{Nj} = 1$ for $j = 1 \ldots N-1$ and $\hat{c}_{ij} = 0$ for $i, j = 1 \ldots N-1$) and with Hagen-Poiseuille flow $f(s) = s$, the reduced system (2.10) is a gradient system.*

We need to show that (cf. [43]),

$$\dot{V}_j = -\frac{\partial E}{\partial V_j}, \tag{2.14}$$

where E is the reduced energy, defined by,

$$E \equiv \int_0^{V_T - \sum_{i=1}^{N-1} V_i} P(V)dV + \sum_{i=1}^{N-1} \int_0^{V_i} P(V)dV. \tag{2.15}$$

Note that the value of the reduced energy is equivalent to that of the area $E = A_T(V_1, V_2, ..., V_{N-1}, V_T - \sum_{i=1}^{N-1} V_i)$. The proposition follows by direct calculation using the given $\hat{c}_{ij}$.

The key property of a gradient system, which we shall use below, is that stability according to the local energy landscape is the same as dynamical linear stability. To that end, the $(N-1) \times (N-1)$ Hessian matrix of the energy is defined in the standard way,

$$H_{jk} \equiv \frac{\partial^2 E}{\partial V_j \partial V_k}. \tag{2.16}$$

Proposition 4. *For the system of Proposition 3 with $\overline{V} > 1$ and $V_N > 1$, the eigenvalues and eigenvectors of $-H_{jk}$ can be calculated explicitly for all possible fixed points. A fixed point of the reduced dynamical system (2.10), with (n_S, n_L) drops, has n_S stable directions and $n_L - 1$ unstable directions.*

Because the Hessian is symmetric, the eigenvalues are real and there is a full set of linearly independent eigenvectors. All $N-1$ eigenvectors are found by inspection, from which the eigenvalues are calculated. The eigenvalues and

eigenvectors are listed in Table D.1 and a description of how they were obtained is provided in Appendix D. A theorem by Gillette and Dyson [38] could have been used in this situation to determine the stability of the Hessian. However, the theorem determines only if there is at least one unstable eigenvalue. We desire the full set of eigenvalues to completely characterize the linear dynamics.

Proposition 5. *At the fixed points, the Jacobian matrix of the reduced system (2.10), can be written as*

$$J_{ik} = \left.\frac{df}{ds}\right|_0 U_{ij}(-H_{jk}) \tag{2.17}$$

where U_{ij} is a symmetric $(N-1)\times(N-1)$ matrix of conductances:

$$U_{ij} = \begin{cases} \sum_{k=1}^{N} c_{kj} & \text{for } i = j \\ -c_{ij} & \text{for } i \neq j \end{cases} \tag{2.18}$$

for $i, j = 1...N-1$.

This proposition follows by straightforward algebraic manipulation and sets us up to use special properties of the U_{ij} matrix, which we call the 'unisignant matrix'. Note that only the first $(N-1)\times(N-1)$ entries of the c_{ij} matrix are used in defining the off-diagonal entries of U_{ij}.

Proposition 6. $det(U_{ij}) > 0$ *for all connected networks.*

The unisignant matrix (equation (2.18)) was known by Sylvester to belong to the class of matrices with nonzero determinants [72]. The convention set in equation (2.4c) yields the positive sign. The invariance of the sign of the determinant was coined the 'unisignant' property by Sylvester. The proof of the proposition with the interpretation of Sylvester's work to networks is given in [17]. When the c_{ij} network is a graph, the proposition is a corollary of the

Matrix-Tree Theorem [54]. An example of this important property is illustrated in Appendix B. This leads to the main result of this Section.

Proposition 7. *For $f(s) \propto s$, the reduced system (2.10) takes the form*

$$\dot{V}_j = -U_{ij}\frac{\partial E}{\partial V_i}. \tag{2.19}$$

The statement can be verified by algebraic manipulation, and it is seen that the statement holds only for linear flow functions $f(s)$. By differentiating this result, Proposition 5 for systems with Hagen-Poiseuille flow follows. Because the unisignant matrix is nonsingular, the drop pressures balance at fixed points, therefore Proposition 2 can be obtained without the use of the necessary condition obtained from Proposition 1. The system $\dot{V}_j = -U_{ij}\frac{\partial E}{\partial V_i}$ becomes a gradient systems when U_{ij} is identity. Many of the properties of gradient systems also hold for this 'unisignant system' (energy and dynamics stability are the same, E is a Lyapunov function, and there are no periodic orbits).

Proposition 8. *For $\overline{V} > 1$, any network, and any flow law satisfying equation (2.8c), a fixed point of system (2.10) with (n_S, n_L) drops has n_S stable directions and $n_L - 1$ unstable directions.*

Taking the determinant of (2.17) one finds

$$det(J_{ik}) = \left(\left.\frac{df}{ds}\right|_0\right)^{N-1} det(U_{ij})det(-H_{jk}). \tag{2.20}$$

The proposition is based on the idea that the Hessian is independent of connectivity matrix c_{ij}. Since the eigenvalues of the star gradient system with $V_N > 1$ are known (Proposition 4) and since one can deform starting from the star network with a unisignant property (Proposition 6), one can monitor the sign of the determinant of the Jacobian along a deformation path from the star network

to another network. In particular, for any flow law satisfying (equation (2.8c)), the derivative of f is nonzero for fixed points. Suppose the c_{ij} matrix is varied in a manner so that the network is always connected, then $det(U_{ij})$ is never zero (Proposition 6). Starting at the star where $det(H_{jk}) \neq 0$, one concludes that $det(J_{ik})$ of never passes through zero and the signs of the eigenvalues remain invariant through the deformation. The proposition follows.

When transforming from one network to another, we can first add all the new connections, then take away the ones we do not need, so that the network is connected throughout the deformation. Consider transforming the unisignant matrix in this manner, from the identity to any other network. Or consider varying the flow function from $f(s) = s$ to any other function that meets the assumption (equation (2.8c)). Then the Jacobian remains nonsingular throughout the deformation, and therefore the eigenvalues of J_{ij} are the same sign as those of the Hessian. The next section presents an example of deformation.

We have found that the stability of the dynamical system is the same as the energy stability for all networks and flow types. The reason for this is the structure of the Jacobian. The nonzero determinant of the unisignant causes the signs of the eigenvalues of the Jacobian to be the same as those of the Hessian - even for systems that are not gradient systems.

2.3.1 Deformation example

Consider obtaining the signs of the eigenvalues of a fixed point from the star network with a small center drop. Begin at a fixed point of a star with a large drop at the center and at least one small drop on the outside. A deformation of the

star network that switches the large center drop for a small center drop is constructed. The needed conduits of the final configuration are added first, then the unneeded conduits are removed, as shown in figure 2.6. Because the network remains connected, the unisignant matrix remains nonsingular throughout the deformation. Since the Hessian is nonsingular, the Jacobian matrix must remain nonsingular throughout the transformation. Therefore, signs of the eigenvalues of the deformation end configuration must correspond to those of the beginning configuration. This kind of argument can be extended to apply to deformation paths from the star network to any other network.

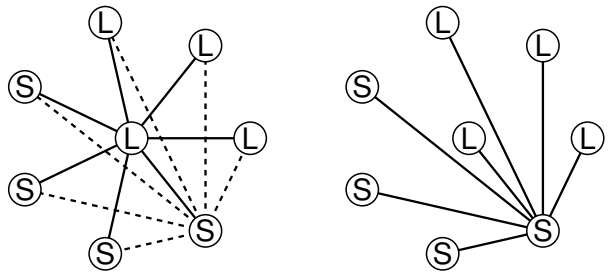

Figure 2.6: A deformation from center drop large to center drop small. Left: The original star network with center drop large (solid lines). The dotted lines are the new connections made. Right: The solid lines that are not used are taken away. The network is now star with a small center drop. The network remains connected throughout the deformation.

2.4 Generalized gradient systems

If a strong Lyapunov function exists for a dynamical system, then for any non-degenerate fixed point with nonsingular Jacobian and Hessian matrices, the number of stable and unstable eigenvalues is the same for the Jacobian matrix and the Hessian. This result is often important for the scientist, as entropy is

always a (negative) Lyapunov function, and thus the stability can be found for a variety of systems (which have the same entropy) with only one calculation of eigenvalues. The result can also be used to find the number of stable and unstable eigenvalues of the Hessian. By analyzing a related dynamical system a Jacobian matrix from which the eigenvalues are easy to pick off may be found. A caveat of this proof is that it requires that the determinant of the Jacobian and the Hessian to be found. This is not necessary if the transformation matrix from dynamical system to gradient system is known.

2.4.1 Proof

Consider the dynamical system

$$\dot{x} = f(x) \tag{2.21}$$

where $x \in \mathbb{R}^N$ and f is a C^r function where $r > 2$. Assume we can find a strong Lyapunov function

$$\dot{V} \leq 0; \;\; \dot{V} = 0 \text{ if and only if } f(x) = 0. \tag{2.22}$$

where V is a C^{r+1} function. Consider the space close to a fixed point x^*. We assume that the fixed point is non-degenerate, has nonsingular Jacobian and Hessian matrices, and that the angle between f and ∇V is locally bounded away from $\pi/2$.

Proposition 9. *For the system described above there exists a C^{r-1} matrix function L which is positive definite in a neighborhood of x^*, and for which $f = L\nabla V$ (or $f_i = L_{ij}\frac{\partial V}{\partial x_j}$).*

The proof is given as Proposition 2.11 in McLachlan [68]. Since L is at least C^1 it is continuous, L is bounded, and it has a continuous first derivative, so $\frac{\partial L}{\partial x_i}$ is bounded.

Proposition 10. *At a fixed point the Jacobian matrix is given by*

$$J_{ik}(x^*) = \left.\frac{\partial f_i}{\partial x_k}\right|_{x^*} = -L_{ij}(x^*) \left.\frac{\partial^2 V}{\partial x_j \partial x_k}\right|_{x^*} \tag{2.23}$$

This is a simple one step calculation; by the chain rule

$$\begin{aligned} \left.\frac{\partial f_i}{\partial x_k}\right|_{x^*} &= -\left.\left[\frac{\partial L_{ij}}{\partial x_k}\frac{\partial V}{\partial x_j}\right]\right|_{x^*} - L_{ij}\ (x^*)\left.\frac{\partial^2 V}{\partial x_j \partial x_k}\right|_{x^*} &(2.24)\\ &= -L_{ij}(x^*) \left.\frac{\partial^2 V}{\partial x_j \partial x_k}\right|_{x^*} &(2.25)\end{aligned}$$

Here we have used the important fact that $\frac{\partial L_{ij}}{\partial x_k}$ is bounded at the fixed point. We can write this proposition as

$$J(x^*) = L(x^*)H(x^*) \tag{2.26}$$

where H is the Hessian matrix and the index notation has been dropped.

Proposition 11. *A deformation path from the identity (I) to any positive definite matrix (L) exists so that the determinant along the path is always positive.*

Consider the matrix

$$M(\alpha) = I + \alpha(L(x^*) - I) \tag{2.27}$$

where $0 \leq \alpha \leq 1$. For a vector v

$$\begin{aligned} Re(v^T M(\alpha)v) &= Re(v^T(I + \alpha(L - I))v)\\ &= (1-\alpha)Re(v^T I v) + \alpha Re(v^T L v)\\ &> 0 \text{ for } |v| > 0.\end{aligned}$$

Since the matrix M is positive definite for all $0 \leq \alpha \leq 1$ and it also has a positive determinant. (When I prove this link between positive definite and the determinant I used the fact that M has only real values, which must be true since $\dot{x}$ and ∇V are real, it may be possible to drop this restriction.)

Proposition 12. *The dynamic and energy stability are the same.*

Consider the matrix K which is a function of α.

$$K(\alpha) = -M(\alpha)H(x^*) \tag{2.28}$$

When $\alpha = 0$ we have a gradient system and at $\alpha = 1$ we have the Jacobian matrix at the fixed point. Consider the determinant of K as α goes from zero to one. Due to Proposition 11 the determinant of M does not pass through zero as we vary α. Since we chose a fixed point with a nonsingular Hessian, the determinant of $H(x^*)$ is nonzero. Therefore $K(\alpha = 0)$ and $K(\alpha = 1)$ have the same number of stable and unstable eigenvalues. Thus, the Hessian and the Jacobian have the same number of stable and unstable eigenvalues.

2.4.2 Remarks on the proof

1.) Lyapunov's second theorem that says that energy and dynamic stability are the same for completely stable and completely unstable fixed points.

2.) For systems where L is symmetric, there is another way to go about this proof. For example, for a linear system $\dot{x} = -Ax$, $A = A^T$, one can create a new metric $(x, y) = xA^{-1}y$. Recall the gradient is defined by $dG(v) = (v, gradG)$ where $dG(v) = \frac{d}{ds}G(\gamma(s))|_{s=0}$ and γ is a curve for which $\gamma(s \dot{=} 0) = v$ [18]. So,

our gradient is for our A metric is then $gradV = A\frac{\partial V}{\partial x_i}$. Thus, the dynamical system is now $\dot{x} = -gradV$ - a gradient system.[48]

3.) Now that we know this stability result we can simplify the previous stability result on networks of drops. For example, we have a strong Lyapunov function and we knew the stability of the Hessian, so we could have just skipped to the final answer at that point. Also, we know from some simple algebra that U is a satisfactory L, therefore it is positive definite, and its determinant is always positive through any deformation path.

2.5 Conclusions

In capillary driven volume-scavenging the system coarsens until there is only one large drop. A Lyapunov function of the dynamical system ensures the energy (equivalently the area) will decrease monotonically until one of N possible sinks is reached. It is shown that there are a total of $2^N - 1$ fixed points in phase space. For any given fixed point the number of stable and unstable directions is shown to be equal to the number of small drops and large drops less one, respectively. The number of fixed points and their stabilities depends upon the shape of the pressure-volume response curve. There are many responses like the Young-Laplace drop (with a single turning point) that yield the same results. Similarly, it is easy to construct a response that has different behavior [73]. That the final state is always one of the N stable fixed points is confirmed by numerical simulations as well by experiment. The system studied has many similarities with gradient systems. The stability of fixed points can be found by the convexity/concavity of the energy landscape, the energy is a Lyapunov function, and no periodic orbits can occur. This similarity is most clearly seen

in the formulation where network connectivity multiplies the gradient of the energy ($\dot{V} = -U\nabla E$).

CHAPTER 3

VOLUME-SCAVENGING*

3.1 Introduction

Consider the system described in the previous chapter. For a system of N drops with $\overline{V} > 1$, there are N stable fixed points, each corresponding to a different scavenging winner (see Section 2.3). As a result, the phase space will be divided into N basins of attraction which determine the winner for a given initial condition. We seek to understand *how and why the scavenging winner varies with the parameters N, $\overline{V}$, the network connectivity, and the initial condition.*

3.2 Motivational observations

3.2.1 Simulations

Simulations for N drops coupled in a linear network are reported in this section. In this network, the edge drops have only one nearest neighbor, and all others have two nearest neighbors. The governing nonlinear system for the linear ar-

*H.B. van Lengerich, M.J. Vogel and P.H. Steen, Dynamics and Stability of Volume-Scavenging Drop Arrays: Coarsening by Capillarity *Physica D* **238** (2009) pp531-539 Reprinted with permission

rangement of drops is written,

$$\begin{aligned}
\dot{V}_1 &= -P(V_1) + P(V_2) \qquad (3.1a)\\
\dot{V}_2 &= P(V_1) - 2P(V_2) + P(V_3)\\
&\vdots\\
\dot{V}_{N-1} &= P(V_{N-2}) - 2P(V_{N-1}) + P(V_N)\\
\dot{V}_N &= P(V_{N-1}) - P(V_N)
\end{aligned}$$

with corresponding initial conditions,

$$V_j(0) = \overline{V} + \epsilon_j \qquad \text{for } j = 1...N \qquad (3.1b)$$

where ϵ_j is the prescribed deviation from identical initial volumes $\overline{V}$ with $\sum_{i=1}^{N} \epsilon_j = 0$. Here the dot represents a derivative with respect to dimensionless time. This ODE system is a specialization of the more general system defined in Section 2.2.

Two protocols are followed in the simulation experiments. The first protocol is to compute a large number of trajectories, each starting from a random initial condition on the surface of an $(N-1)$-dimensional ball around the source fixed point. A histogram with the frequency of each winner is constructed. We call this the probability-of-winning protocol. For the second protocol, an initial condition ϵ_j for $j = 1...N$ is fixed and the winner is recorded while $\overline{V}$ and N are varied. We call this the change-of-winner protocol. For both protocols, an Euler integration scheme (in MATLAB) with a time step of dt=0.1 is used to integrate System (3.1).

3.2.2 Probability-of-winning

Here, the probability of winning is simulated with $\overline{V} = 1.5$ and for the linear network, $N = 5, 6, 7, 8$. The initial configuration is defined by a set of ϵ_j's randomly chosen on the surface of a ball of radius $\epsilon \sim 10^{-12}$ where $\epsilon^2 \equiv \sum_{i=1}^{N} (\epsilon_j)^2$. System (3.1) is integrated $10,000$ times each from a random initial condition, and the results are summarized in the histograms shown in figure 3.1.

Let $p^N = (p_1, \ldots, p_N)$ denote the probability vector for N drops where p_i is probability of drop i winning. The simulations suggest that $p^5 = (0,\ 1/4,\ 1/2,\ 1/4,\ 0)$. The fact that an end drop never wins can be rationalized by its having only one neighbor to scavenge from. The middle drops have a greater probability of winning, perhaps because they are fed from more drops. The observation that $p^6 = (0,\ 0,\ 1/2,\ 1/2,\ 0,\ 0)$ is consistent with these arguments. One might expect p^7 to be similar to the previous odd configuration, p^5. In contrast, we observe that the center drop has zero probability of winning, $p^7 = (0,\ 1/4,\ 1/4,\ 0,\ 1/4,\ 1/4,\ 0)$. The bimodal distribution that appears at $N = 7$ continues to the distribution p^8 but is further sharpened to yield only two possible winners, $p^8 = (0,\ 0,\ 1/2,\ 0,\ 0,\ 1/2,\ 0,\ 0)$. We found this sequence of distributions surprising, and it drew us to the problem. These results are explained in Sections 3.3.3 and 3.4.1.

3.2.3 Change-of-winner

Here the change-of-winner is simulated for $3 < N < 25$ and $1 < \overline{V} \leq 2.5$ for the linear network. For $j = 1...N$, the initial condition ϵ_j is chosen according to the linear ordering $\epsilon_j = a[2j - (N+1)]/(N-1)$ with the amplitude $a =$

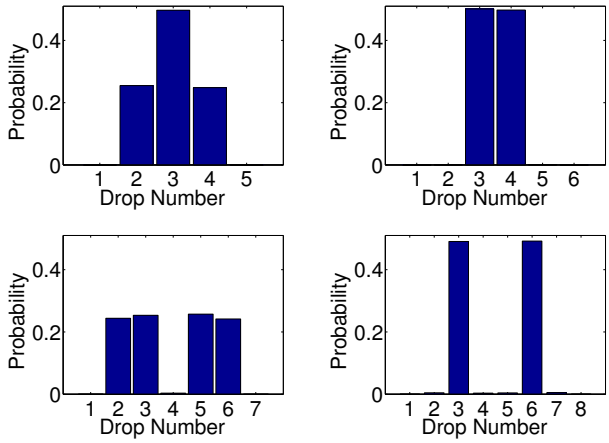

Figure 3.1: Histograms showing the probability for a given drop to win in a linear system for $N = 5, 6, 7, 8$ (as indicated by the abscissa range). The 10,000 initial conditions are uniformly distributed close to the point of identical 1.5 hemispherical drops.

10^{-3}. This perturbation from the $LL \ldots L$ fixed point corresponds to a linear ordering of the volumes from smallest ($j = 1$) to largest ($j = N$) where the extremes deviate from the average drop size by only 0.001 hemispheres. The simulation results can be summarized in a 'phase diagram' (figure 3.2). Since the initial condition is fixed, the phase diagram suggests that the domains of attraction change in a complicated manner as $\overline{V}$ and N vary. The movement of the domains of attraction is explained in Section 3.4.2.

3.3 Domains of attraction

The phase space can be partitioned into N attracting domains, one for each of the stable fixed points. The separatrices of the domains for the reduced system are $N - 2$ dimensional manifolds, which we shall refer to as 'separatrix manifolds'. A separatrix manifold that determines the domain of attraction for the

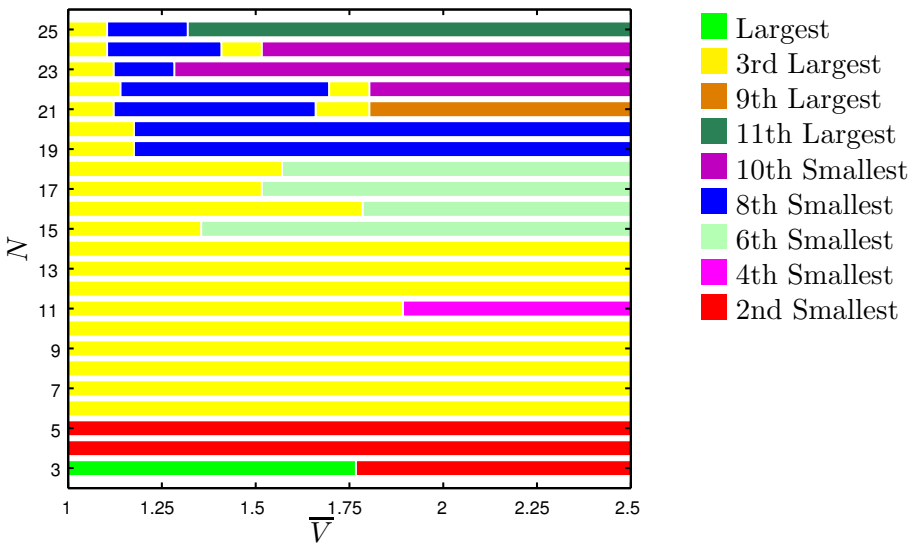

Figure 3.2: Phase diagram showing which drop wins for a fixed initial disturbance.

j^{th} drop winning, must contain all unstable fixed points that have the j^{th} drop being large. The reason for this is that each of these saddle points has a trajectory that decreases energy to make the j^{th} drop small, and a trajectory that makes a large drop other than j small.

Invariant manifolds arising from symmetries of the governing nonlinear equations will be called 'symmetry manifolds.' When symmetry manifolds are hyper-planes they are also separatrix manifolds and can often be found by inspection. We are interested in finding the domains of attraction close to the source fixed point. This is done by combining properties local to the fixed point (the eigenvectors) with the global properties of the symmetry manifolds.

To get a sense of the interaction between symmetry and separatrix manifolds, all possible symmetries of the $N = 3$ case are explored by varying two parameters, c_{13} and c_{12}. The conductances are chosen to be: $c_{12} = c_{13} = c_{23} = 1$ for the *complete/ring*; $c_{12} = c_{23} = 1$ and $c_{13} = 0$ for the *linear/star*; and $c_{23} = 1$,

$c_{12} = 1/2$ and $c_{13} = 0$ for the *skew network*.

3.3.1 Eigenvectors and eigenvalues

The $N = 3$ phase space in figure 3.3 (top) shows the branches of static shapes (dotted lines) for parameter values of $\overline{V} > 1$. Consider a phase plane orthogonal to the $[1, 1, 1]$ direction of the full $N = 3$ system shown in figure 3.3 (bottom). This 'triangular reduced space' preserves the symmetry of the system and will be used henceforth. The transformation from full to triangular reduced space is given by $(x, y) = (V_1 - V_3, \sqrt{3}(V_2 - \overline{V}))$. It can be verified using the vector field that all trajectories cross the triangular boundary inwards. For the $2^3 - 1 = 7$ fixed points the number of unstable and stable directions at a fixed point are $n_L - 1$ and n_S, respectively; this is consistent with index theory [2]. figure 3.3 (bottom) also shows the eigenvectors schematically for the skew network.

Our focus is on initial condition near LLL, therefore we find the eigenvectors and eigenvalues at the source (see Table 3.1). The algebraic degeneracy of the complete/ring network gives a 1-parameter family of eigenvectors (parameter θ). The linear/star network breaks this symmetry and has two unique unstable eigenvalues, as does the skew network.

3.3.2 Symmetry manifolds

A symmetry of the drop system is most easily found from the full system (2.9). Due to the special structure of (2.9) – that the function $P(V)$ is identical for all

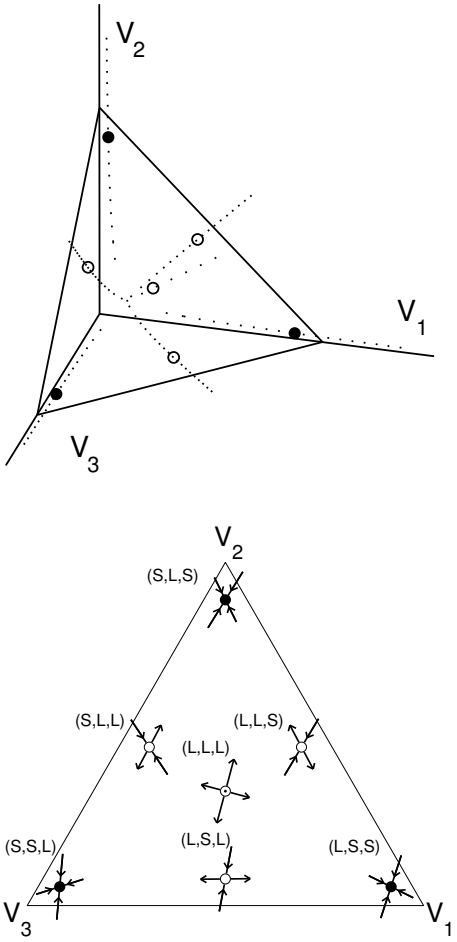

Figure 3.3: Top: Three dimensional phase-space for $\overline{V} > 1$ with branches of fixed points (dashed lines). Bottom: A constant volume slice gives the triangular reduced space. Eigenvectors shown are for a skew network with $\overline{V} = 2$.

drops – symmetries can be found using only the connectivity matrix. Indeed, suppose γ_{kl} is an $N \times N$ matrix representing a permutation of indices (permutations are a natural choice since $P(V)$ is nonlinear). If $\gamma_{kl} c_{lj} = c_{kp} \gamma_{pj}$ (summation convention holds) then it can be shown that γ_{kl} is a symmetry. It is immediate that the fixed-point subspace is flow invariant; that is, V solving $\gamma_{kl} V_k = \delta_{jl} V_j$ is an invariant manifold [40]. For $N = 3$ the complete/ring network has S_3 symmetry. Three one dimensional invariant manifolds due to the symmetry

$N=3$	Complete/Ring	Linear/Star	Skew
Symmetry Manifolds	$V_1 = V_3$ $V_1 = V_2$ $V_2 = V_3$	$V_1 = V_3$	none
Eigenvalues	$\lambda = 3, 3$	$\lambda = 3, 1$	$\lambda = \frac{3+\sqrt{3}}{2}, \frac{3-\sqrt{3}}{2}$
Eigenvectors	$v_1 = (cos\theta, sin\theta)$	$v_3 = (0, 1)$ $v_1 = (1, 0)$	$v_{\frac{3+\sqrt{3}}{2}} = \frac{(1-\sqrt{3},-1-\sqrt{3})}{2\sqrt{2}}$ $v_{\frac{3-\sqrt{3}}{2}} = \frac{(-1-\sqrt{3},-1+\sqrt{3})}{2\sqrt{2}}$

Table 3.1: Symmetry manifolds and eigenvalues and eigenvectors of source fixed point for various $N = 3$ networks with conductances given in Section 3.3.2. Eigenvalues are scaled by $-P'(\overline{V})$, where the prime denotes differentiation with respect to volume. Eigenvectors are expressed in triangular reduced space $(x, y) = (V_1 - V_3, \sqrt{3}(V_2 - \overline{V}))$ and $0 \leq \theta \leq \pi$.

are $V_1 = V_2$, $V_1 = V_3$, and $V_2 = V_3$. For the linear/star case only one invariant manifold can be found from symmetry, namely $V_1 = V_3$. For the skew case the conductances are all different and the nonlinear system has no symmetries. These symmetry manifolds are shown as dashed lines in figure 3.4 (top) and are listed in Table 3.1.

3.3.3 Separatrix manifolds

Symmetry manifolds (global) interact with the eigenvectors (local) to yield the separatrix manifolds, found by integrating system (2.10) backwards in time from an initial condition close to a saddle point (figure 3.4, middle). For the complete network, the degenerate eigenvalues (algebraic multiplicity 2) accommodate the three symmetry manifolds. Portions of these symmetry manifolds ultimately determine the boundary between basins of attraction – the separatrix manifolds. For $N = 3$, the separatrix manifolds are 1D-manifold connections of the source to one of the saddle points. For the linear network, one separatrix

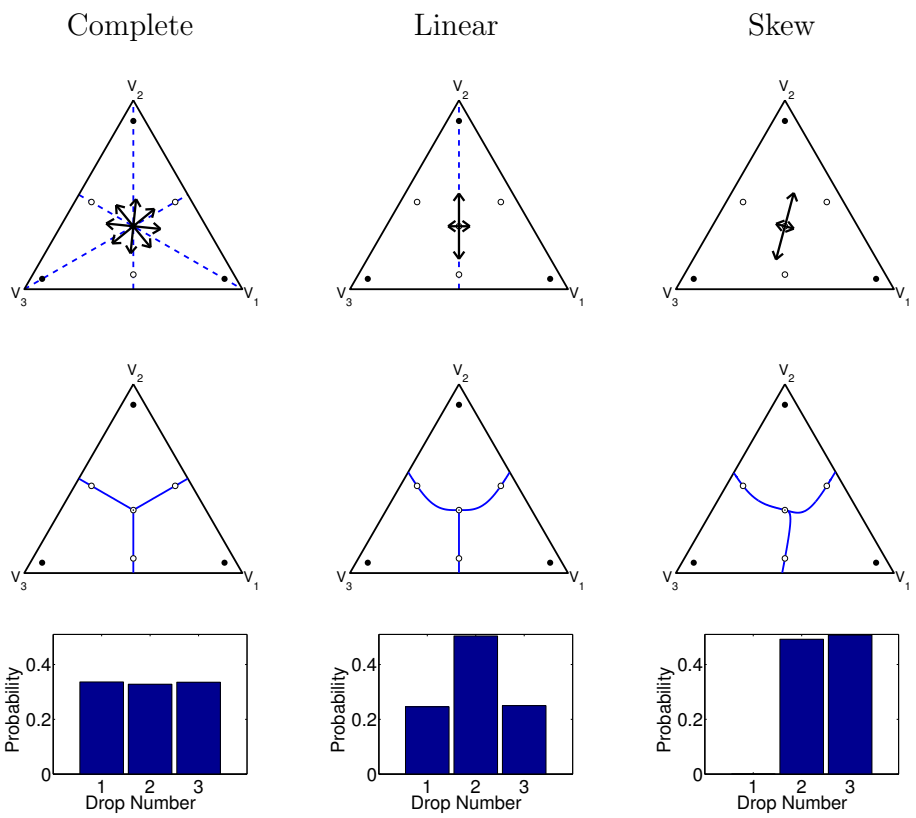

Figure 3.4: Top: Symmetry manifolds (dashed) and eigenvectors of LLL (arrows) in triangular reduced space. Middle: Separatrix manifolds found numerically for $\overline{V} = 2$. Bottom: Probability of winning found numerically as described in Section 3.2.2 (10,000 runs).

manifold is a portion of the symmetry manifold found by inspection, the other two are tangent to the least unstable eigenvector and approach the fixed point along eigen-directions from opposite sides (due to symmetry). For the skew network the eigensystem dominates the determination of the separatrix manifolds – all three separatrices come in normal to the most unstable eigenvector. These observations on how the symmetry manifolds and eigenvectors interact to form the separatrix manifolds near the LLL fixed point are generalized to $N > 3$ by the following formation rules in the reduced space.

Rules of formation of separatrix manifolds. *The portion of an $N-2$ dimensional symmetry manifold leaving the source and passing through a saddle point with exactly one stable direction forms a separatrix manifold. When no such symmetry manifold exists for a given saddle, the separatrix manifold is an $N-2$ dimensional hyper-surface that connects the saddle point to the source where it is normal to the most unstable eigenvector.*

Implications of these rules, for arbitrary N and provided initial conditions are taken sufficiently close to the source, are i) that without any symmetry there are exactly two drops which have equal probability of winning (i.e. the skew case is typical) and ii) that for linear networks one of three symmetric probability distributions must occur: two drops with equal probability, three drops with $p = 1/2$ for the center drop and $p = 1/4$ for two others, or four drops with equal probability. That is, the hyperplane of symmetry is either normal ($\gamma v_u \neq v_u$) or parallel ($\gamma v_u = v_u$) to the most unstable eigenvector. The particular identity of the winning drops is not predicted by the 'Rules'.

3.4 Explanation of computational results

3.4.1 Probability-of-winning

Probability-of-winning is given by the area fraction of initial conditions in each basin of attraction. Such a prediction is possible when the separatrix manifolds are known. For $N = 3$, these predictions are compared to the computational results of figure 3.4 (bottom). For the complete network (subscript c), each drop is equally likely to win for any fair set of initial conditions

($p_c^3 = (1/3, 1/3, 1/3)$). In contrast, for the linear network (subscript l), starting nearby by the source, the middle drop is twice as likely as either of its neighbors to win ($p_l^3 = (1/4, 1/2, 1/4)$), while starting far away (a random initial condition) still favors the middle drop but not as strongly. This difference between nearby (small disturbance) and far (large disturbance) initial conditions is most dramatic for the skew network (subscript s). Starting nearby the source gives zero probability for V_1 to win ($p_s^3 = (0, 1/2, 1/2)$), while for initial conditions far from the source the situation is more favorable to V_1. Note that the skew network can be deformed into the linear network by letting $c_{12} \to 1$ and that the probability of winning is discontinuous in the limit. This discontinuous behavior can be understood immediately from figure 3.4 (middle).

The skew case illustrates how some of the separatrices can be tangent to each other, and therefore drops can have zero probability of winning, such as the edge drops in figure 3.1. The linear case shows that if there is a limited amount of symmetry some of the separatrices come in along the most unstable eigendirection, whereas others come in from less unstable eigendirections. The interaction between this limited amount of symmetry in higher dimensions results in unexpected probability distributions (see figure 3.1); these seem to depend on whether N is even or odd, among other factors.

3.4.2 Change-of-winner

A transition from one winner to another is recorded for a fixed network type in the phase diagram (figure 3.2). Recall that the initial condition is fixed. Such transitions occur when a separatrix manifold crosses the point representing the

initial condition and can be predicted by center-manifold theory [15]. For the $N = 3$ linear network of drops, the separatrix manifold can be approximated using this approach. The calculation uses the reduced system (2.10). The third drop is eliminated and the volume coordinates are shifted such that the origin corresponds to the source. The invariant manifold is found by letting the variable V_2 be a function of V_1 such that

$$V_2 = a_1 V_1 + a_2 V_1^2 + O(V_1^3). \tag{3.2}$$

The coefficients a_i are found by solving

$$0 = \dot{V}_2 - \frac{\partial V_2}{\partial V_1}\dot{V}_1. \tag{3.3}$$

for successive orders of V_2. Equation (3.3) for the linear network has two solutions:

$$(a_1, a_2) = (-2, 0), \tag{3.4a}$$

$$(a_1, a_2) = (0, P''/P'). \tag{3.4b}$$

The first of these coefficient pairs represents the symmetry manifold (vertical solid line, Fig 3.5), the second is an approximation (dashed) to the other symmetry manifold (solid). The separatrix crosses the initial condition at $\overline{V} = 5\sqrt{2}/4 \approx 1.76$. At average volumes $\overline{V} < 5\sqrt{2}/4$ the initial point with linear disturbance lies in the domain of attraction of the third drop, whereas for $\overline{V} > 5\sqrt{2}/4$ the initial condition belongs to the domain of attraction of the second drop, as shown in figure 3.5 (in triangular reduced coordinates).

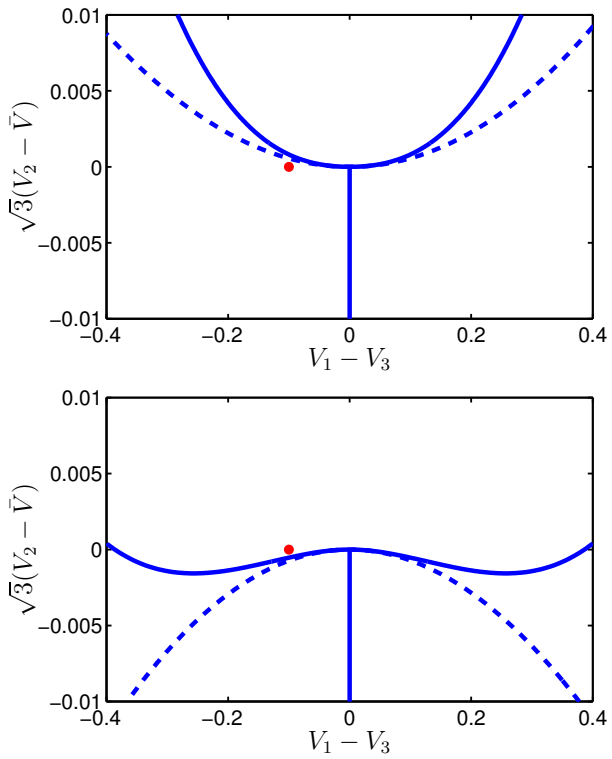

Figure 3.5: Separatrix manifolds computed numerically (solid) and approximated (dashed line), projected onto triangular reduced space. Top is $\overline{V} = 1.66$ and bottom is $\overline{V} = 2$. The initial condition (dot) has been shifted for clarity (actual value: $V_1(0) - V_3(0) = 0.002$).

3.5 Higher dimensional results

The rules for finding the domains of attraction presented in section 3.3.3 can be applied to higher dimensional systems $N > 3$ as well. Results for systems with and without symmetry are shown below.

3.5.1 No symmetry

In the absence of symmetry only the plane perpendicular to the most unstable manifold separates the two domains of attraction in the vicinity of the most unstable fixed point. This is demonstrated numerically in figure 3.6. Here three random adjacency matrices of networks without symmetry for $N = 3, 4$ and 5 are shown. The diagrams show the probability of winning for initial disturbances chosen on a hypersphere of radius r. The probability of winning is proportional to the arclength along the dotted circle. As the most unstable fixed point is approached, two drops each have a 50% probability of winning. As the dimension of the system increases, the disturbance size must be decreased in order to reach this limit. Further away from the fixed point other drops have an increased chance of becoming the winner.

In figure 3.6 it is interesting to note that it is the two drops whose columns of the adjacency matrix have the greatest sums, each share the 50% probability of winning. That is, the two drops that are the most connected end up winning. This makes sense from an intuitive perspective, and it is true for all random networks for which these simulations have been done so far.

3.5.2 Some or full symmetry

When the system has full symmetry then the boundaries of the domains of attraction are all parts of invariant manifolds. More intuitive symmetry arguments can be made about the ring or star network, if an exchange of two drops is a symmetry then these drops must have equal probabilities of winning. Switching two drops always gives an $N - 1$ dimensional invariant manifold in N di-

$$\begin{bmatrix} 0 & 1.4342 & 2.1266 \\ 1.4342 & 0 & 1.5612 \\ 2.1266 & 1.5612 & 0 \end{bmatrix}$$

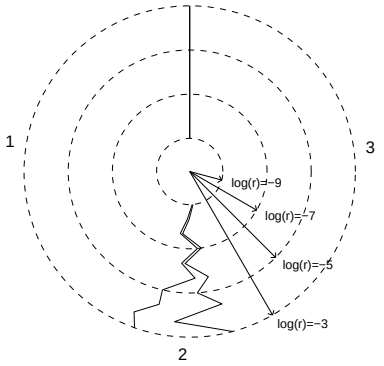

$$\begin{bmatrix} 0 & 0.3973 & 1.5356 & 0.7973 \\ 0.3973 & 0 & 1.2128 & 0.6477 \\ 1.5356 & 1.2128 & 0 & 1.5184 \\ 0.7973 & 0.6477 & 1.5184 & 0 \end{bmatrix}$$

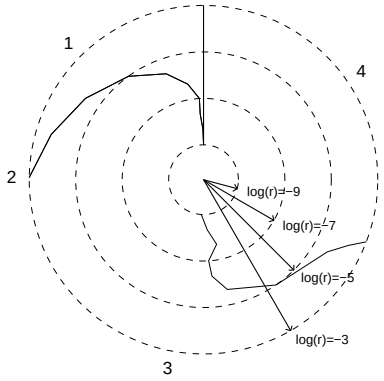

$$\begin{bmatrix} 0 & 1.3907 & 1.0617 & 1.2102 & 1.4026 \\ 1.3907 & 0 & 0.6074 & 1.0497 & 1.0151 \\ 1.0617 & 0.6074 & 0 & 1.0045 & 1.3428 \\ 1.2102 & 1.0497 & 1.0045 & 0 & 1.3145 \\ 1.4026 & 1.0151 & 1.3428 & 1.3145 & 0 \end{bmatrix}$$

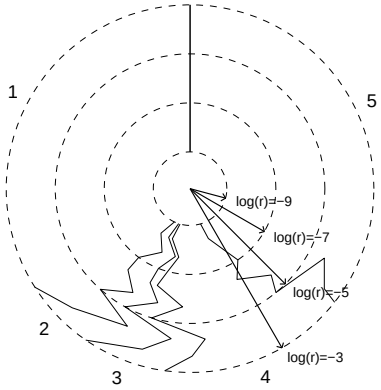

Figure 3.6: Probability of winning for three random conduit networks (no symmetry) for $N = 3, 4$ and 5. The probability of winning is proportional to the arclength along the dotted circle.

mensional space - and it is expected that this manifold separates the two basins of attraction.

Not all types of symmetry yield $N-1$ dimensional invariant manifolds. For example, the flip symmetry of linear networks gives a 1 dimensional manifold for $N=2$, a 2 dimensional manifold for $N=3$, but only a 2 dimensional manifold for $N=4$. That is, the invariant manifold is $[V_1,V_2,V_3,V_4]=[V_4,V_3,V_2,V_1]$, and this does not split the domain into two parts. However, if one considers doing simulations on all initial conditions in the range, then only half of all simulations must be done, as for each initial condition one also obtains the results for the mirror image. Thus it appears there is some kind of $N-1$ dimensional manifold splitting the domain into two parts, but this manifold is not an invariant manifold obtained from a permutation of the indices (for example, it could be a rotational symmetry). If we assume such a symmetry manifold exists for linear networks, then this manifold can either be parallel or perpendicular to the plane perpendicular to the most unstable eigenvector. This gives three possible probabilities of winning, as shown in figure 3.5.2. The three probabilities, $1/4,1/4,1/4,1/4$, $1/2,1/4,1/4$, and $1/2,1/2$ are those observed in figure 3.1, and have been verified for up to $N=12$, although extremely small disturbances must be chosen for such high dimensional systems.

3.6 Conclusions

Through numerical simulations, it is shown that the identity of the winning drop depends on the network connectivity and the total system volume. Networks where each drop is directly connected to all other drops (complete) have

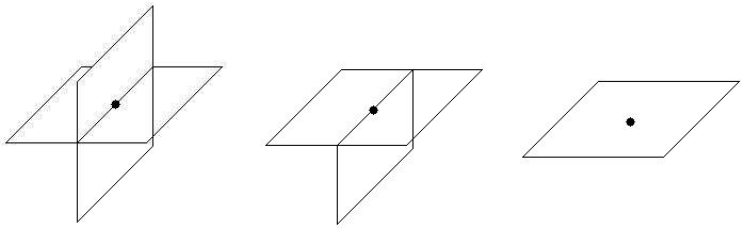

Figure 3.7: Interaction of symmetry manifold with the plane perpendicular to the most unstable manifold centered about the most unstable fixed point.

a maximal symmetry. For these systems, each drop is equally likely to be the winner. As the symmetry of the network decreases, the basins of attraction partition the phase space with decreasing symmetry. For a linear network this can yield a unimodal or bimodal histogram (figure 3.1). To find the basins of attraction analytically, a rule for the formation of separatrix manifolds is proposed. This rule uses only information from invariant manifolds due to symmetry and the eigenvectors of the source fixed point. Since the drop response is identical for all elements, the asymmetry depends only on the connectivity network and is decoupled from the nonlinearity of the problem. At the source all drops have identical volume, so the eigenvectors can also be found using only the c_{ij} matrix.

The reader might naturally ask how the theory developed in this paper can be used to gain insight into the experiment of figure 2.1. The exact connectivity network is unknown. For flow through only the porous frit the resistance is expected to be proportional to the distance between drops. However, if the liquid exchange occurs primarily in the space below the frit, so that the majority of the flow through the frit is in the vertical direction, then a complete connectivity network would be a good model. Note that the winning drop does not

appear to be the largest initially (figure 2.1 i), from which one may infer that most of the liquid is transferred horizontally through the porous frit. Contrary to the simulations for linear networks (figure 3.1), an edge drop wins. This is due to the non-ideality of the experimental system. The internal geometry of the apparatus causes the edge drops to be significantly larger than those in the interior. That is, the system likely did not start very close to the $LL\ldots L$ fixed point. The situation is analogous to picking an initial condition in the lower part of the reduced triangular space for the linear network (figure 3.4 Middle). Additionally, the hole radii vary slightly and this would cause the larger radii holes to have higher probabilities of winning. In short, the experiments are not sufficiently controlled to illustrate features beyond the coarsening competition that ends with one drop taking all the volume.

The results regarding the stability and dynamics of the drop system are general and could be applied to other systems. The 'unisignant' gradient system gives a simple way to find the signs of all the eigenvalues. It was shown that the formation rule regarding the separatrices can give insight into the end state that a system evolves to. Finding the domains of attraction for higher dimensions systems is more difficult because of the low dimensional symmetry manifolds that arise. There appear to be manifolds separating the space which are not invariant manifolds from symmetry. It is also difficult to label the domains of attraction to the correct winner; this has been done by visual inspection for $N = 3$, and an intuitive argument for systems without symmetry was also made. Correctly labeling the domains of attraction, and then approximating them with center manifold theory would allow the results in figure 3.2 to be predicted.

CHAPTER 4

COARSENING DYNAMICS*

4.1 Introduction

A system of spherical-cap drops coupled by a network of uniform conduits will coarsen as the capillary force causes some drops to gain volume at the expense of others. We consider a system of n drops. Each has contact-line pinned on identical circles of radii B. The pressure P of each drop is related to the volume V through the surface tension σ by the Young-Laplace equation, cf. figure 4.1. The difference in pressure between drops drives the flow through the conduits. This system is dominated by viscous and surface tension forces (small Bond, Weber, and Reynolds number), and the dissipation within the drop is negligible compared to that through the conduits. The system is started close to a state of almost identical super-hemispherical drops (referred to as 'large' henceforth) and coarsens as some drops become sub-hemispherical (referred to as 'small' henceforth) by giving volume to the remaining large drops. The surface area is a maximum value initially and decreases monotonically until a only a single large drop remains [95]. We seek coarsening laws which predict the number of large drops n_ℓ as a function of time.

A simple experiment illustrates capillary coarsening cf. figure 2.1. A 4×6 array of holes is drilled in a plate. The plate is sealed along its outer edges to a reservoir below and the total volume of water in the reservoir and the drops is controlled by a syringe pump. Initially, by pumping with the syringe, 24 drops

*H.B. van Lengerich, M.J. Vogel and P.H. Steen, Coarsening of capillary drops coupled by conduit networks submitted to *Phys. Rev. E*

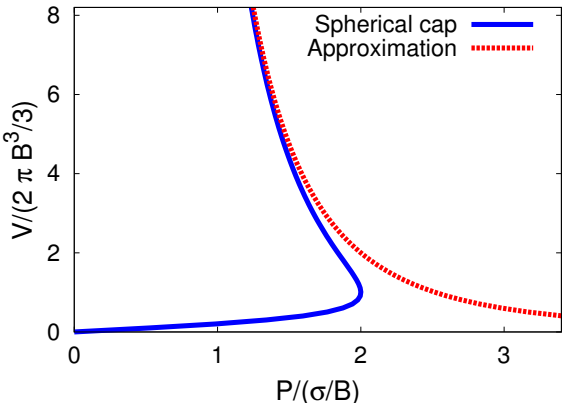

Figure 4.1: Exact pressure-volume response of a single spherical-cap drop (solid/blue). Approximate response of a full sphere works well at large volumes (red/dashed). In this figure only, pressure is scaled by σ/B and volume by $2\pi B^3/3$.

are caused to protrude to large volumes. Pumping is then stopped, the total volume fixed, and coarsening ensues. The number of large drops decreases, while the distance between large drops and the difference in volumes between large drops increase.

Coarsening of spherical-cap drops has a central role in the strength of adhesion, both before and after grabbing, for a grab-release adhesion device that we have designed and built [97]. This device, inspired by a leaf beetle [33], uses surface tension to grab onto and release from a substrate. The device works on a principle of parallel action; when many large drops of similar sizes are brought close to a substrate they form liquid bridges, and the total adhesion force is the sum of the forces of individual bridges. Before grabbing, coarsening redistributes liquid in the drops which can decrease the number of bridges formed and, thereby, decrease the total initial adhesive force. After grabbing, the bridges may coarsen over longer time-scales which also changes the adhesion. Our focus is on drops, but coarsening of bridges can be studied with a

similar approach. Another application where coarsening of capillary drops has been utilized is in microfluidic devices where surface tension forces are used to pump fluid through conduits [103]. This method is attractive in the life sciences due to its compatibility with existing technologies [70]. Although we shall discuss a model of the experiment, figure 2.1, our main interest in this paper is capillary coarsening as a prototype for more general coarsening processes [12, 69, 78, 79].

A numerical simulation of the coarsening of $n = 100$ drops in figure 4.2 shows the volume of each drop as it varies with time. To observe the coarsening rate, we prefer to plot the time course of the number of large drops n_ℓ as a fraction of the total number n (inset, figure 4.2). At the start, as the disturbance grows from the unstable equilibrium, there is a plateau where $n_\ell \sim n$ after which there is a transient $1 < n/n_\ell \lesssim 4$ until a coarsening regime develops during which time $(n/n_\ell)^\beta \sim t$, with some exceptions to power-law growth, as we shall discuss below. The coarsening exponent β and the constants that make this expression an equality are the focus of this paper. At the end of coarsening, as a single drop emerges to take all the volume and the final equilibrium state is slowly approached, there is another plateau where $n_\ell \to 1$. The initial and final plateaus can be studied using standard linear stability analysis, while the transient that leads to the coarsening regime is more complicated; this coarsening regime is our focus. In this paper we will compare numerical simulations to derived scaling laws.

The time to transfer volume depends on the flow rate through the conduits. Suppose the flow rate Q is driven by a pressure difference ΔP against resistance due to liquid viscosity μ. For a single conduit of hydraulic radius R and length

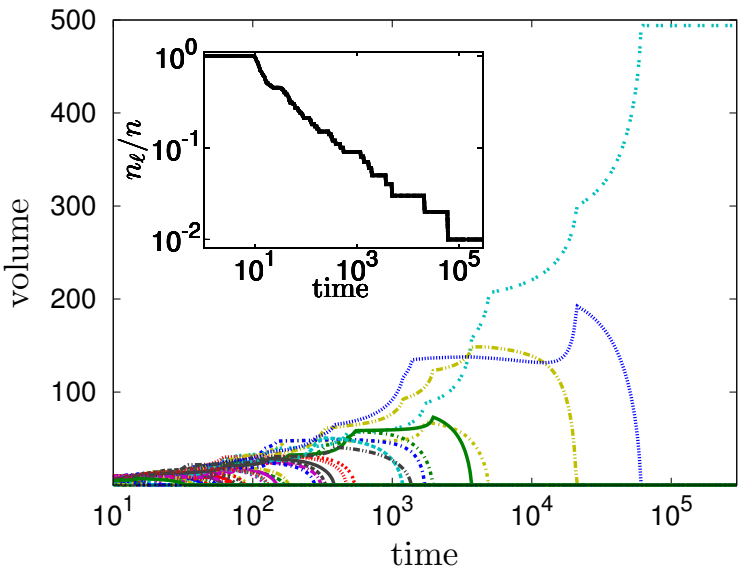

Figure 4.2: A single numerical simulation of a linear network with 100 drops, where the initial disturbance is randomly chosen from a hypersphere of radius $r_0 = 0.1$ centered about identical drop volumes of five hemispheres. Inset: n_ℓ/n against time. Volume is in hemispheres, time in scale T_{on}, defined in text.

L, $Q \sim R^4 \Delta P/\mu L$ (e.g. Hagen-Poiseuille flow). For a system of two drops coupled through a single conduit and otherwise isolated, the flow rate will change due to changing ΔP since the capillary pressure of the drops varies as volume is drained from the smaller to the larger drop. In the two drop system, ΔP scales as $\sigma/V_0^{1/3}$, where V_0 is the average volume of the drops. When many drops are connected through a network, the relevant driving pressure is that across nearest *large-volume* neighbors ΔP_ℓ. The relevant resistance depends on the network of paths available to move volume between these neighboring large drops and the distance W between large drops. More precisely, the flow rate between the large drops depends i) on the pressure drop between nearest large neighbors which depends on the extent of coarsening n/n_ℓ through the volume-difference of nearest large drops and ii) on the resistance between large drops which de-

pends on the extent of coarsening through W, and on the network topology though the arrangement of conduits separating large drops. This suggests the following scales, $\Delta P_\ell \sim (\sigma/V_0^{1/3})h_1(n/n_\ell)$ and $W = Lh_2(n/n_\ell)$, where functions h_1 and h_2 of n/n_ℓ are unknown at this stage. For drops connected in a line, it follows that $Q \sim R^4\Delta P_\ell/\mu W$ and, finally, that a characteristic coarsening time V_0/Q scales as $\mu L V_0^{4/3}/\sigma R^4 h_3(n/n_\ell)$ where h_3 is (yet another) dimensionless function of n/n_ℓ, unknown for now. We may summarize by defining a time-scale, useful for all networks considered,

$$T \equiv c\mu L V_0^{4/3}/\sigma R^4. \tag{4.1}$$

Here, we have added a dimensionless constant c which depends on prescribed network type and dimension. We shall specify c when we specify the network connectivity in Sec. 4.2 and this will facilitate the final dimensionless formulation. Closely related to the network of Hagen-Poiseuille conduits is a Darcy porous medium (permeability κ). It turns out that the above time scale is suitable for porous media provided the hydraulic radius is defined through the geometric mean of B^2 and κ, $R^2 \equiv (B^2\kappa)^{1/2}$. The main subject of this paper may now be stated as the determination of the dependence of coarsening time on the dimensionless group n/n_ℓ.

We study two kinds of coupling conduits (figure 4.3). Orthogonal networks (ON) have identical conduits and fractal networks (FN) have conduits of varying length. The unit cell of an ON has a drop at the origin of and conduits aligned along the coordinate axis of a d-dimensional Cartesian space. This unit cell does not repeat forever; the network is bounded. An ON with $d = 1$ corresponds to a 'linear array', $d = 2$ to a 'square lattice', and so forth. Here, all but the drops at the boundary are connected to $2d$ other drops. A 'completely connected' ON has dimension $d = n - 1$ with periodic boundary conditions along

each dimension; each drop is directly connected to every other drop twice. FN can take on any fractal dimension d_f by adjusting the ratio of lengths of the conduits. Both d and d_f in these networks are consistent with the 'similarity dimension' [90]. We note that the dependence of coarsening rates on the dimension of the system has been studied in a diverse range of systems (see [9, 83], and references therein) but we are not aware of any previous work regarding fractal networks.

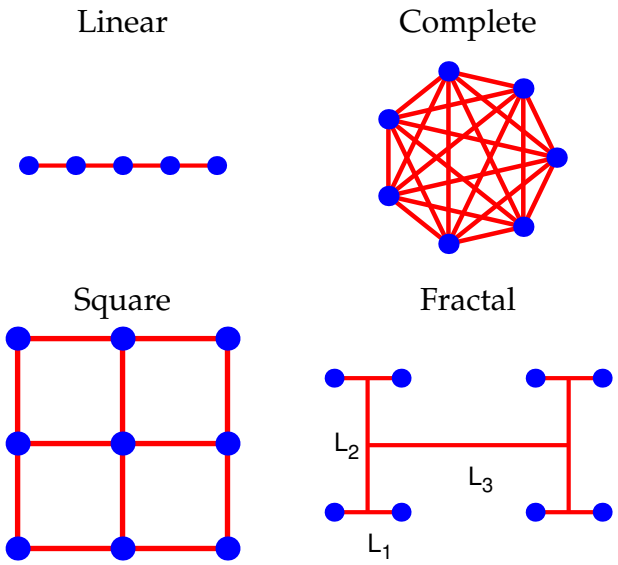

Figure 4.3: Linear ($d = 1$), square ($d = 2$), complete ($d = n - 1$), and fractal (fractal dimension d_f) networks of conduits connecting drops. Complete network has been flattened from $d = 6$, therefore the conduits appear to have unequal lengths; periodic boundary conditions for this network means each line represents two conduits.

The adhesion device design, shown in cross-section in figure 4.4, has a porous medium (PM) adjacent to the top plate to slow the coarsening time. This design consists of a large number of orifices with radii B and center-to-center distances L, below which is a membrane or frit of thickness H_F and Darcy permeability κ_F, and below that is a water reservoir of thickness H_R. Two limiting

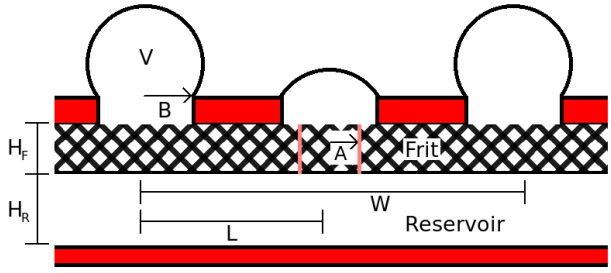

Figure 4.4: Sketch of adhesion device while coarsening. The height of the frit is H_F; reservoir depth H_R; distance between nearest drops L; and distance between nearest large drops W. For flow horizontal through the a porous media region, the pressure of the drop is applied at a radius A to account for the vertical flow entering from the orifice of radius B.

cases of drop coupling may be identified: (i) flow vertically through the frit and then horizontally through a low-resistance reservoir and (ii) flow only horizontally through the frit. Additionally, fabrication defects can allow drops to communicate through gaps between the frit and the top plate. Scenarios (i) and (ii) are further discussed in Appendix E. We model the coupling of the first case by a complete network. The second case and the coupling through a defect region are modeled with flow through a PM between drops arranged in a linear or square configuration. This study is motivated by the question 'can the coarsening exponent distinguish between cases (i) and (ii) (eg. detect a defect)?'.

Classical studies of coarsening of conserved quantities have focused on two types of governing equations. One type is a backwards heat equation plus a higher-order (usually biharmonic) term, such as the Cahn-Hilliard equation. This equation occurs in applications such as spinodal decomposition [12, 88] and dewetting of thin films [39, 91]. The higher-order term leads to a non-zero most unstable growth rate which determines the early stage of the coarsening

into different phases [12, 91]. The cluster size of the two phases grow at the late times due to coalescence of clusters [39, 41, 88, 64]. The second type of governing equation is a discretized backwards heat equation. This equation is ill-posed in the continuum limit, where the most unstable mode has zero wavelength, but in a system with discrete elements the system can be posed as a set of ordinary differential equations. This type of equation arises in granular mechanics [94, 69, 106], image enhancement [79], population dynamics [78], as well as the drop coarsening that we study. The methods used to find coarsening rates and size distributions are similar for both partial and ordinary differential equations. Rigorous upper bounds on the decay of energy have been found for both Cahn-Hilliard type equations [56] and discrete backwards heat equations [34].

In this work we study orthogonal and fractal networks, both of arbitrary dimension, as formulated in Sec. 4.2. A coarsening law is derived for each of these networks in Sec. 4.3. For networks such as the square, the rates are not simple exponents, and logarithmic terms arise. The coarsening laws are then compared to simulation of the exact equations. The derived laws predict the correct functional relation between pre-exponential factors and the number of drops n, the initial volume, and the size of the disturbance. The distribution of the large drops is predicted in Sec. 4.4. Although the growth rate of large drops depends on the network, the distribution of the large drops for all networks collapses onto one curve.

4.2 Governing Equations

We write three types of governing equations to capture the various conductivities between drops described above. The simplest is an ODE model of drops coupled in orthogonal networks (figure 4.3). Alternatively, a model of drops coupled by a Darcy porous medium is constructed (cf. figure 4.4). This model involves solving a PDE, but we will show in Sec. 4.3 that the coarsening law is identical to that for the network of orthogonal conduits. Finally, we consider a fractal network (cf. figure 4.3) where by changing the lengths of the conduits, one can achieve a range of coarsening exponents.

4.2.1 Orthogonal networks

Consider a system of drops coupled by a d-dimensional network of orthogonal conduits. The change in the volume of drop i is determined by the flow through the conduits connecting it to its adjacent neighbors

$$\dot{v}_i = \frac{1}{2d} \sum_{k}^{2d} q_{k,i} \text{ for } i = [1, \ldots, n] \tag{4.2}$$

where the sum over k denotes the $2d$ nearest neighbors of drop i. The dot is a derivative with respect to time and $q_{k,i}$ denotes the volumetric flow rate from drop k to drop i. All the variables have been made dimensionless, with scales V_0 for volume, T_{on} for time and $V_0/(2dT_{on})$ for flow rate (see below in this paragraph for definition of T_{on}). The factor of $2d$ has been added so that when the number of connections to drop i is varied through the network dimension d, and the total dimensional flow rate to a drop i is held constant, then the dimensionless variable $q_{k,i}$ also remains constant. We use a no-flux condition at the edges

for linear and square networks and use a periodic boundary condition for completely connected networks, as mentioned. For example, for a linear network the sum at the edges is over just one element (rather than two). The flow rate between any two drops is assumed to be a linear function of the pressure drop

$$q_{k,i} = p(v_k) - p(v_i) \tag{4.3}$$

where the capillary pressure of an average sphere $2\sigma/(3V_0/(4\pi))^{1/3}$ has been used to scale the pressure. From here on we assume fully developed Hagen-Poissuelle flow so that the flow rate $Q = (\pi/8)R^4(P_k - P_i)/\mu L$. This determines the *time-scale* $T_{on} \equiv c\mu L V_0^{4/3}/\sigma R^4$ where $c = 6^{1/3}/(d\pi^{4/3})$, consistent with equation (4.1). Combining Eqs. (4.2) and (4.3) gives a set of ordinary differential equations for the volume of the drops

$$\dot{v}_i = -p(v_i) + \frac{1}{2d}\sum_{k}^{2d} p(v_k), \tag{4.4a}$$

aps with corresponding initial conditions

$$v_i(t=0) = 1 + \epsilon_i/v_0, \tag{4.4b}$$

where k denotes drops adjacent to i, v_0 is scaled by a hemisphere $2\pi B^3/3$, and ϵ_i is an n dimensional vector assigning to each drop a randomly chosen volume (in hemispheres) from the surface of an n dimensional hyper-sphere of radius $r_0 = \sqrt{\sum \epsilon_i^2}$ with the constraint $\sum \epsilon_i = 0$. Simulations of Eqs. (4.4) use the exact pressure behavior of spherical-cap drops (cf. figure 4.1), available in closed form. Note that the length scale B enters the scaling only through the initial conditions [equation (4.4b)] and since the initial conditions have 'washed out' by the coarsening regime, the coarsening rate is independent of B, contrary to the case for porous media, described next.

4.2.2 Porous media

Consider a system of drops protruding from a d-dimensional surface, arranged in an orthogonal grid, with the drops coupled through a Darcy porous medium below the surface (cf. figure 4.4). Recall that the Darcy's law has the fluid velocity proportional to pressure gradient with a coefficient κ/μ, where κ is the Darcy permeability of the porous medium and μ the fluid viscosity. Scaling the typical flow velocity by flow through the orifice, $V_0/(\pi B^2 T_{pm})$, time by T_{pm}, pressure by $2\sigma/(3V_0/(4\pi))^{1/3}$, and L for the gradient length-scale, the dimensionless Darcy's law becomes

$$u = -\nabla p, \tag{4.5}$$

provided the *time-scale* $T_{pm} \equiv c\mu L V_0^{4/3}/B^2\kappa\sigma$ is chosen with $c = 3^{1/3}/(2^{5/3}\pi^{4/3})$. This corresponds with equation (4.1) for $R^4 = B^2\kappa$. Inserting Darcy's law into the continuity equation gives

$$0 = \nabla^2 p \tag{4.6}$$

The boundary conditions to this equation are determined by the pressures of each of the drops. The pressure of a drop $p(v_i)$ is specified at a dimensionless 'cut-off' radius $a \equiv A/L$ from the center of the base of drop i, to account for the finite orifice area πB^2 where the drop joins the frit (cf. figure 4.4). This cut-off distance scales with the orifice radius $A \sim B$. To simplify the formulation we assume the flow through the frit happens in the same number of dimensions as the arrangement of drops. Therefore, the spherical hyper-shell at which the pressure is applied is $d-1$ dimensional, consistent with the Laplacian in equation (4.6) which is d dimensional. The evolution of the volume of drop i can be

obtained by a balance of a shell of radius a to give

$$\dot{v}_i = -\int_{\Omega_i} u \cdot n_i ds \tag{4.7}$$

where the surface Ω_i of radius a and normal vector n_i depend on d. The dimensionless surface area Ω_i is scaled by the orifice area πB^2. Once the volume of the drops are specified, the pressure field can be solved using equation (4.6) and the volumes can be iterated using equation (4.7). The initial condition can be specified in terms of drop volumes, as in equation (4.4b).

4.2.3 Fractal networks

We formulate the governing equations for a system of $n = 2^{s_n}$ drops arranged in a fractal configuration (for $s_n = 3$, see figure 4.3). The length of the shortest conduits is L_1, the length of conduits that connects the midpoints of two L_1 segments is L_2, and so on for all s_n lengths. The lengths are scaled by the shortest length $l_i = L_i/L_1$, thus $l_1 = 1$. The governing equations are constructed by first writing a balance equation on the volume of all n drops assuming we know the pressures $[p_a, p_b, ...]$ at the intersection of the l_1 and l_2 conduits. For example

$$\begin{aligned} \dot{v}_1 &= \frac{2}{l_1}(p_a - p_1) \\ \dot{v}_2 &= \frac{2}{l_1}(p_a - p_2) \\ &\vdots \end{aligned} \tag{4.8}$$

Scales for volume, pressure, and volumetric flow rate are the same as for orthogonal networks. Each drop is connected to only one conduit, therefore the time scale corresponds to that of the ON with $d = 1/2$. The *time-scale* $T_{fn} \equiv c\mu L_1 V_0^{4/3}/\sigma R^4$ with $c = 2 \times 6^{1/3}/\pi^{4/3}$ results.

To determine the pressures at the intersections $[p_a, p_b, ...]$ we write a volume balance around all the intersections of conduits of length l_1 and l_2. For example, a balance about the midpoint of drops 1 and 2 gives

$$0 = \frac{2}{l_1}(p_1 - p_a + p_2 - p_a) + \frac{2}{l_2}(p_b - p_a) \tag{4.9}$$

where p_b is the pressure at the midpoint of the conduit of length l_2 connecting the conduit of length l_1 from above, to another conduit of length l_1. Balances of the form of equation (4.9) are written with a recursive code for all $n-2$ intersections, giving $n-2$ equations for $n-2$ unknown intersection pressures. By solving for all intersection pressures in terms of drop pressures we obtain a system of n equation for the dynamics of the drops:

$$\dot{v}_i = \sum_{j=1}^{n} c_{ij}(p_i - p_j) \tag{4.10a}$$

$$v_i(t=0) = 1 + \epsilon_i/v_0 \tag{4.10b}$$

where c_{ij} is the adjacency matrix of the conduit network and ϵ_i and v_0 are as for orthogonal networks. Numerical simulation of Eqs. (4.10), like Eqs. (4.4), uses the exact pressure relation of spherical-cap drops (cf. figure 4.1). To obtain self-similar networks, we set the lengths of the conduits as

$$\begin{aligned} l_1 &= 1 \\ l_i &= \omega^{i-2}(\omega - 1) \text{ for } 2 \leq i \leq s_n \end{aligned} \tag{4.11}$$

where $\omega \geq 1$. When one drop is eliminated from the end of each conduit of length l_1, the system can be rescaled by ω and overlaid on half the original image. This elimination of half the large drops and rescaling by ω can be done for all s_n lengths. Therefore [90], the fractal dimension is

$$d_f \equiv log(2)/log(\omega). \tag{4.12}$$

This dimension (the 'similarity dimension') can be used to recover the dimension d of the ON [90].

4.3 Coarsening Rates: Heuristic predictions and simulation results

A heuristic argument can be made to find the number of large drops as a function of time. To do this, we write an equation for the evolution of a typical growing large drop at some intermediate time. We assume the large drops are evenly distributed in space, because any more closely spaced large drops will more quickly coarsen due to the lower resistance between them. A typical large drop will be connected to other large drops a dimensionless distance $w \equiv W/L$ away. Small drops cannot become large as no drop can have more pressure than a hemisphere. Therefore, the majority of the flow transferred to a (growing) large drop must originate from another (shrinking) large drop. We can solve for the pressure profile below the small drops to calculate the resistance to flow between large drops. The coarsening rate will depend on the network resistance through w and on the network connectivity.

4.3.1 Orthogonal networks: large drop growth

The resistance between two large drops in an orthogonal network will be determined by the flow through a network of conduits below the small drops (since small drop growth is negligible, $\dot{v}_s \approx 0$). Substituting this into equation (4.4a) gives a standard discretized version of the Laplace equation which, for large w,

takes the continuum form,

$$0 = \nabla^2 p, \tag{4.13}$$

For linear networks, this approximation is true for all w since the solution to Laplace's equation is identical to that for discrete resistors in series. For square networks, a comparison against discrete resistors shows that it also works well down to very small w (figure 4.5).

Next, we solve equation (4.13) in radial coordinates with one drop at the origin and $2d$ drops at a distance w. The boundary condition for the drop at the origin is $p(r = a) = p_\ell$. The pressure at the nearest-neighbor large drops at a distance w is set to the mean-field pressure p^*. Therefore the pressure at the surface of the disk of radius $w/2$ is $p(r = w/2) = (p^* + p_\ell)/2$. Applying these boundary conditions we obtain

$$p = \frac{1}{2}\frac{p_\ell - p^*}{a^{2-d} - (w/2)^{2-d}}\left(r^{2-d} - a^{2-d}\right) + p_\ell \text{ for } d \neq 2 \tag{4.14a}$$

$$p = \frac{1}{2}\frac{p_\ell - p^*}{\ln(a) - \ln(w/2)}\left(\ln(r) - \ln(a)\right) + p_\ell \text{ for } d = 2. \tag{4.14b}$$

Evaluating this expression at the location of the nearest-neighbor drops ($r = 1$) and inserting this into the dynamical system for the orthogonal networks (4.4a) gives

$$\dot{v}_\ell = \frac{1}{2}\frac{p_\ell - p^*}{a^{2-d} - (w/2)^{2-d}}(1 - a^{2-d}) \text{ for } d \neq 2 \tag{4.15a}$$

$$\dot{v}_\ell = -\frac{1}{2}\frac{p_\ell - p^*}{\ln(a) - \ln(w/2)}\ln(a) \text{ for } d = 2. \tag{4.15b}$$

In the limit $a \ll 1$, growth of large drops is given by

$$\dot{v}_\ell = \frac{p^* - p_\ell}{2(w/2)^{2-d}} \text{ for } d = 1 \tag{4.16a}$$

$$\dot{v}_\ell = \frac{p^* - p_\ell}{2} \text{ for } d \geq 2. \tag{4.16b}$$

For $d = 1$, the resistance between drops of a distance w is equal to w, as the resistors add in series. From equation (4.15a) we see that this corresponds to $a = 0$. For $d > 2$, a is negligible for a different reason. There, the exponent on a makes the equations in the limit of small a more accurate. For $d = 2$ the approximation is least valid, and therefore, we will leave a in the prediction of the coarsening rate. The value of a is determined by comparing the resistance through a diamond-shaped domain to the resistance given by equation (4.15b), cf. figure 4.5. A value of $\ln(a) = -1.7$ is found as a best fit to match the resistance in a continuous porous medium with a discrete network model.

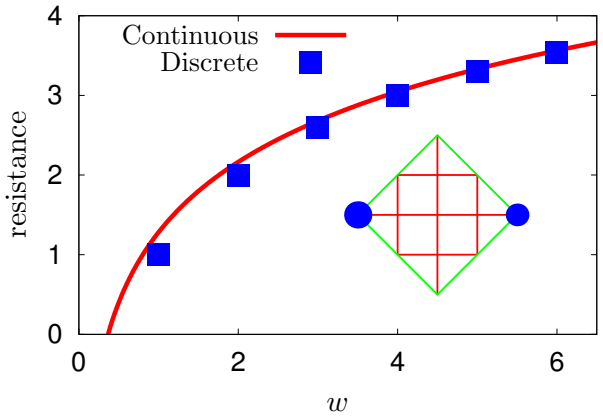

Figure 4.5: Network resistance for flow between two drops in square network: continuous (solid) vs discrete (squares) resistance. The continuous curve is fit to the discrete curve with a value of $\ln(a) = -1.7$. Inset: diamond-shaped domain through which flow travels for $w = 4$.

4.3.2 Porous medium: large drop growth

For the porous medium, start by noting that equation (4.13) also governs the pressure in porous media [cf. equation (4.6)]. Applying the same boundary conditions as for the orthogonal networks leads to the same solutions, Eqs. (4.14),

for the pressures. We then insert the pressure profiles [Eqs. (4.14)] into equation (4.5) and equation (4.7) and observe that, by rescaling the time with scales,

$$T^*_{pm} \equiv T_{pm} \frac{1 - a^{2-d}}{(2-d)\int_{\Omega(r=1)} ds} \text{ for } d \neq 2 \tag{4.17a}$$

$$T^*_{pm} \equiv T_{pm} \frac{-\ln(a)}{\int_{\Omega(r=1)} ds} \text{ for } d = 2, \tag{4.17b}$$

one arrives at Eqs. (4.15). Here, the subscript on the integral indicates the radius of the surface is unity. In summary, the equations for the growth of large drops are the same for the porous medium and orthogonal networks. The main difference is that, for networks, a is a fixed quantity and, for porous media, it is a material parameter that depends on the ratio of B/L as well as the exact experimental setup. The close relationship between ON and PM has been anticipated by [57], among others [93]. It is included here for completeness and because of its relevance to the motivating application. The pressure in hexagonal, triangular, and other regular networks are also determined by a d dimensional Laplace equation (cf. [57]); the dynamics of drops on these networks are equivalent to those on ON and PM modulo a change in the time scale.

4.3.3 Orthogonal networks and porous media: prediction and simulation

We can now calculate the coarsening rates from Eqs. (4.15b), (4.16a) and (4.16b) (for $d > 2$). The majority of the volume is in the large drops and the total volume of the system is constant, therefore

$$v_\ell n_\ell \approx n, \tag{4.18}$$

regardless of network topology. For all large drops the pressure can be approximated as

$$p_\ell \approx v_\ell^{-1/3} \tag{4.19}$$

which is the pressure of a sphere. This approximation is more accurate for larger volumes, as shown in figure 4.1. The large drops dominate the dynamics, therefore the mean-field pressure should depend on the pressure of the large drops. For simplicity we choose the mean field pressure to be directly proportional to the pressure of the large drop

$$p^* = (1+\delta)p_\ell \tag{4.20}$$

where δ is undetermined.

For linear networks ($d = 1$), after turning 'approximate' relationships into 'equality,' (to simplify notation) we insert (4.18), (4.19), (4.20) as well as a relation between the distance of large drops $w \approx n/n_\ell \approx v_\ell$ into equation (4.16a) and integrate to give

$$\left(\frac{n}{n_\ell}\right)^{7/3} - 1 = \frac{7}{3}\delta t. \tag{4.21}$$

The lower bound of integration has a negligible effect and was chosen to be zero for convenience. This coarsening law not only gives us the time it takes for small drops to coarsen, it also includes the dependence on the total number of drops, and shows no dependence on initial disturbance size and initial volume . These dependencies are verified against numerical simulations of equation (4.4) shown in figure 4.6. The value of the mean-field pressure determines the intercept in the coarsening plot; a value of $\delta = 0.15$ was used to match the simulation results. The value of δ did not need to be adjusted when r_0, v_0, or n was varied.

Numerical integration of equation (4.4) (cf. figure 4.6) show that the initial coarsening rate is slower, and then faster, than that which is predicted. For smaller disturbances, the time until the first large drop becomes small increases. As the size of the disturbance r_0 decreases the initial condition is getting closer to an unstable fixed point, therefore it takes longer to escape the neighborhood of the fixed point and start to coarsen. Once the first drop becomes small, many others quickly follow. The validity of the heuristic coarsening law at early times is related to the distribution of large drop volumes, discussed in Sec. 4.4. The initial time is exaggerated by the log scale; discrepancies between the theory and experiment at initial times have a negligible effect on the long-time coarsening.

We do not observe any effects from the finite size of the network. As the number of drops is increased, a smaller fraction of drops are affected by the boundaries, however, the numerical data collapses onto a single curve for the three values of n simulated.

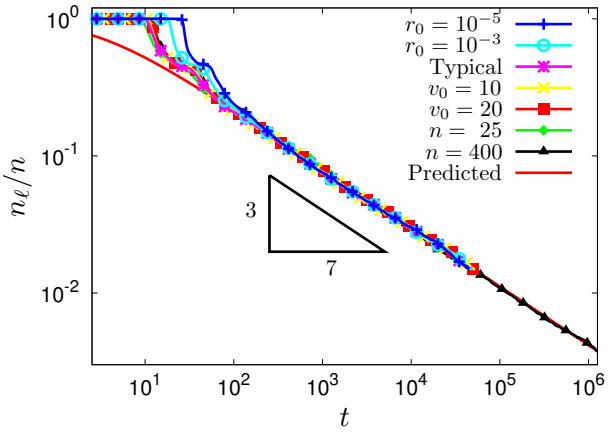

Figure 4.6: Coarsening of linear network according to equation (4.21). Simulations for $n = 100$, $r_0 = 0.1$, and $v_0 = 5$ (typical), unless otherwise noted in legend. Each simulation curve is an average of 100 simulations each with random initial condition. Simulations are cut off before they reached steady state for presentation purposes

.

For orthogonal networks where $d > 2$ and $a \ll 1$ we insert Eqs. (4.18), (4.19), and (4.20) into equation (4.16b) and integrate to obtain

$$\left(\frac{n}{n_\ell}\right)^{4/3} - 1 = \frac{2}{3}\delta t. \tag{4.22}$$

This coarsening law is compared against simulations of equation (4.4) for the completely connected network in figure 4.7. By including the dimension d in the time scale, the simulations collapse using n_ℓ/n even though the number of connections per drop increases with n.

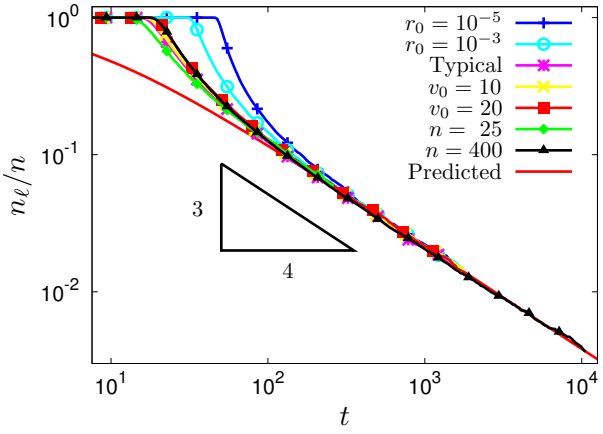

Figure 4.7: Coarsening of complete network according to equation (4.22). Simulations for $n = 100$, $r_0 = 0.1$, and $v_0 = 5$ (typical), unless noted in legend. Each simulation curve is an average of 100 simulations each with random initial condition. Simulations are cut off before they reached steady state for presentation purposes.

For square networks ($d = 2$) where a is not negligible, we insert Eqs. (4.18), (4.19), (4.20) as well as the relation $w^2 \approx n/n_\ell \approx v_\ell$ into equation (4.15b) and integrate to obtain

$$\left[\left(\frac{n}{n_\ell}\right)^{4/3} - 1\right]\left[\frac{3}{4} + 2\ln(2a)\right] - \left(\frac{n}{n_\ell}\right)^{4/3}\ln(\frac{n}{n_\ell})$$
$$= \frac{4\ln(a)}{3}t\delta, \tag{4.23}$$

where the value of a, mentioned previously, is given by $\ln(a) = -1.7$.

The derived coarsening law for the square network (4.23) matches the simulations of equation (4.4) as can be seen in figure 4.8. The difference between the $-3/4$ coarsening law, which would be obtained in the limit of $a \to 0$, and the coarsening law including logarithmic terms due to finite a [equation (4.23)] can also be seen in figure 4.8.

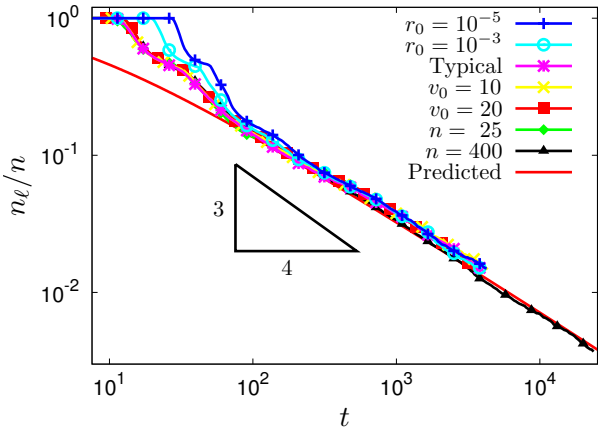

Figure 4.8: Coarsening of square network ($d = 2$) according to equation (4.23). Simulations for $n = 100$, $r_0 = 0.1$, and $v_0 = 5$ (typical), unless noted in legend. The predicted coarsening rate does not have a $-3/4$ exponent due to the non-zero value of a.

4.3.4 Fractal network: prediction and simulation

In the fractal network the $n/2$ pairs of drops closest to each other will coarsen first because the resistance between them is the lowest. In the next stage of the process (denoted $s_i = 2$) the $n/4$ pairs of drops next closest to each other coarsen, and this process continues until only one drop is left. We neglect the pressure of the small drops, since the flow between the larger drops does not pass below

these. The total resistance between drops depends only on the length between the remaining large drops, which goes as $\sum_{j=1}^{s_i} l_j = (2^{s_i})^{\lambda}$, where $\lambda \equiv 1/d_f$ and the stage s_i is given by $s_i = log_2(n/n_\ell)$. The growth rate of a large drop goes as

$$\dot{v}_\ell = \frac{p^* - p_\ell}{\sum_{i=1}^{s_n} l_i} = \frac{p^* - p_\ell}{v_\ell^{\lambda}}. \tag{4.24}$$

Inserting the approximation for the pressure (4.19), the mean-field pressure (4.20), and the conservation of volume (4.18), and then integrating gives the coarsening law

$$\left(\frac{n}{n_\ell}\right)^{4/3+1/d_f} - 1 = (4/3 + 1/d_f)\delta t. \tag{4.25}$$

Comparison of equation (4.25) against simulations of fractal systems equation (4.10) is shown in figure 4.9. The pre-exponential factor in the coarsening law was chosen as $\delta = 1/4$, and this fit matched the numerical simulations for $d_f = 1/2$, 1, 2, and 70; however, for small dimensional systems a range of fitting factors could have been justified. As seen in equation(4.25), *systems can be created with any coarsening exponent between* $-3/4$ *and* 0 *by changing the fractal dimension of the network.* In figure 4.9 the simulations show a 'staircasing' behavior due to the coarsening stages. Each step in the staircase halves the number of large drops. Staircasing is more prominent at smaller dimensions where the resistance, and therefore also the time, between the s_i and s_{i+1} stages is larger. For $d_f = 1$ the system coarsens at the same rate as that for the linear networks. For $d_f = 2$ the drops coarsen as $n_\ell \sim t^{-6/11}$ in contrast to the square coarsening rate of $n_\ell \sim t^{-3/4}$ plus logarithmic terms. This was verified by numerical simulations and is shown in figure 4.9. The coarsening rate $n_\ell \sim t^{-6/11}$ would be obtained in the square network only if the resistance between large drops would be proportional to w instead of $\ln(w)$. The coarsening for orthogonal networks is quicker than that for fractal networks for $1 < d_f < \infty$. In orthogonal

networks the resistance between large drops is lower due to the multiple flow paths in parallel, whereas the resistances add in series for the fractal networks. In the limit $\omega \to 1$ the infinite dimensional fractal network becomes identical to the completely connected network to within a constant scaling factor of time; simulations and predictions confirm this limiting behavior.

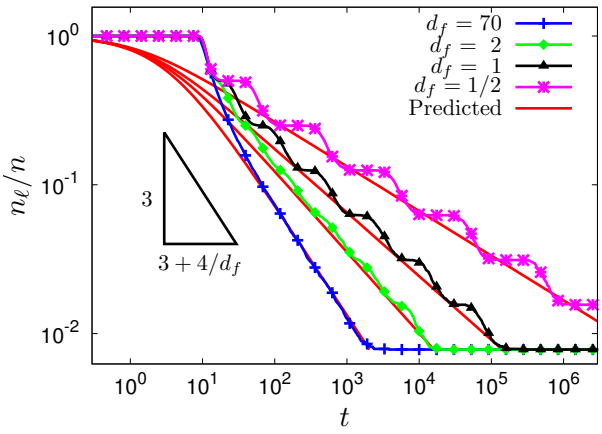

Figure 4.9: Coarsening of fractal network (various d_f). Simulations for $n = 128$, $v_0 = 5$, and $r_0 = 0.1$. Simulations are averaged over 100 random initial conditions. Predictions according to equation (4.25).

4.4 Distribution of large drop volumes and self-similar coarsening rates

To determine the difference between the large drop volumes throughout the coarsening we seek a self-similar distribution of the large drop volumes. From the distribution some of the heuristic coarsening laws from the previous section can be recovered. We follow the formulation presented by Gratton and Witelski [42] to apply the Lifshitz-Slyozov-Wagner (LSW) [63, 102] model to our system

of drops. It is assumed that the system has coarsened for long enough so that the initial perturbation has evolved into a self-similar distribution of volumes, but not so long that the number of large drops is too few to justify a continuous distribution. We write a conservation of law of the number density of large drops ϕ as

$$\frac{\partial \phi}{\partial t} + \frac{\partial}{\partial v}\left(\phi \dot{v}\right) = 0 \tag{4.26}$$

where $\dot{v}$ is given by equation (4.16a), (4.16b), or (4.24) for linear networks, orthogonal networks where $d \geq 2$ and $a \to 0$, or fractal networks, respectively. We can integrate the number distribution to obtain the number of large drops, the average large drop volume or the average large drop pressure

$$n_\ell = \int_0^\infty \phi dv, \tag{4.27}$$

$$\overline{v} = \frac{1}{n_\ell}\int_0^\infty v\phi dv, \tag{4.28}$$

$$\overline{p} = \frac{1}{n_\ell}\int_0^\infty v^{-1/3}\phi dv. \tag{4.29}$$

We construct a similarity variable $z \equiv v/v^*$ where v^* is a mean-field volume and seek a self-similar solution of the form

$$\phi = t^{-\alpha} f(z). \tag{4.30}$$

We assume the mean-field volume scales as $v^* = \nu t^\beta$ and the relation between the mean-field volume and average volume is given by $\gamma = v^*/\overline{v}$. The value of the pressure is given by equation (4.19), thus the mean-field pressure is $p^* = (v^*)^{-1/3}$, where α, β, γ, and ν are undetermined coefficients. In the equations for $\dot{v}$ we use the mean volume to determine the distance to the nearest large drops, as a result the function f will be independent of the network. Using the conservation of volume in large drops $n = \int_0^\infty v\phi dv$ we find the relation

$\alpha = 2\beta$. From equation (4.26) we find the value of α and an ordinary differential equation for the function f

$$\frac{df}{d\tilde{z}} = \frac{2\tilde{z}^{4/3} - 1}{-\tilde{z}^{7/3} + 4\tilde{z}^{4/3} - 3\tilde{z}} f \tag{4.31}$$

where $\tilde{z} \equiv z/z_{max}$. The undetermined coefficients β and z_{max} are found by setting the denominator of equation (4.31) and its derivative to zero, see [42, 9, 63] for details. The value of γ can be found from its definition. The values $z_{max}^{1/3} = 4/3$ and $\gamma = \int_0^1 f d\tilde{z}/(z_{max}\int_0^1 \tilde{z} f d\tilde{z}) \approx 0.8509$ were found. We integrate equation (4.31) numerically and compare this to the distributions of large drops for various networks from simulations of equation (4.4) in figure 4.10.

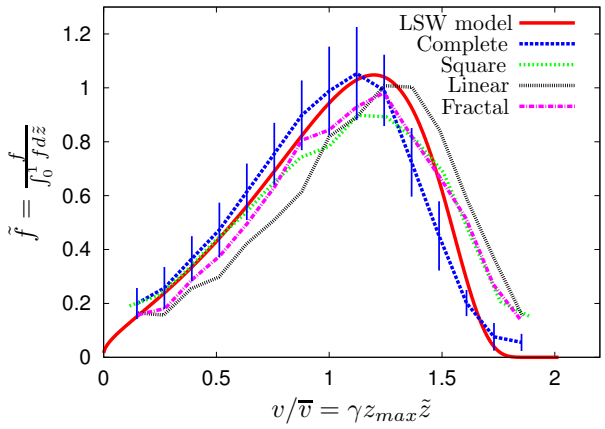

Figure 4.10: Probability distribution of large drop volumes. Simulations of complete, square and linear networks done with 2500 drops, Fractal network ($d_f = 2$) with 2048 drops. Only data between $500 > n_\ell > 200$ is used. All simulations had an initial volume of $v_0 = 5$ and a perturbation size of $r_0 = 0.1$. One standard deviation for the completely connected network is shown; error for other networks is of similar magnitude.

The probability distributions for the smaller dimensional networks are shifted to higher probabilities of larger volume drops, according to figure 4.10. The complete network most accurately matches the predicted probability distribution. Fractal networks of $d_f < 1$ do not reach a self-similar volume distribu-

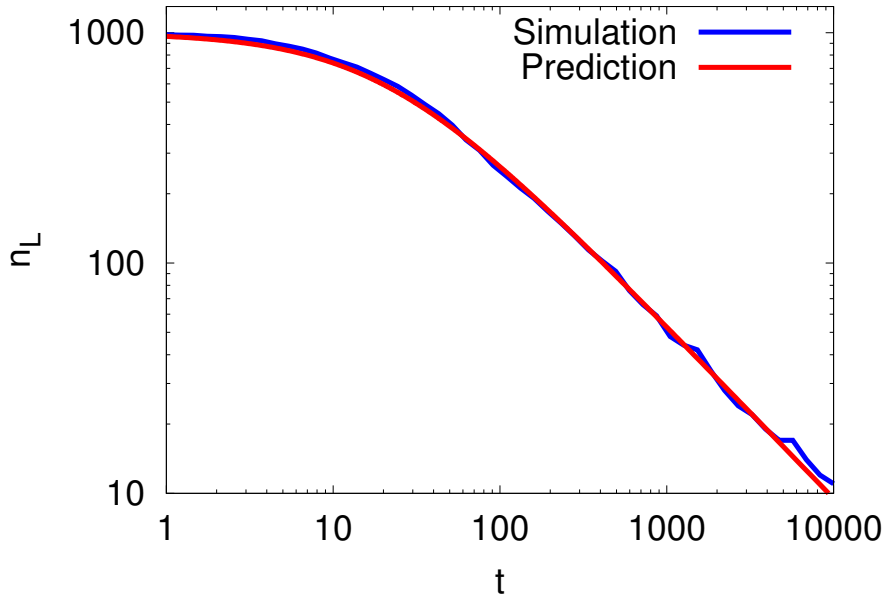

Figure 4.11: A complete network with $n = 1000$ and a random initial condition chosen such that it matches the self-similar distribution.

tion. These low-dimensional systems have very prominent stepping behavior, as seen in figure 4.9, and therefore the exact time at which the probability distribution is evaluated (on the flat or on the steep part of the step) can yield very different results. It was observed that, when the numerical simulations are given initial conditions that match the self-similar large volume distribution, they follow the heuristic coarsening laws even at early times (cf. figure 4.11). The self-similar distributions are apparently stable distributions.

The coarsening law can be found from equation (4.27) for regular networks where $a \to 0$ and fractal networks, using the values of γ and α found previously. The results are shown in Table 4.1. The coarsening exponents and the dependence on the total number of drops and initial volumes compare favorably to those found by heuristics. For $d = 2$ and $a > 0$, the coarsening law is a transcendental function of t and therefore cannot be expected from a similarity solution

Network	Dimension	Heuristics	Simulation δ	LSW
Linear ON	$d = 1$	$\left(\frac{n}{n_\ell}\right)^{7/3} - 1 = \frac{7}{3}\delta t$	0.15	$\left(\frac{n}{n_\ell}\right)^{7/3} = \frac{7}{3}\frac{3^3}{4^4}t$
Square ON	$d = 2$	$\left[\left(\frac{n}{n_\ell}\right)^{4/3} - 1\right]\left[\frac{3}{4} + 2\ln(2a)\right] - \left(\frac{n}{n_\ell}\right)^{4/3}\ln(\frac{n}{n_\ell}) = \frac{4\ln(a)}{3}t\delta$	0.20	NA
ON $a \to 0$	$d \geq 2$	$\left(\frac{n}{n_\ell}\right)^{4/3} - 1 = \frac{2}{3}\delta t$	NA	$\left(\frac{n}{n_\ell}\right)^{4/3} = \frac{2}{3}\frac{3^3}{4^4}t$
Complete ON	$d = n - 1$	$\left(\frac{n}{n_\ell}\right)^{4/3} - 1 = \frac{2}{3}\delta t$	0.25	$\left(\frac{n}{n_\ell}\right)^{4/3} = \frac{2}{3}\frac{3^3}{4^4}t$
Porous Media	Same as above			
Fractal	$0 < d_f < \infty$	$\left(\frac{n}{n_\ell}\right)^{\frac{4}{3}+\frac{1}{d_f}} - 1 = (\frac{4}{3} + \frac{1}{d_f})\delta t$	0.25	$\left(\frac{n}{n_\ell}\right)^{\frac{4}{3}+\frac{1}{d_f}} = (\frac{4}{3} + \frac{1}{d_f})\frac{3^3}{4^4}t$

Table 4.1: Comparison of heuristic and LSW coarsening rates as well as δ values used to fit the data for orthogonal networks (ON), porous media, and fractal networks. LSW predicts a pre-exponential factor of $\delta = 3^3/4^4 \approx 0.105$ for all networks.

of the form equation (4.30). The LSW theory also predicts a pre-exponential factor to be compared to a fit value of the heuristics. The probability distribution of large drops predicted by the LSW model is independent of network topology; therefore, the pre-exponential factor predicted is also independent of network topology. The LSW model predicts $\delta = 3^3/4^4 \approx 0.105$, which is most accurate for low dimensional systems.

4.5 Discussion and Summary

Simulations of coarsening behavior of a system of spherical-cap drops obtained by solving the 'exact' equations are reported. Drops are connected by conduits laid out in orthogonal (ON) and fractal networks (FN) with network size n, initial conditions, and system dimensions (d and d_f) varied in the simulations. Scaling-law predictions are derived by presuming dominant balances (heuristics) for coarsening growth and by assuming the LSW model for size-distribution dynamics. Table 4.1 summarizes the predictions. Figures 4.6, 4.7, 4.8 and 4.9 compare simulation of coarsening rates against prediction. Figure 4.10 compares simulation of distribution of size against prediction of the LSW model.

For coarsening rates, the prediction captures the dependence on initial total volume, initial drop size distribution, and network size with a single fitting parameter for each network type (Table 4.1). The initial volume dependence is accounted for by the time scale, and enters only through the perturbation size of the initial condition. The initial drop distribution is 'washed away' as the large drop distribution converges to the self-similar distribution shown in figure 4.10.

Connectivity	Time scale (T)	Constant (c)
ON	$c\mu L V_0^{4/3}/\sigma R^4$	$6^{1/3}/(d\pi^{4/3})$
PM $d \neq 2$	$c\mu L V_0^{4/3}/B^2\kappa\sigma$	$\frac{3^{1/3}(1-a^{2-d})}{2^{5/3}\pi^{4/3}(2-d)\int_{\Omega(r=1)} ds}$
PM $d = 2$	$c\mu L V_0^{4/3}/B^2\kappa\sigma$	$\frac{-3^{1/3}\ln(a)}{2^{5/3}\pi^{4/3}\int_{\Omega(r=1)} ds}$
FN	$c\mu L_1 V_0^{4/3}/\sigma R^4$	$2 \times 6^{1/3}/\pi^{4/3}$

Table 4.2: Time scales for orthogonal networks (ON), porous media (PM) and fractal networks (FN).

The network size enters the coarsening rate only as a ratio through the volume balance $v_\ell \approx n/n_\ell$. Coarsening depends most strongly on the dimension of the network. The coarsening exponent increases from $3/7$ to $3/4$ going from $d = 1$ (linear ON) to $d = 2$ (square ON, $a \to 0$) dimensions, as anticipated [34]. For $d > 2$ the exponent remains at $3/4$ while coarsening continues to increase but in a linear fashion, as reflected in the time-constant dependence on d (Table 4.2). The complete ON are optimally connected and show a maximum coarsening rate for any chosen n, among all the ON networks. Effects of the cut-off distance a at which the pressure of the drop is applied plays the strongest role in planar networks $d = 2$ where logarithmic corrections to the power law growth must be included to capture the simulations (figure 4.8).

The fractal network (FN) is distinguished by drops with exactly one nearest neighbor (a pairwise competition occurs between drops at each stage) but a resistance from stage to stage that changes in a self-similar fashion. Putting $d_f = 1$ corresponds to resistances that increase in a geometric fashion and yields a coarsening rate that is identical to the linear ON. Increasing to $d_f = \infty$, the FN coarsens with the same power law as the complete ON but with a different constant in the time scale. For all other d_f, the FN coarsens slower than the ON because the resistance of many conduits in series is greater than that for

conduits in parallel.

Drops coupled by a two dimensional porous medium coarsen with the same exponential behavior as those coupled by complete networks, cf. Table 4.1. Hence, a measured exponent alone cannot distinguish if the flow is through the reservoir, frit or a defect region; that is, cannot distinguish between cases (i) and (ii) above. For linear arrays of drops the coarsening exponent changes significantly from linear to complete coupling. In two dimensional arrays different flow types might be distinguishable by the coarsening time, provided the time scales differ significantly.

In some instances the practitioner may find it convenient to know the actual times the system might take to reach certain milestones, such as half-coarsening ($n_L = n/2$) or full-coarsening ($n_L = 1$). Expressions for these times can be readily derived from Tables 4.1 and 4.2. Due to the appearance of d in the time scale for orthogonal networks, changing the number of drops will change the time scale for the complete network, but not for other networks. That is, with R, V_0, L, and fluid properties held constant, the time for half-coarsening is independent of n for square networks; however, it scales as $1/n$ for complete networks. The time for full-coarsening scales as $n^{4/3}$ for square networks, and $n^{1/3}$ for complete networks. In practice, these times can be highly dependent on the initial distribution of imperfections, perhaps making the coarsening exponent a more reliable metric.

For drop size predictions by the LSW model, the pre-exponential factor is found to be independent of the network connectivity. In contrast, the simulations show that the lower dimensional networks have distributions shifted to larger volumes and smaller pre-exponential factors. The differences in large vol-

ume distributions cannot be attributed to different initial conditions (cf. [11]), as all initial conditions are picked from the same distribution. The reason the predicted distributions are insensitive to network type is because the mean volume is used to determine the distance to nearest large drops (w). The results suggest that the LSW model could be improved by incorporating the effects of network connectivity through the use of a better estimate of the large drop separation.

CHAPTER 5

BRIDGE-DROP CHANGE-OF-STATE*

5.1 Introduction

Consider a drop pinned on a flat circular support of radius R_0. Upon contact with a dry solid, the drop will spontaneously spread, turning into a liquid bridge (figure 5.1). The flow is driven by surface tension. For a viscous partially wetting fluid, the contact-line and bridge shape will move until equilibrium is reached. For this spreading flow, the dissipation occurs predominantly near the moving contact-line. Furthermore, for this spreading flow, the dissipation is equal to the rate of surface-energy loss, which allows one to measure the area-change in an experiment (provided surface tension is sensibly constant) and fit the corresponding dissipation by computation. Microscopic features of the moving contact-line, that have otherwise proved difficult to obtain directly, can thereby be inferred. The goal of this paper is to demonstrate the utility of this approach.

Every experimental set-up has an inherent limit of resolution. Contact-line experiments are often limited by optical resolution, typically $\sim 15\mu m$ [31, 81]. That is, the interface shape can be measured only up to a certain distance of the substrate, say $h_d - h_m$ (figure 5.1). The 'macroscopic' quantities are those measured below the height h_d, quantities such as the dynamic contact-angle θ_d and contact-line velocity U_d. The limit of resolution of a particular optical set-up, then, sets the definition of what is macroscopic. The 'microscopic' region, be-

*H.B. van Lengerich and P.H. Steen, Viscous dissipation and the contact-line region of spreading bridges. In Preparation

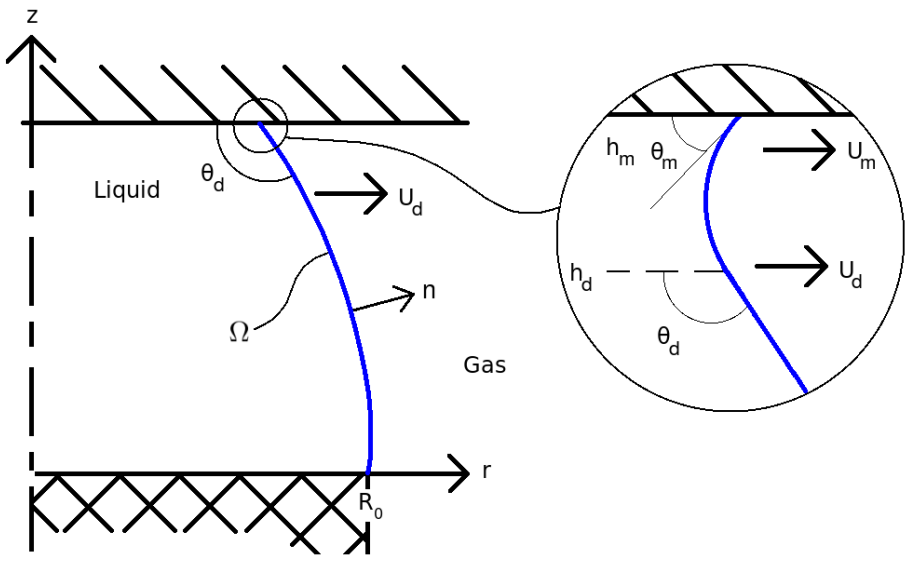

Figure 5.1: Macroscopic view (left) of a liquid bridge, pinned along a circle at the bottom, spreading along a substrate at the top. Microscopic view (right) of the moving contact-line region, illustrating the macroscopic and microscopic contact-angles (θ_d and θ_m) and speeds (U_d and U_m).

tween h_d and the substrate h_m, is the region close to the contact-line, not directly observable. Microscopic features, such as the contact-angle θ_m and contact-line velocity U_m, may take values different from their macroscopic counterparts and are therefore given different labels.

In this study macroscopic experimental data from high-speed video imaging is combined with numerical simulation to resolve the microscopic region of the contact-line. In a sense, the high-resolution flow computation substitutes for a higher-resolution optical system. However, we are not proposing that computations can replace direct observation, but that, subject to the hypotheses of the computational model (e.g. no substrate roughness, no shear-thinning), valuable microscopic information can be inferred. This microscopic information is important in explaining the macroscopic relation between the dynamic contact

angle θ_d and the contact-line velocity U_d. [There is a long history of such inference in science. Perhaps the best known example is the accurate estimate of Avogadro's number, based on macroscopic observations of Brownian motion [80] enabled by an estimate of Brownian diffusivity [32]].

Historically, models of contact-line motion have taken one of two approaches. The 'molecular-kinetic' models view the movement of the contact-line as a molecular rate process, with an energy barrier to moving forwards and another to moving backwards [6, 4]. According to this view, the microscopic contact-angle is equal to the dynamic contact-angle $\theta_m = \theta_d$ and the contact-line is driven by molecular forces. The 'hydrodynamic' models view contact motion in terms of continuum mechanics and a slip must be introduced close to the contact-line in order to resolve the non-integrable shear stress [52, 29]. More recent models have combined these two approaches by using non-equilibrium thermodynamics [87] or using molecular dynamics simulations close to the contact-line and matching these with hydrodynamic simulations [44]. This study will use the hydrodynamic approach.

Early hydrodynamic models, such as that by Huh [52], used wedge flow to solve for a self-similar flow regime near the contact-line. It was found that the no-slip boundary condition will always lead to infinite shear stresses at the contact-line [29]. This singular stress was eliminated by allowing slip close to the contact-line [51]. To drive the flow from the bulk to the contact-line, the free interface is expected to bend microscopically; the Young-Laplace pressure causes a low pressure region close to the contact-line (figure 5.1, inset). This 'viscous bending' has been demonstrated through simulations [65] and has been observed experimentally [31, 81]. Viscous bending prompted theoretical models

which have macroscopic and microscopic regions [98, 49, 20]. These models use matched inner and outer wedge flows to obtain an equation of the type

$$Ca \ln(L_{out}/L_{in}) = g(\theta_m) - g(\theta_d) \tag{5.1}$$

where $g(\theta) \equiv \int_0^\theta (\alpha - \cos(\alpha)\sin(\alpha))/(2\sin(\alpha))d\alpha$ [20]. Here L_{out} is the outer (or macroscopic) length scale, L_{in} is a length scale over which there is some kind of slip or breakdown of continuum mechanics. The capillary number is defined as $Ca \equiv \mu U_d/\gamma$ where μ is the viscosity and γ is the liquid-gas surface tension. Opinions on how to choose L_{out} vary greatly. Blake [4] states that it is "the approximate distance from the wetting line at which the contact-angle can be measured" and Rame et. al. [82] use the capillary length $\sqrt{\gamma/\rho g}$, as this is smaller than any other length scale in the experiment. In equation 5.1, the slip-length and microscopic contact-angle cannot be known simultaneously. For simplicity, it is frequently assumed that θ_m is a constant, and therefore must be equal to the equilibrium contact angle θ_e [82].

In this work, we record the macroscopic shape and velocity of a bridge spreading on a solid. From these experiments a relation between Ca and θ_d is obtained. The flow field and microscopic bending are computed from the macroscopic experimental bridge shapes using the boundary integral method (BIM). Numerically solving the hydrodynamic equations on the entire domain eliminates the need to specify the outer length scale L_{out}, and replaces the asymptotic solution (equation 5.1). A slip condition must be specified on the solid-liquid interface where the contact-line moves. Two types of slip are used: i) a region of local slip (LS) close to the contact-line where the shear stress is set to zero; and ii) a Navier slip (NS) condition where the slip is proportional to the shear stress. As is the case for equation 5.1, the formulation is purely hydrodynamic so far; therefore the relation between slip-length and microscopic

contact-angle is unknown. These are related to the equilibrium contact-angle by using an energy balance.

An overview and test of the method in the absence of contact-line motion are given in section 5.2. The formulation of the hydrodynamic problem is given in section 5.3. In section 5.4, different formulas for the energy lost are derived. The material in sections 5.3 and 5.4 has appeared in the literature in different places with varying notation. The accepting reader could skip these sections; key equations are summarized in table 5.1. In section 5.5 an experiment is used to demonstrate the significance of the various contributions to the energy in spreading along both hydrophobic and hydrophilic solid substrates. The BIM Stokes-flow code used to compute the flow field within the bridge is described in section 5.6. In section 5.7 the slip-length, flow profile and the location of dissipation within the bridge are found numerically using the energy balance. In section 5.8 the energy balance is used to analytically determine the microscopic contact-angle for the different types of slip. This result is independent of the results in sections 5.5-5.7. It is compared against the microscopic angle, computed numerically. Finally, in section 5.9, the microscopic contact-angle result and the computed slip-lengths are used to interpret the parameters in the Voinov-Hocking-Cox model.

5.2 Overview: Spreading bridges and drop-bridge changes-of-state

The spreading bridge (figure 5.1) is closely related to coalescing drops, and a retracting bridge is closely related to a breaking bridge. The coalescing and

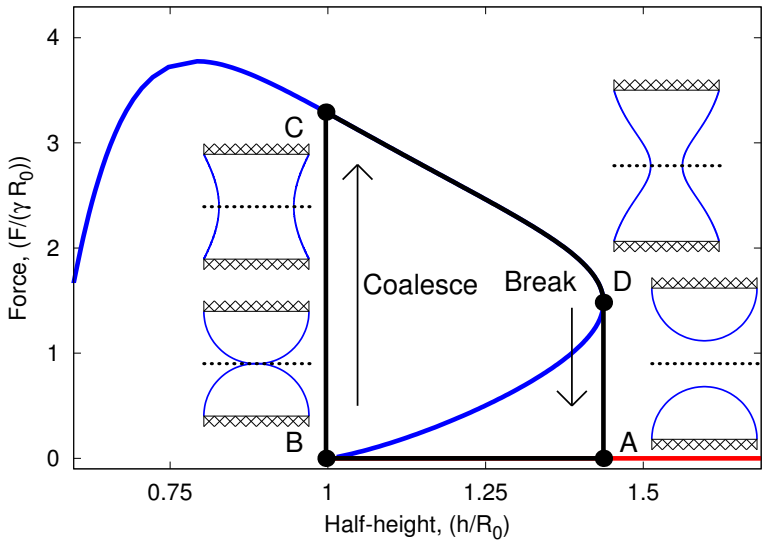

Figure 5.2: Bridge-drop force-length thermodynamic cycle for a constant half-volume $V = 2\pi R_0^3/3$. Solid lines are equilibrium states generated using branch-tracing code [27]. Arrows indicate non-equilibrium transitions at limits of stability. The shapes are for pinned-pinned contact-lines and spreading on a solid with 90° equilibrium contact-angle (indicated by dotted line).

breaking events may be viewed as changes-of-state, as summarized in the drop-bridge cycle of figure 5.2. State A in figure 5.2 shows two drops, pinned at circular contacts, that are mirror images of one another and have axes-of-rotation that align. As the two drops are brought together, they will eventually touch and a liquid bridge will evolve. The axisymmetric evolving shapes are mirror symmetric about the mid-plane (dotted), so that the equilibrium curves in figure 5.2 also apply to bridges wetting a surface with a 90° contact-angle. The dynamics of the change-of-state for coalescence/breaking differs from spreading/retracting due to the resistance provided by the solid boundary. In the limit of a 'no-shear' solid boundary the dynamics become identical.

Bridge spreading and the bridge breaking are important for a switchable

capillary adhesion device that has recently been designed and built [97]. This device utilizes the pulling force of many liquid bridges to adhere to a substrate. By removing volume from the bridges, release from the substrate may be controlled. Under an excess of applied force, release may be uncontrolled. In this case bridge lengths are increased (e.g. from C to D) until instability initiates breaking (D to A). Analysis of the kind demonstrated in this paper allows predictions of force-distribution during grabbing (bridge spreading) and breaking events as they vary with time. These results are peripheral to our purpose and will not be presented here.

5.2.1 Rate of energy decay

Consider the work done in the constant-volume cycle of drop coalescence and bridge breaking shown in figure 5.2. No work is done as the drops are brought closer together quasi-statically (A to B). When the drops touch, a spontaneous change-of-state (B to C) forms a liquid bridge, driven by decreasing surface energy (surface area times the surface tension). The liquid bridge exerts a pulling force. The work done to stretch the bridge quasi-statically (C to D) is equal to the increase in surface energy. The bridge becomes unstable at the turning point in the force-length diagram [14, 66] and decreases surface energy by undergoing a change-of-state (D to A) to form two drops. The work done on the system to perform a cycle is given by the area ABCD. This energy becomes surface energy, and this potential energy is dissipated during the two changes-of-state. The concept discussed for the drop-bridge cycle remains the same for the cycle of spreading/retracting on a solid surface, although the flow profile and, therefore, the distribution of the dissipation differs.

Now consider a general change-of-state, that is either a bridge spreading on a solid or a pinned-pinned coalescing event. By keeping the length fixed, no work is done on the system. In the absence of body forces and elastic forces within the liquid, the change in potential energy between two configurations with negligible kinetic energy is given by the change in surface energy. Up to a constant, the surface energy of a quasi-static shape is given by

$$\mathcal{A} \equiv \gamma A_{lg} + \gamma_{ls} A_{ls} + \gamma_{sg} A_{sg} \tag{5.2}$$

where A_{lg} is the liquid-gas area and the subscripts ls and sg represent the liquid-solid and solid-gas interfaces, respectively. Here the surface tensions are assumed to be constants. This equation is valid for both moving contact-line and pinned-pinned configurations, in which case A_{ls} and A_{sg} are constant. In the case of low Reynolds number, the change in kinetic energy is small compared to the change in surface energy, and equation 5.2 is valid throughout the change-of-state. This study focuses on incompressible Newtonian fluids at low Reynolds number. In table 5.1 the rate-of-change of the surface energy is split into free and solid interface components. At the solid interface, the Young-Dupré equation [107] has been used to eliminate the liquid-solid and gas-solid surface tensions in favor of the equilibrium contact-angle θ_e.

The rate of work done by the interface on the inner fluid, or "power" $\mathcal{P}$ (see [92]), is summarized in row 2 of table 5.1. The power exerted has a contribution from the free interface due to viscous bending. The free interface pushes with pressure p against a fluid with velocity v. Along the solid interface the non-equilibrium Young-Dupré force pushes against the fluid at the contact-line velocity U_d. The equivalence between the loss of surface energy and power is proved in section 5.4.2 and tested against experiment in section 5.5.

rate of energy loss		=	free interface	+	solid interfaces
Surface (5.19)	$\dot{\mathcal{A}}$	=	$\gamma \frac{d}{dt} \int_{\Omega_d} dA$	−	$\gamma \oint_{\ell_d} U_d \cos\theta_e d\ell$
Power (5.22)	$\mathcal{P}$	=	$2\pi\gamma \int_0^{h_d} \left(\frac{1}{r_1} + \frac{1}{r_2}\right) \frac{dR}{dt} r dz$	+	$\gamma \oint_{\ell_d} (\cos\theta_d - \cos\theta_e) U_d d\ell$
Dissipation (5.24)	$-\mathcal{D}$	=	$-\int_\Omega \boldsymbol{\sigma} \cdot \boldsymbol{n} \cdot \boldsymbol{v} dA$	−	$\int_{ls} \boldsymbol{\sigma} \cdot \boldsymbol{n} \cdot \boldsymbol{v} dA$

Table 5.1: $\dot{\mathcal{A}} = \mathcal{P} = -\mathcal{D}$; equivalent expressions for the rate of energy loss in a system with a moving contact-line. Find derivations in section 5.4 (equation numbers in parenthesis).

In a viscous change-of-state, energy is dissipated by friction within the liquid (the surrounding gas dynamics are neglected). Other forms of energy loss, such as those involving the phase-change when liquid molecules adjacent to gas molecules become liquid molecules adjacent to a solid molecules, are assumed negligible. The viscous dissipation is given by

$$\mathcal{D} = \int_V \boldsymbol{\sigma} : \boldsymbol{\nabla} \boldsymbol{v} dV \tag{5.3}$$

which can be evaluated once the velocity $\boldsymbol{v}$ and the total stress tensor $\boldsymbol{\sigma}$ are known [60]. Here V is the instantaneous volume occupied by the liquid. Alternatively, the viscous dissipation can be computed from the work done on the fluid along the free and solid-liquid interfaces, listed in row 3 of table 5.1 (see section 5.4.3). The special feature of the flows that we consider is that the surface energy loss is balanced by the dissipation at every instant.

$$\dot{\mathcal{A}} = -\mathcal{D}. \tag{5.4}$$

We will derive this equation in section 5.4.3. In the case of pinned-pinned change-of-state this balance provides no new information. In contrast, when the change-of-state involves a moving contact-line, the added degree-of-freedom

introduces microscopic parameters which are not directly measurable. Equation 5.4 then yields an extra relation from which the microscopic contact-angle and the slip-length can be obtained. The concept of coupling hydrodynamic equations to an energy balance is not new; it has been performed by Brochard-Wyart [10] and deGennes [24] for completely wetting fluids. Voinov has used this energy balance to gain insight into contact-line hysteresis [98], microscopic contact-angles [99] and wetting fluids [100].

5.2.2 Experiment and computation for pinned contact-lines

A pinned-pinned experiment provides a check of the equivalence of terms in table 5.1 and the proposed method. In the case of a pinned contact-lines, each row of table 5.1 simplifies. The solid interface terms (right column) all vanish since $U_d = 0$ by pinning and $v = 0$ by the no-slip condition. In this case, there is no degree-of-freedom amongst the expressions of table 5.1. The energy lost can be evaluated as the observed area-change (equation 5.2) or, alternatively, using the viscous dissipation (equation 5.3) through a computational solution of the Stokes equations. Provided the viscosity has been measured separately, these two alternative routes to the energy-loss are independent.

A coalescence experiment on a PDMS bridge (viscosity $\mu = 5.7kg/ms$, measured) with both contact-lines pinned is performed. The free surface shape and velocity are recorded using a high-speed camera and a BIM simulation (section 5.6) is used to calculate the flow within the bridge for each image frame. The interfacial rate of energy loss, the power, and the viscous dissipation (left column of table 5.1) are shown in figure 5.3. The difference between $\mathcal{A}$, $\bar{\mathcal{P}} \equiv \int_0^t \mathcal{P} dt$ and

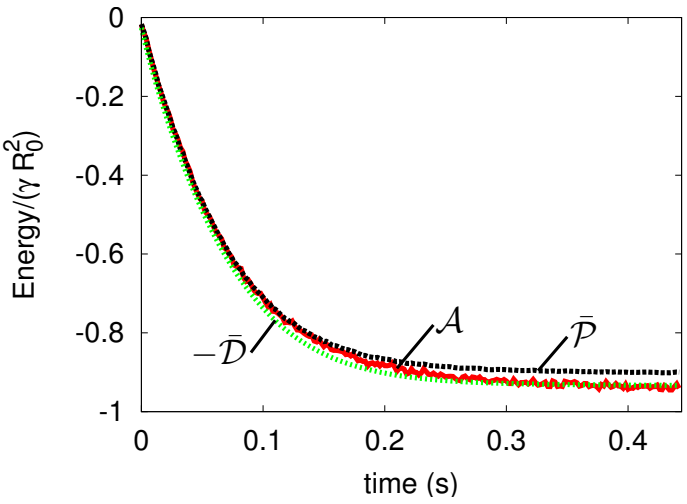

Figure 5.3: Energy loss for pinned-pinned coalescence: Measured surface energy $\mathcal{A}$ (equation 5.19), measured work done by interface $\bar{\mathcal{P}} \equiv \int_0^t \mathcal{P} dt$ (equation 5.22) and accumulated viscous dissipation $-\bar{\mathcal{D}} \equiv -\int_0^t \mathcal{D} dt$ calculated by the BIM according to equation 5.24 (no fitting). Volume is $V/R_0^3 = 2.88$. The first $0.03s$ have been omitted.

$-\bar{\mathcal{D}} \equiv -\int_0^t \mathcal{D} dt$ is at most 5%.

For the moving contact-line, in contrast to the pinned-pinned case, the boundary terms in the second column of table 5.1 can be significant. The computation of the dissipation depends strongly on the slip-length, an unknown parameter, which is then fit to the rate of surface energy loss obtained from experiment via equation 5.4. It may seem surprising that a macroscopic experiment can extract microscopic slip-lengths. This is possible because of the singular dependence of dissipation on slip-length.

5.3 Formulation

An axisymmetric liquid bridge, pinned by a circle at the bottom, spreads along a substrate at the top boundary, figure 5.1. The governing equations for the incompressible viscous fluid within the bridge are Stokes equation and continuity

$$\boldsymbol{\nabla} \cdot \boldsymbol{\sigma} = \mathbf{0} \tag{5.5a}$$

$$\boldsymbol{\nabla} \cdot \boldsymbol{v} = 0 \tag{5.5b}$$

where $\boldsymbol{v} = [v_r, v_z]$ is the velocity and $\boldsymbol{\sigma}$ is the total stress tensor, defined as

$$\boldsymbol{\sigma} \equiv -p\boldsymbol{I} + \boldsymbol{\tau} \tag{5.6a}$$

$$\boldsymbol{\tau} \equiv \mu \left[\boldsymbol{\nabla v} + (\boldsymbol{\nabla v})^T \right] \tag{5.6b}$$

and p is the pressure.

Two boundary conditions must be specified at each interface in order to solve equations 5.5. At the top solid boundary ($z = h_m$), the liquid does not penetrate the solid

$$\boldsymbol{v} \cdot \boldsymbol{n} = 0, \tag{5.7}$$

where $\boldsymbol{n}$ is the normal pointing away from the liquid. Previous work shows that the contact-line motion should be insensitive to the exact type of slip introduced [20]. For this reason we introduce two different slip conditions:
i) local slip (LS) near the contact-line, specified as the location where the free interface $r = R(z,t)$ meets the solid,

$$\begin{aligned} \boldsymbol{v} \cdot \boldsymbol{t} = 0 \text{ for} \quad & r \leq R(h_m, t) - b \\ \boldsymbol{\sigma} \cdot \boldsymbol{n} \cdot \boldsymbol{t} = 0 \text{ for} \quad & R(h_m, t) - b < r < R(h_m, t), \end{aligned} \tag{5.8a}$$

and ii) the Navier slip (NS) condition [74],

$$-\frac{\beta}{\mu}\boldsymbol{\sigma}\cdot\boldsymbol{n}\cdot\boldsymbol{t}=\boldsymbol{v}\cdot\boldsymbol{t}. \tag{5.8b}$$

The unit vector $\boldsymbol{t}$ is tangent to the liquid boundary in a plane of constant azimuthal angle. For the local slip, the length b is the distance from the contact-line over which the no-shear boundary condition is applied; no slip applies elsewhere. For the Navier slip, the length β is the distance above the solid interface at which the no-slip boundary condition would apply. These two models are typical ways to resolve contact-line singularities [23, 30].

Along the free interface, $r = R(z,t)$, both the Young-Laplace and the kinematic condition are satisfied

$$\boldsymbol{\sigma}\cdot\boldsymbol{n}=-\gamma\left(\frac{1}{r_1}+\frac{1}{r_2}\right)\boldsymbol{n} \tag{5.9a}$$

$$\boldsymbol{v}\cdot\boldsymbol{n}=\frac{dR}{dt}\left(1+\frac{dR}{dz}^2\right)^{-1/2}, \tag{5.9b}$$

where r_1 and r_2 are the principle curvatures. Due to the absence of surface-tension gradients there is no shear along the free interface. Since equation 5.9a is a vector equation, three boundary conditions have been stated for each point along the free interface. However, the system is not overdefined since the shape of the free interface must also be solved for. According to the tangent-angle formulation,

$$\frac{dR}{dz}=\cot\theta \tag{5.10a}$$

$$\frac{d\theta}{dz}=\frac{-1}{\sin\theta}\left(\frac{1}{r_1}+\frac{1}{r_2}\right)-\frac{1}{R} \tag{5.10b}$$

where θ is the angle measured through the liquid to a plane parallel to the solid surface. The free interface must also satisfy the integral constraint for constant

volume,

$$V = \int_0^h \pi R^2 dz, \tag{5.11}$$

as well as the boundary value,

$$R(0,t) = R_0, \tag{5.12}$$

for the pinned bottom radius.

The bottom boundary conditions are no-slip and no-penetration on the circle at $z = 0$,

$$\boldsymbol{v} \cdot \boldsymbol{n} = 0 \tag{5.13a}$$

$$\boldsymbol{v} \cdot \boldsymbol{t} = 0. \tag{5.13b}$$

The assumed axisymmetry gives conditions at $r = 0$,

$$\boldsymbol{v} \cdot \boldsymbol{n} = 0 \tag{5.14a}$$

$$\boldsymbol{\sigma} \cdot \boldsymbol{n} \cdot \boldsymbol{t} = 0. \tag{5.14b}$$

For pinned-pinned bridges, instead of equation 5.8, the boundary condition 5.13b is applied at $z = h_m$. At the top $R(h_m, t) = R_0$, which adds an extra constraint to the free interface ODE 5.10. The evolution of a pinned-pinned bridge can be solved using the above hydrodynamic equations with a known initial condition. In contrast, for spreading bridges, the slip-length and a boundary condition at the top of the free interface $R(h_m, t)$ are not known. Note that, even though the equilibrium contact-angle θ_e is absent from this formulation, this is an important parameter in the dynamics. In this work, we shall use the overall energy balance to relate θ_e to the hydrodynamic equations and we will measure dR/dt from an experiment to obtain a slip-length.

5.4 Energy decay rate

The irreversible change-of-state is driven by the potential energy of the interfaces ($\mathcal{A}$). The rate of energy loss can be expressed in terms of the working ($\mathcal{P}$) of the interface on the fluid. Surface energy and the work done by the interface can be obtained from images of an experiment. The rate of surface energy loss is equal to the viscous dissipation $\mathcal{D}$ and to calculated $\mathcal{D}$ requires knowledge of the flow within the liquid bridge.

5.4.1 Surface energy relation

During a viscous change-of-state the mechanical work, kinetic energy, body forces and elastic forces are negligible. The surface energy (equation 5.2) determines the energy of the system. The rate of change in energy is given by

$$\dot{\mathcal{A}} = \gamma \dot{A}_{lg} + \gamma_{ls} \dot{A}_{ls} + \gamma_{sg} \dot{A}_{sg}. \tag{5.15}$$

The solid surface tensions (γ_{ls} and γ_{sg}) are eliminated in favor of the equilibrium angle using the Young-Dupré equation [107]

$$\gamma \cos\theta_e = \gamma_{sg} - \gamma_{ls}. \tag{5.16}$$

This equation does not assume that the dynamic contact-angle and the equilibrium contact-angle are similar. The changes in wetted solid area can be related to the contact-line velocity to give

$$\dot{\mathcal{A}} = \gamma \frac{d}{dt} \int_{\Omega} dA - \gamma \oint_{\ell_m} U_m \cos\theta_e d\ell \tag{5.17}$$

where $\Omega = \Omega_d + \Omega_m$ is the liquid-gas area from $z = 0$ to $z = h_m$ and ℓ_m is the circular contact-line located at $z = h_m$. Here Ω_d is the free interface from $z = 0$

to $z = h_d$ and Ω_m is the free interface from $z = h_d$ to $z = h_m$. In an experiment, the microscopic values are unknown. Under conditions where

$$\left|\frac{d}{dt}\int_{\Omega_d} dA\right| \gg \left|\frac{d}{dt}\int_{\Omega_m} dA\right| \text{ and} \tag{5.18a}$$

$$\left|\oint_{\ell_d} U_d d\ell\right| \gg \left|\oint_{\ell_d} U_d d\ell - \oint_{\ell_m} U_m d\ell\right| \tag{5.18b}$$

the energy can be expressed in terms of macroscopic values

$$\dot{\mathcal{A}} = \gamma\frac{d}{dt}\int_{\Omega_d} dA - \gamma\oint_{\ell_d} U_d \cos\theta_e d\ell \tag{5.19}$$

where ℓ_d is the circle of radius $R(h_d, t)$ located at height $z = h_d$. The scaled surface energy $\mathcal{A}/\gamma R_0^2$ depends only on one material property (θ_e) and can be determined from knowledge of the free interface alone.

5.4.2 Working of the interface

The rate of surface energy change can be alternatively expressed in terms of the power exerted by the interface on the fluid. At the observed contact-line the unbalanced Young-Dupré force moves the contact line at a velocity U_d. The Young-Laplace pressure moves the free interface along its normal.

A purely geometric result gives a relation between the change in area and the sum of the principle radii of curvature as well as a contribution from a line integral,

$$\frac{d}{dt}\int dA = \int\left(\frac{1}{r_1} + \frac{1}{r_2}\right)\boldsymbol{n}\cdot\boldsymbol{v}dA + \oint U\cos\theta d\ell, \tag{5.20}$$

where the line integral is performed at the moving boundary of the area. This equation is derived in appendix F. This equation can be applied over any fraction of the surface area of the bridge. Choosing the area to be the observed area

Ω_d, and inserting into the equation 5.19 gives

$$\dot{\mathcal{A}} = \gamma \int_{\Omega_d} \left(\frac{1}{r_1} + \frac{1}{r_2} \right) \boldsymbol{n} \cdot \boldsymbol{v} dA + \gamma \oint_{\ell_d} U_d (\cos\theta_d - \cos\theta_e) d\ell. \tag{5.21}$$

Due to the kinematic boundary condition (equation 5.9b), the change in area can be related to the deformation of the free interface. We now recognize the loss of surface energy as the power exerted by the interface;

$$\dot{\mathcal{A}} = 2\pi\gamma \int_0^{h_d} \left(\frac{1}{r_1} + \frac{1}{r_2} \right) \frac{dR}{dt} r dz + \gamma \oint_{\ell_d} U_d (\cos\theta_d - \cos\theta_e) d\ell \equiv \mathcal{P}. \tag{5.22}$$

Using this equation, the scaled loss of energy can be obtained directly from video of a spreading bridge and the equilibrium contact-angle. The accuracy of the experiment has yet to be specified; greater optical resolution decreases $h_m - h_d$ and brings the observed contact line ℓ_d closer to the actual contact line ℓ_m. As long as the inequalities 5.18 are satisfied, equation 5.22 is valid, regardless of the optical resolution. This equation can also be obtained from relations given by Dussan [28] and Joseph [53].

In 5.22, the term $\gamma \oint U_d (cos\theta_d - cos\theta_e) d\ell$ is the power exerted by the Young-Dupré force. This term is zero for pinned contact-lines because $U_d = 0$. The term $2\pi\gamma \int_{\Omega_d} \left(\frac{1}{r_1} + \frac{1}{r_2} \right) \boldsymbol{n} \cdot \boldsymbol{v} dA$ is the rate of work done along the liquid-gas surface. If the pressure were constant, then this term would be zero due to incompressibility. To see this, apply the divergence theorem to the volume integral of incompressibility $0 = \int \boldsymbol{\nabla} \cdot \boldsymbol{v} dV = \oint_\Omega \boldsymbol{v} \cdot \boldsymbol{n} dA = 2\pi \int \frac{dR}{dt} r dz$. In the absence of viscous bending, the pressure is constant, and the energy lost due to terms along the free interface is zero. It is appropriate to neglect the work done by the viscous bending *only* when the pressure across the free interface is constant (e.g. [24, 45, 10]).

5.4.3 Viscous dissipation

The viscous dissipation within the fluid can be related to the loss of surface energy. Consider the control volume encasing the interfaces in figure 5.4. In the limit of a control volume with zero volume the internal energy is determined by the surface energy alone [89]. The change in internal energy is balanced by the work done on the control volume. In the absence of significant temperature gradients, the change in energy of the dashed region is given by

$$\frac{d}{dt}\left[\gamma A_{lg} + \gamma_{ls} A_{ls} + \gamma_{sg} A_{sg}\right] = \int \boldsymbol{\sigma} \cdot \tilde{\boldsymbol{n}} \cdot \boldsymbol{v} dA \tag{5.23}$$

where $\tilde{\boldsymbol{n}}$ is the normal pointing out of the control volume and the area integral is done along the entire surface of the control volume. The left-hand-side of this equation is $\dot{\mathcal{A}}$. The work done within the solid surfaces and along the bottom liquid (where the no-slip boundary condition applies) are zero because the velocity is zero. For a gas of negligible viscosity the total stress in the gas is equal to a constant pressure. The work done along the gas surface is zero due to incompressibility of the liquid. The only remaining work terms are those within the liquid. The normals pointing out of the control volume within the liquid can be related to the normals pointing out of the liquid $\tilde{\boldsymbol{n}} = -\boldsymbol{n}$, defined previously. The loss of internal energy can be expressed in terms of the remaining non-zero area integrals, which we recognize as the viscous dissipation

$$\dot{\mathcal{A}} = \int_{\Omega} \boldsymbol{\sigma} \cdot (-\boldsymbol{n}) \cdot \boldsymbol{v} dA + \int_{ls} \boldsymbol{\sigma} \cdot (-\boldsymbol{n}) \cdot \boldsymbol{v} dA \equiv -\mathcal{D} \tag{5.24}$$

where ls represents the liquid-solid interface on the liquid side. The first term on the right represents viscous bending losses, as the integrand is the same as 5.21, due to the Young-Laplace equation (5.9a). For equation 5.24, the viscous bending term accounts for the bending in the microscopic region, whereas equa-

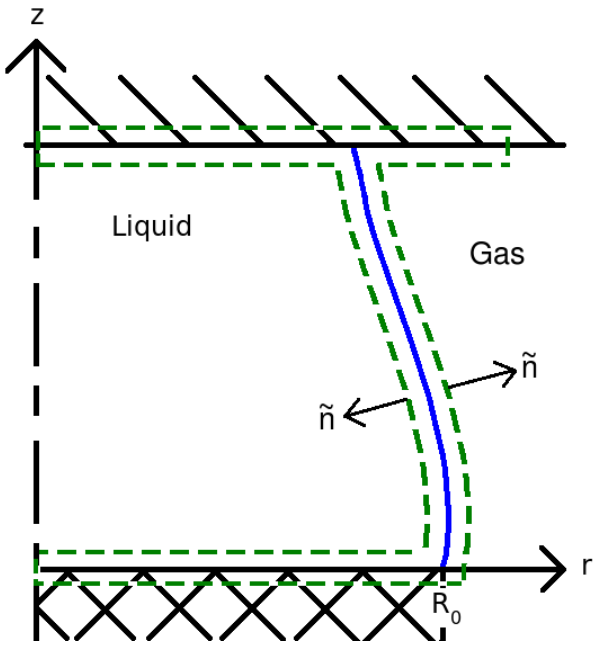

Figure 5.4: Work done on the boundary of the control volume is equal to the rate of surface energy lost within it.

tion 5.21 only accounts for the macroscopic bending. The second term on the right represents losses due to the sliding of the liquid along the solid surface.

The right-hand-side of equation 5.24 can be expressed in terms of a volume integral using the divergence theorem along with the Stokes flow (equations 5.5a):

$$\int_{\Omega} \boldsymbol{\sigma} \cdot \boldsymbol{n} \cdot \boldsymbol{v} dA + \int_{ls} \boldsymbol{\sigma} \cdot \boldsymbol{n} \cdot \boldsymbol{v} dA = \int_{V} \boldsymbol{\sigma} : \boldsymbol{\nabla} \boldsymbol{v} dV. \tag{5.25}$$

The viscous dissipation calculated by equation 5.24 agrees with the conventional interpretation of viscous dissipation given by equation 5.3 (cf. [60, 26]). This quantity is strictly positive and represents the irreversible energy lost due to friction within the liquid [26]. To evaluate $\mathcal{D}$, the viscosity, surface tension and the velocity and tractions along the free interface must be known. The computation of the viscous dissipation lends itself well to the boundary integral

method, where $\boldsymbol{\sigma} \cdot \boldsymbol{n}$ and $\boldsymbol{v}$ are found along the boundary of the liquid.

5.5 Experiments

Experiments are done with PDMS as the liquid and the end of a metal cylinder to pin the contact-line. For the top substrate, either another cylinder (for pinned-pinned experiments) or a coated glass plate (for spreading experiments) is used. The images are recorded with a high-speed camera and analyzed to find the surface energy ($\mathcal{A}$) and the working of the interface ($\mathcal{P}$).

For both pinned-pinned and spreading experiments, vinyl terminated PDMS, with molecular weight $45,000 - 55,000$ and 95% purity (Gelest) is used. From a pendant drop the surface tension was found to be $0.021 kg/s^2$ [35]. This agrees well with the value of $0.0208 kg/s^2$ [85]. The Newtonian viscosity was found to be $5.7 \pm 0.2 kg/(ms)$ (95% confidence) using a cone and plate rheometer, and within the range given by the manufacturer $3.9 - 5.8 kg/(ms)$.

Pinned-pinned experiments are done with two identical steel cylinders 1.3mm in diameter. A drop is placed between the cylinders and then a bridge is made and broken to get two similarly shaped drops. Spreading experiments are done with one of two coated glass slides. A hydrophobic substrate is created by reacting glass with (heptadecaflouro-1,1,2,2-tetra hydrodecyl) trichlorosilane for at least ten hours and a hydrophilic substrate is created with dodecyl trichlorosilane (see [16, 101] for more procedure details). The slides are cleaned with ethanol and water and dried with compressed air. The static advancing contact-angles are found to be $68.5 \pm 3.7^\circ$ and $14 \pm 5^\circ$ using a sessile drop. The spreading experiments are performed by placing a drop on the cylinder and then slowly

moving the cylinder until the drop makes contact with the cleaned substrate. No electrostatic effects were observed.

All experiments are recorded at 500 fps and $500\mu s$ exposure time with a Redlake MotionPro HS-3 camera and back lit with a 150 watt incandescent light. The resolution was $8\mu m$ per pixel using a Tamron SP AF Di $90mm$ macro lens. Slight inconsistencies in the light intensity caused the size of the image to oscillate. To reduce the noise in the velocity data, only every eighth frame was used for the spreading experiments.

From the video of the spreading experiment and the equilibrium contact-angles, the scaled loss of energy can be obtained using either equation 5.19 or 5.22. The energy for the pinned-pinned coalescence was shown in figure 5.3. The energies for coalescence on hydrophilic and hydrophobic substrates are shown in figure 5.5. The change in surface energy is obtained from images by equation 5.19, where $\Omega_d = 2\pi \int_0^{h_d} R\sqrt{1+(dR/dz)^2}dz$. The change in energy can also be obtained by integrating the power (equation 5.22), where $1/r_1 + 1/r_2 = -\frac{d^2R/dz^2}{(1+(dR/dz)^2)^{3/2}} + \frac{1}{R\sqrt{1+(dR/dz)^2}}$. These two expressions were shown to be equivalent in section 5.4. Calculating derivatives of the pixilated free interfaces leads to the small discrepancies observed in figure 5.3 and figure 5.5.

The free interface and solid-fluid interface contributions to the surface energy ($\mathcal{A}$) and integrated power ($\bar{\mathcal{P}}$) for the spreading bridges are shown in figure 5.5. The area of the free interface initially decreases as the solid-liquid area increases, both resulting in decreases of energy. At later times the solid-fluid energy decreases as the free interface energy increases - this happens to a greater extent for the hydrophilic substrate. In both hydrophobic and hydrophilic substrates the viscous bending dissipated roughly the same amount

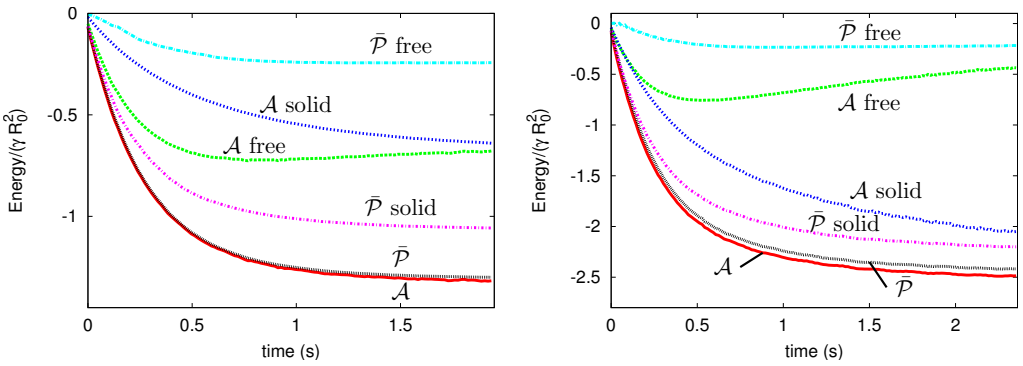

Figure 5.5: Measured contributions to surface energy, $\mathcal{A} = \mathcal{A}_{free} + \mathcal{A}_{solid}$ (equation 5.19), and to cumulative work done, $\bar{\mathcal{P}} = \bar{\mathcal{P}}_{free} + \bar{\mathcal{P}}_{solid}$ (equation 5.22). Spreading on a hydrophobic substrate, $\theta_e = 68.5 \pm 3.7°$ and $V/R_0^3 = 1.24$ (left) and on a hydrophilic substrate, $\theta_e = 14 \pm 5°$ and $V/R_0^3 = 1.70$ (right). No fitting.

of energy. However, this accounts for 9% of hydrophilic dissipation and 19% of hydrophobic dissipation due to the differing total dissipation for the two substrates.

Dimensionless parameters can be found using the bridge experiments and the liquid properties (assumed to be constant). The maximum Reynolds number in the pinned-pinned experiments is $Re \equiv \rho U_d R_0/\mu = 3 \times 10^{-4}$. For the spreading experiments the maximum Reynolds number is 1.5×10^{-5} and the maximum Capillary number is $Ca \equiv \mu U_d/\gamma = 0.05$. This low Reynolds number justifies the Stokes flow (equation 5.5a) and BIM simulations. The low capillary number justifies use of the Voinov-Hocking-Cox model. The Bond number is $Bo = \rho g R_0^2/\gamma = 0.2$, justifying neglect of gravity.

5.6 Numerical simulations

The boundary integral method is used to compute the tractions $\boldsymbol{\sigma} \cdot \boldsymbol{n}$ and the velocity $\boldsymbol{v}$ along the boundary of the liquid bridge. The experimental images are used as boundary conditions on the macroscopic shape and the velocity of the free interface. The microscopic free interface shape is obtained through an iterative process using the boundary conditions on the free interface (equations 5.9). The slip-length is adjusted until it satisfies the energy balance (equation 5.4).

5.6.1 Boundary integral method

The advantage of the boundary integral method is that only points along the interfaces need be computed. Along the boundary, point forces of magnitude $\boldsymbol{F}$ centered at $\boldsymbol{\eta}$ determine the flow within the domain [61]. The flow velocity, pressure and total stress tensor due to a single point force are given by

$$\hat{\boldsymbol{v}} = \frac{1}{8\pi\mu}\left(\frac{\boldsymbol{I}}{|\boldsymbol{x}-\boldsymbol{\eta}|} + \frac{(\boldsymbol{x}-\boldsymbol{\eta})(\boldsymbol{x}-\boldsymbol{\eta})}{|\boldsymbol{x}-\boldsymbol{\eta}|^3}\right)\cdot \boldsymbol{F}, \tag{5.26}$$

$$\hat{p} = \frac{1}{4\pi}\left(\frac{(\boldsymbol{x}-\boldsymbol{\eta})}{|\boldsymbol{x}-\boldsymbol{\eta}|^3}\right)\cdot \boldsymbol{F} \text{ and} \tag{5.27}$$

$$\hat{\boldsymbol{\sigma}} = \frac{3}{4\pi}\left(\frac{(\boldsymbol{x}-\boldsymbol{\eta})(\boldsymbol{x}-\boldsymbol{\eta})(\boldsymbol{x}-\boldsymbol{\eta})}{|\boldsymbol{x}-\boldsymbol{\eta}|^5}\right)\cdot \boldsymbol{F}. \tag{5.28}$$

For any two vector fields $\hat{\boldsymbol{v}}$ and $\boldsymbol{v}$ the following vector identity holds,

$$\hat{\boldsymbol{v}}\cdot\boldsymbol{\nabla}\cdot\boldsymbol{\sigma} - \boldsymbol{v}\cdot\boldsymbol{\nabla}\cdot\hat{\boldsymbol{\sigma}} = \boldsymbol{\nabla}\cdot(\hat{\boldsymbol{v}}\cdot\boldsymbol{\sigma} - \boldsymbol{v}\cdot\hat{\boldsymbol{\sigma}}) + \boldsymbol{\nabla}\,\boldsymbol{v}\colon\hat{\boldsymbol{\sigma}} - \boldsymbol{\nabla}\,\hat{\boldsymbol{v}}\colon\boldsymbol{\sigma}. \tag{5.29}$$

Setting one of the vector fields to be that from a point source, the following Green's function is obtained

$$\boldsymbol{v}(\boldsymbol{x}) + \frac{3}{4\pi}\int \frac{(\boldsymbol{x}-\boldsymbol{\eta})(\boldsymbol{x}-\boldsymbol{\eta})(\boldsymbol{x}-\boldsymbol{\eta})}{|\boldsymbol{x}-\boldsymbol{\eta}|^5}\cdot\boldsymbol{v}(\boldsymbol{\eta})\cdot\boldsymbol{n}(\boldsymbol{\eta})dA_\eta = \frac{1}{8\pi\mu}\int\left(\frac{\boldsymbol{I}}{|\boldsymbol{x}-\boldsymbol{\eta}|}+\frac{(\boldsymbol{x}-\boldsymbol{\eta})(\boldsymbol{x}-\boldsymbol{\eta})}{|\boldsymbol{x}-\boldsymbol{\eta}|^3}\right)\cdot(\boldsymbol{\sigma}(\boldsymbol{\eta})\cdot\boldsymbol{n}(\boldsymbol{\eta}))\,dA_\eta. \tag{5.30}$$

This result is attributed to Ladyzhenskaya [59]. If the velocity is evaluated at a boundary, the jump condition must be used [77]. Due to axisymmetry, the azimuthal direction is integrated analytically. The Green's function can be expressed in terms of complete elliptic integrals as described by Lee [62]. This simplifies the area integration to an integration along the arclength s_η of the liquid boundary in the $r-z$ plane.

Equation 5.30 is discretized as described by Youngren [108]. For every point $\boldsymbol{\eta}$ on the surface, 32 integration points were used along the interface s_η. The points $\boldsymbol{\eta}$ were spaced in a geometric series symmetrically about the contact-line, such that the spacing between the points closest to the contact-line was $b/50$ for the local slip and $\beta/50$ for the Navier slip condition. One-hundred point forces were placed along the top liquid-solid substrate; this resulted in some 200 to 400 points $\boldsymbol{\eta}$ along the entire boundary.

The axisymmetric Green's function has singular integrands when $r=0$ and $\boldsymbol{\eta}=\boldsymbol{x}$. Close to these singularities, the integrals over s_η were performed analytically using expansions of the elliptic integrals given by Lee [62] (where π has been moved to the numerator in their equations [A11]-[A16] as described by Davis [22] and $2/k'^4$ has been changed to $1/k'^4$ in equation [A23]). Youngren [108] suggests analytically integrating up to 10% of the region where $\boldsymbol{\eta}=\boldsymbol{x}$. Close to the contact-line, the elliptic functions took on such extremely large values that their differences could not be computed accurately using the machine

precision. Here the integral over all 32 arclength points close to $\boldsymbol{\eta} = \boldsymbol{x}$ was substituted for those done analytically. Analytic calculations were done with computer algebra to first order (shown in Appendix G) and confirmed with those obtained by Nitsche [76]. Close to the contact-line, integrands in the single layer beyond the 32 integration points where $\boldsymbol{\eta} = \boldsymbol{x}$ also caused round-off errors. Additional approximations were done in this region (Appendix G).

The fidelity of the code was verified by cutting in half the number of points $\boldsymbol{\eta}$; a difference of less than 3% in $\boldsymbol{\sigma} \cdot \boldsymbol{n}$ and less than 0.2% in $\boldsymbol{v}$ were observed. The fidelity of the method is demonstrated by the nearly equal $\dot{\mathcal{A}}$ and $-\bar{\mathcal{D}}$ in figure 5.3.

5.6.2 Microscopic region

An iterative scheme is used to calculate the shape of the free interface in the microscopic region (illustrated in figure 5.6). First the velocity, pressure and shape of the free interface in the macroscopic region is obtained from the experiment. In the macroscopic region the no-stress condition and the kinematic condition are used to find the tangent velocity and the normal traction on the free interface. The microscopic contact-line velocity is assumed to be the same as the macroscopic velocity; i.e. $U_m = U_d$. As a result, the assumption in equation 5.18b is always true. For the first iteration, a linear extrapolation of the free interface is used in the microscopic region, therefore $\theta(z) = \theta_d$. The BIM simulation is run using the tangent component of the Young-Lapace equation (equation 5.9a), that is $\boldsymbol{\sigma} \cdot \boldsymbol{n} \cdot \boldsymbol{t} = 0$, and the kinematic boundary condition (equation 5.9b) where $dR/dt = U_d$ in the microscopic region. We also guess

a slip-length; the guess is arbitrary and its correction will be described in section 5.6.3. The BIM simulation computes $\boldsymbol{\sigma} \cdot \boldsymbol{n} \cdot \boldsymbol{n}$ and a new microscopic surface is constructed using the ODE system 5.10 where the curvatures are given by the normal component of the Young-Laplace equation (equation 5.9a). The bending in the microscopic region has a negligible influence on the total volume, therefore the volume constraint (equation 5.11) can be neglected. The boundary conditions for constructing the free interface are obtained from the experiment; specifying the radius $R(z = h_d)$ and the contact-angle $\theta(z = h_d) = \theta_d$ turns the system 5.10 into an initial value problem. Using the new microscopic free interface, the BIM simulation is run on the entire domain and the surface is iterated until the new microscopic angle θ_m is within 1° of the previous iteration.

For the hydrophilic substrates, the angle θ from equation 5.10 frequently went to zero below the height of the substrate ($z < h_m$). Once the angle reaches zero the Young-Laplace equation cannot decrease the pressure any more and still make contact with the solid surface. These experiments may have formed a precursor layer which has a low pressure due to effects neglected in the simulation, such as van der Waals attraction (cf. [24]). For this reason *only simulations on the hydrophobic substrate are presented.*

5.6.3 Slip-length

The slip-length is found by matching the viscous dissipation to the rate of change of surface energy using equation using equation 5.24. If the viscous dissipation was too small in magnitude, then the slip-length was decreased. If the viscous dissipation was too large, or the the angle θ went to zero before

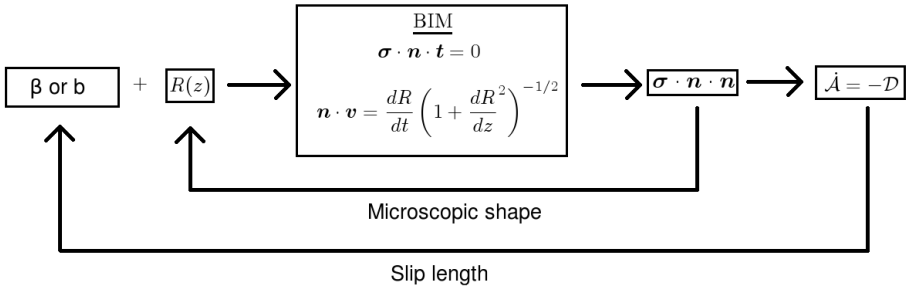

Figure 5.6: Schematic of iteration for computation of microscopic shapes and slip-lengths.

$z = h_m$, then the slip-length was increased. This was done two different ways; first a constant slip-length was found that best matches the energies for the entire change-of-state event. The second method found a slip-length so that the energy match was within 10% for each experimental image. These two methods were performed with each of the slip-length models (LS and NS).

A schematic of how the two iterations, in conjunction with the BIM, are used to obtain the microscopic region and the slip-length is shown in figure 5.6. The slip-length and free interface shape are first guessed. Then the tangent component of the Young-Laplace along with the kinematic condition are used in the BIM to find the normal tractions. The normal traction is used with the ODE system 5.10 to find the shape of the microscopic region. Then the slip-length is adjusted until the rate of surface energy loss is equal to the viscous dissipation.

5.7 Simulation results

The slip-length and microscopic region shape are computed using the BIM. The contribution of the surface integrals to the viscous dissipation (in equation 5.24)

as well as the location of viscous dissipation within the bulk are calculated. The flow profile and free interface shape as well as the tangent velocity and tractions along the interfaces are also obtained.

5.7.1 Energy loss due to viscous dissipation

The viscous dissipation is calculated according to equation 5.24 for constant slip-lengths of $b = 135nm$ for LS and $\beta = 23nm$ for the NS condition. As shown in figure 5.7, the rate of viscous dissipation for these constant slip values match the shape obtained from the loss of surface energy (equation 5.17). It was verified that the assumption used to calculated the surface energy (equation 5.18a) was satisfied by at least one order of magnitude for each frame. The error bars in the figure represent the uncertainty in the total energy lost which is a result of the uncertainty in the equilibrium contact-angles. The slip-length required for the total viscous dissipation to pass through the upper error bars is $b = 225nm$ for LS and $\beta = 33nm$ for NS. The slip-length required for the lower error bars (smaller equilibrium contact-angle) is $b = 85nm$ and $\beta = 13nm$.

The viscous dissipation has two contributions, one from the viscous bending of the free interface and another from the liquid-solid interface. When the LS boundary condition is applied, the integral for the viscous dissipation along the liquid-solid region is zero. The dissipation must be accounted for by the viscous bending alone. For the NS boundary condition the term $\int_{ls} \boldsymbol{\sigma} \cdot \boldsymbol{n} \cdot \boldsymbol{v} dA$ represents the dissipation that would have happened if the domain would have been extended a length β to satisfy the no-slip condition. The liquid-solid contribution is positive, and as a result the free interface must bend more for the

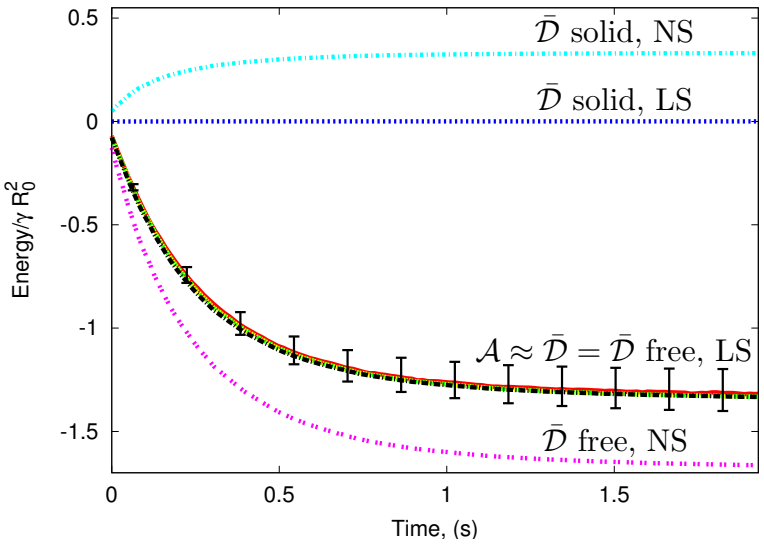

Figure 5.7: Calculated contributions to energy dissipated $\bar{\mathcal{D}} = \bar{\mathcal{D}}_{free} + \bar{\mathcal{D}}_{solid}$ (equation 5.24) for the local slip (LS) and Navier slip (NS) boundary conditions. Loss of surface energy $\mathcal{A}$ (equation 5.19) is almost exactly equal to dissipation $\bar{\mathcal{D}}$ for both NS and LS. Slip-length is used as a fitting parameter.

total dissipation to match the loss of surface energy.

The viscous dissipation has been computed using stresses and velocities on the interface; however, the actual frictional losses occur within the fluid. We seek to compute the viscous dissipation that happens within a given radius R_v of the contact-line (see inset of figure 5.8). The viscous dissipation within this region of the contact-line was computed by creating a new boundary around the area of interest, computing the velocity on this boundary using the Green's function (equation 5.30), using these velocities as the boundary conditions for a new BIM simulation in order to compute $\boldsymbol{\sigma} \cdot \boldsymbol{n}$ along the boundary completely submerged in the liquid and then finding the dissipation according to the surface integral $\int \boldsymbol{\sigma} \cdot \boldsymbol{n} \cdot \boldsymbol{v} dA$. The fraction of the total dissipation is shown as a function of the logarithmic distance from the contact-line in figure 5.8. The

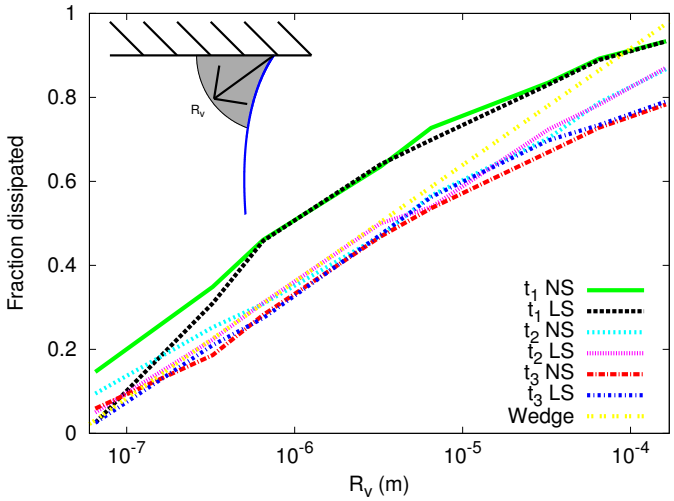

Figure 5.8: Fraction of total viscous dissipation within radius R_v of contact-line for local slip (LS) and Navier slip (NS) models at subsequent times $t_1 = 0.096s$ (early), $t_2 = 0.304s$ (intermediate) and $t_3 = 1.008s$ (late). The wedge model predicts a linear relation.

fraction of total dissipation is calculated for both boundary conditions at three instances of time; the first when the bridge is rapidly dissipating energy, the second at an intermediate stage and the third when the total energy dissipated is roughly constant.

The fraction of the total dissipation is proportional to the logarithmic distance to the contact-line. This might have been expected from a simple wedge model. For a wedge of angle θ_d and velocity U_d along one side and a no-shear along the other side, the stream function is given by

$$\psi = \frac{U_d \tilde{r}}{\theta_d - \sin(\theta_d)\cos(\theta_d)} \left[-\sin^2(\theta_d)\alpha \sin(\alpha) - \sin(\theta_d)\cos(\theta_d)\alpha\cos(\alpha) + \theta_d \sin(\alpha) \right] \tag{5.31}$$

where $\tilde{r}$ is the distance from the contact-line and α is the angle measured from the solid through the liquid (cf. [52]). According to this model, the dissipation

occurring in a wedge of radius R_v is

$$\mathcal{D}_w = \frac{2U_d^2 \mu \sin^2(\theta_d)}{\theta_d - \cos(\theta_d)\sin(\theta_d)} ln(R_v/R_{in}) \tag{5.32}$$

where R_{in} is the location where the solution is cut off to prevent singular dissipation. The fraction of the total dissipation occurring within a wedge of radius R_v is

$$\mathcal{D}_w/\mathcal{D} = \left(\ln(R_v) - \ln(R_{in})\right) / \left(\ln(R_{out}) - \ln(R_{in})\right) \tag{5.33}$$

where R_{out} is the size of the wedge. Both R_{in} and R_{out} are not predicted by the wedge model. The wedge model with $R_{in} = 50nm$ and $R_{out} = 200\mu m$ is shown in figure 5.8 to demonstrate the applicability of equation 5.33. The zero dissipation at small R_v and the flattening of the curves for high R_v represent flows that are not self-similar. The radii R_{in} and R_{out} represent the regions where dissipation occurs for this single wedge model; they do not necessarily correspond to L_{in} and L_{out} of the matched asymptotic solution.

Figure 5.8 shows the viscous dissipation is more localized about the contact-line at earlier times when the contact-line velocity and the dynamic contact-angle are larger. The dissipation within the slip region for all three times displayed is less than 20% of the total dissipation. The Navier slip condition causes the dissipation to occur closer to the contact-line; this is expected because the Navier slip still provides resistance close to the contact line, whereas the local slip does not provide any resistance there at all.

The flow field for early, intermediate and late times are shown in figure 5.9. The velocity profile within the bridge is computed using the Green's function (equation 5.30). The reference frame is fixed in the lab. Fluid is taken from from the free interface far from the contact-line and pulled to the contact-line

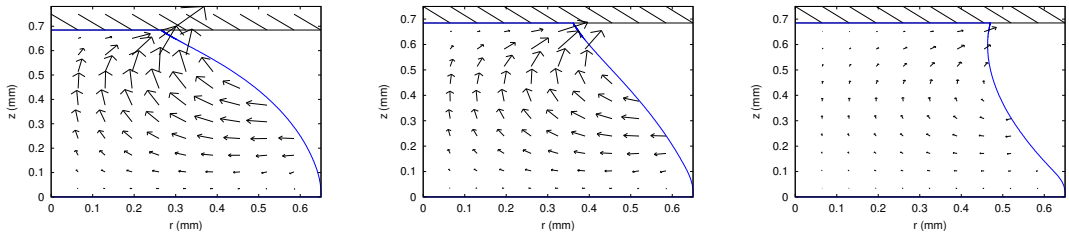

Figure 5.9: Entire flow field for $t_1 = 0.096s$ (left), $t_2 = 0.304s$ (middle) and $t_3 = 1.008s$ (right) under constant $b = 135nm$ local slip condition.

through a single vortex. The center of the vortex moves further away from the contact-line for later times. For these figures the type of slip is insignificant to the motion of the bulk flow.

In figure 5.10 the flow profile is viewed in the reference frame moving with the contact-line. Most of the viscous bending predicted by the simulation is within $\sim 500nm$ of the contact-line, a region much smaller than what is visible through the experimental setup (8 μm per pixel). Fluid is 'stagnant' within $\sim 50nm$ of the contact-line, the fluid here moves along with the contact-line. Experiments done by Dussan [29] show that a drop of dye at the contact-line moves with the bulk flow predicted by the wedge model; this is consistant with the scale of the 'stagnation' region, as this would not be visible by the naked eye.

The velocity profiles in figure 5.10 show a 'tank treading' behavior away from the contact-line. To further explore this, the tangent velocity in the reference frame moving with the contact-line is plotted in figure 5.11(b). Here the abscissa is the logarithmic arclength from the contact-line along the interface, sketched in figure 5.11(a). A straight line would indicate tank-treading behavior. The tangent velocity far from the contact-line along the liquid-solid interface

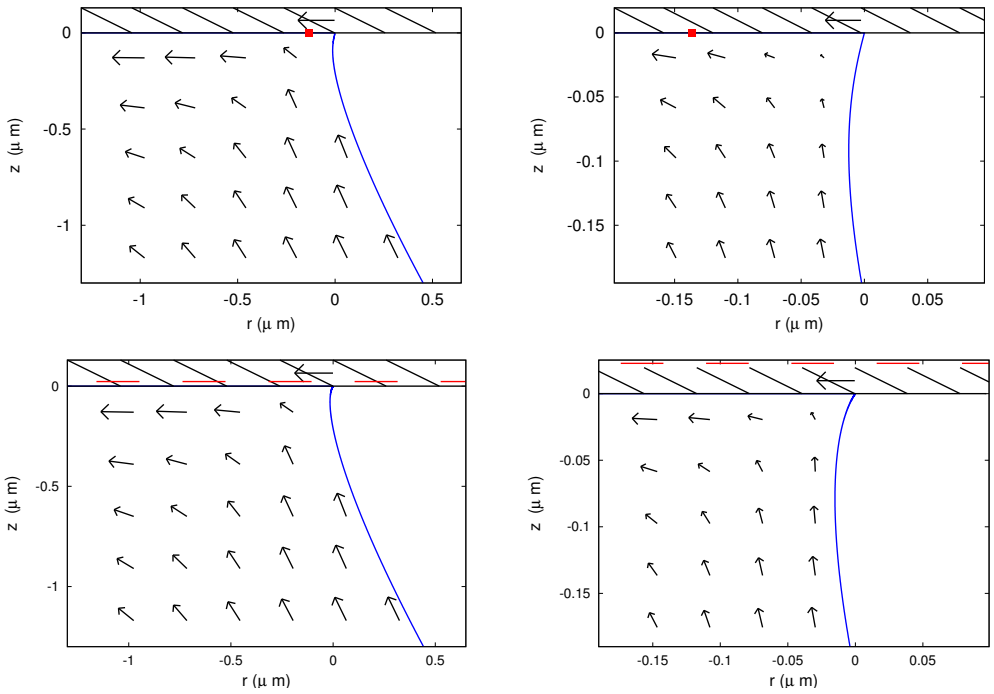

Figure 5.10: Velocity fields and slip conditions at t_1 in a reference frame moving with the contact-line (solid velocity indicated by top arrow). The top row is for local slip (LS) where $b = 135nm$ is indicated by the square. The bottom row is for the Navier slip (NS) condition where $\beta = 35nm$ is indicated by the dashed line. Velocity vector lengths have been scaled to the plot range ($O(1\mu m)$ left column and $O(0.1\mu m)$ right column).

is equal to the contact-line velocity. The velocity drops off abruptly where slip is applied for the LS boundary condition and then levels off at a non-zero value. For the NS boundary condition, the velocity drop off is slightly smoother. Along the free interface, the tangent velocity is zero close to the contact-line and comes to a value similar to the contact-line velocity within $1\mu m$ of the contact-line. The velocity at the bottom of the bridge is the negative contact-line velocity ($-U_m$) because here the tangent points in the opposite direction to the movement of the solid in the moving reference frame.

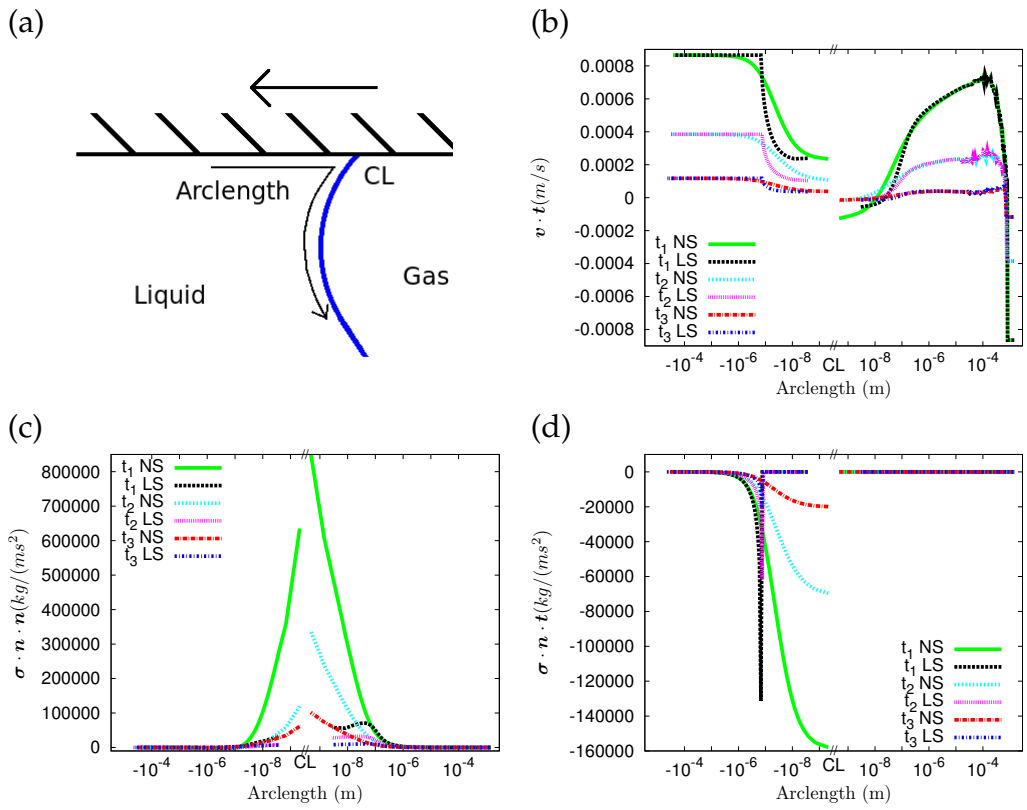

Figure 5.11: Along the solid-liquid and free interface in the moving frame (a), tangent velocity (b), normal traction (c) and tangential traction (d) at times $t_1 = 0.096s$, $t_2 = 0.304s$ and $t_3 = 1.008s$ for local slip (LS) and Navier slip (NS) boundary conditions.

The magnitude of the normal traction along the interfaces is shown in figure 5.11(c). The negative curvature of the free interface causes very large normal tractions. These cause a pressure drop which drives the fluid into the contact-line region, therefore moving the contact-line. The driving pressure is more negative at early times when the contact-line velocity is faster. The Navier boundary condition has a more negative pressure than the local slip due to the extra viscous bending that must occur to dissipate all the energy. The simulations do not show a constant value of the normal traction as the contact-line is approached for the NS boundary condition, and this issue is not settled with higher resolu-

tion simulations.

The tangential traction for the LS boundary condition is zero for the free interface and along the local no-shear boundary of the solid (see figure 5.11(d)). The tangential traction reaches a minimum at the location of the no-slip boundary condition closest to the contact-line. For the NS condition the normal traction is most negative at the location of the contact-line. Unlike the normal traction, the tangential traction for the NS boundary condition converges close to the contact-line. The maximum shear-rate is calculated using the Newtonian viscosity value to be $28,000s^{-1}$; at this shear-rate, slip-lengths comparable to those found here have been reported for PDMS [75]. Slip is common in long chain polymers, but it has also been observed in pure fluids such as water [19] and hexadecane [109]; therefore the hydrodynamic model may also work for smaller molecules than those tested here. The high shear-rates may also cause shear-thinning, and this has been used as a possible explanation of slip at contact-lines [104]. Based on the rheological data, we expect shear-thinning to be significant when the shear-rates approach $1,000s^{-1}$, in agreement with literature data [55].

5.8 Microscopic contact-angle relation

The balance of surface energy and viscous dissipation can be used to analytically determine the microscopic contact-angle given a slip condition. The surface energy used for this calculation includes the microscopic terms (equation 5.17); therefore the results in this section are independent of the assumptions in equations 5.18.

The Young-Laplace equation (5.9a) is inserted into the energy balance (equation 5.24) to give

$$\dot{\mathcal{A}} = \int_{\Omega} \gamma \left(\frac{1}{r_1} + \frac{1}{r_2} \right) \boldsymbol{n} \cdot \boldsymbol{v} dA - \int_{ls} \boldsymbol{\sigma} \cdot \boldsymbol{n} \cdot \boldsymbol{v} dA. \tag{5.34}$$

The differential geometry relation (equation 5.20) is applied to the entire free interface to convert the curvature terms into changes in free area

$$\dot{\mathcal{A}} = \gamma \frac{d}{dt} \int_{\Omega} dA - \gamma \oint_{\ell_m} U_m \cos\theta_m d\ell + \int_{ls} \boldsymbol{\sigma} \cdot \boldsymbol{n} \cdot \boldsymbol{v} dA. \tag{5.35}$$

By definition of the surface energy (equation 5.17)

$$0 = \int_{ls} \boldsymbol{\sigma} \cdot \boldsymbol{n} \cdot \boldsymbol{v} dA + \oint_{\ell_m} U_m \gamma \left(cos\theta_m - cos\theta_e \right) d\ell \tag{5.36}$$

The liquid-solid area integral term represents the reduction in dissipation due to the slip condition. The line integral is the rate of work done by the microscopic unbalanced Young-Dupré force.

The LS boundary condition requires that, along the liquid-solid interface, either the velocity is zero or the tangential stress is zero, therefore $\int_{ls} \boldsymbol{\sigma} \cdot \boldsymbol{n} \cdot \boldsymbol{v} dA = 0$. As a consequence the microscopic contact-angle is fixed,

$$\theta_e = \theta_m \tag{5.37}$$

for both advancing and receding contact-lines. This result agrees with that obtained by Voinov [99].

For the NS boundary condition the energy can be bounded using the definition 5.8b,

$$\int_{ls} \boldsymbol{\sigma} \cdot \boldsymbol{n} \cdot \boldsymbol{v} dA = - \int_{ls} \frac{\mu}{\beta} |v|^2 dA \leq 0. \tag{5.38}$$

Inserting the above equation into 5.36 gives a bound on the energy lost due to the microscopic unbalanced Young-Dupré force

$$\oint U_m \gamma \left(cos(\theta_e) - cos(\theta_m) \right) d\ell \leq 0. \tag{5.39}$$

For advancing contact-lines, $U_m > 0$,

$$\theta_m \leq \theta_e. \tag{5.40}$$

For receding contact-lines, $U_m < 0$,

$$\theta_e \leq \theta_m. \tag{5.41}$$

For all but a few anomalies $\theta_e < \theta_d$ for advancing and $\theta_d < \theta_e$ for receding contact-lines [3]. This gives an ordering of the angles, $\theta_m \leq \theta_e < \theta_d$ for advancing and $\theta_d < \theta_e \leq \theta_m$ for receding contact-lines (see figure 5.12). That is the contact-line may *microscopically bend in the direction opposite that the macroscopic free interface is pulled*. Such bending creates a low pressure region to move the fluid.

In figure 5.12 the macroscopic and microscopic contact-angles are shown for the BIM simulations. For the LS condition, as predicted by equation 5.37, the microscopic contact-angle is roughly $\theta_e = 68.5°$. For the NS condition, the microscopic contact-angle is less than the equilibrium value, especially at early times when the contact-line velocity and tangential tractions are large (cf. figure 5.7). The noise in the simulation data is roughly the same as the noise in the experimental data for the macroscopic dynamic contact-angle. Matching the energy for each frame resulted in larger microscopic contact-angles for early times.

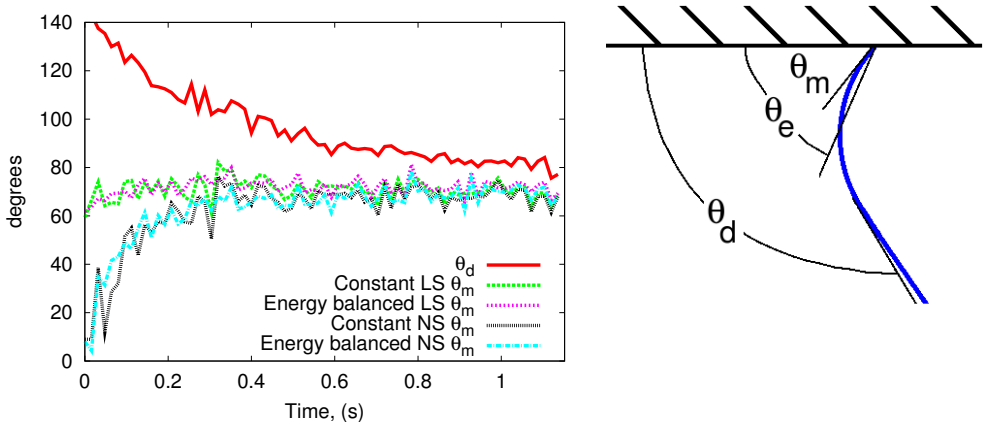

Figure 5.12: Left: Measured dynamic angle (θ_d) and computed microscopic contact angle (θ_m) for Navier (NS) and local (LS) slip for constant slip-length parameters and for those adjusted frame-by-frame to satisfy the energy balance. Numerical accuracy of θ_m is $\pm 1^\circ$. Right: Necessary ordering of the angles for the case of an advancing contact-line.

5.9 Relation to Voinov-Hocking-Cox model

A simple relation between contact-angle and contact-line velocity is often desired. Here, we relate our results back to the Voinov-Hocking-Cox model (equation 5.1).

The Voinov-Hocking-Cox model assumes a microscopic region where some kind of slip occurs and an outer wedge flow with a no-slip boundary condition along the solid surface. For simplicity, we relate this model to the results from the LS condition. The slip-length is assumed to correspond to the inner length scale and the energy balance specifies the microscopic contact angle $\theta_m = \theta_e$. For the outer length scale L_{out}, we choose the length over which viscous bending occurs. An estimate of the viscous bending scale is the location (z) at which the curvature is less than an averaged curvature of the entire bridge by an amount equal to the curvature of a sphere $(1/r_1(z) + 1/r_2(z)) = < (1/r_1 + 1/r_2) > -2/R_0$.

The location for L_{out} can be obtained from the images or from the numerical simulations. Both of these methods give values of $L_{out} \approx 25\mu m$ throughout the change-of-state.

The experimental data to test the Voinov-Hocking-Cox model (equation 5.1) are the capillary number Ca and the dynamic contact-angle θ_d. The capillary number is predicted in figure 5.13 (left) using $\theta_m = \theta_e = 68.5°$, $L_{out} = 25\mu m$ and $L_{in} = b = 135nm$. The only parameter not obtained directly is b. Relating the Voinov-Hocking-Cox model to the NS boundary condition is more difficult because the microscopic angle is not specified by the energy balance and the value of the inner length scale is not obvious (because the slip depends on the shear rate).

The length of the inner region needed for the Voinov-Hocking-Cox model (with $\theta_e = \theta_m$ and $L_{out} = 25\mu m$) to match the experimental data perfectly is plotted in figure 5.13 (right). The slip-lengths using the LS and NS boundary conditions to match the viscous dissipation to the surface energy loss for each frame, are also shown in figure 5.13. The NS length (β) is smaller than the LS length (b) by an order of magnitude. Note, however, that β does not represent the length over which slip occurs. The length over which the velocity of the liquid is greater than 10% of the contact-line velocity for the NS is shown in figure 5.13. This length is very similar to the outer length scale; therefore this value could be used as L_{out}, and the predictions would remain the same (since the Ca terms dominate the $g(\theta_m)$ terms at high Ca, when the two slip models predict different microscopic angles). These three slip-region lengths are similar for early times of the change-of-state. For late times the slip region predicted by the Voinov-Hocking-Cox model decreases, whereas the slip-length obtained

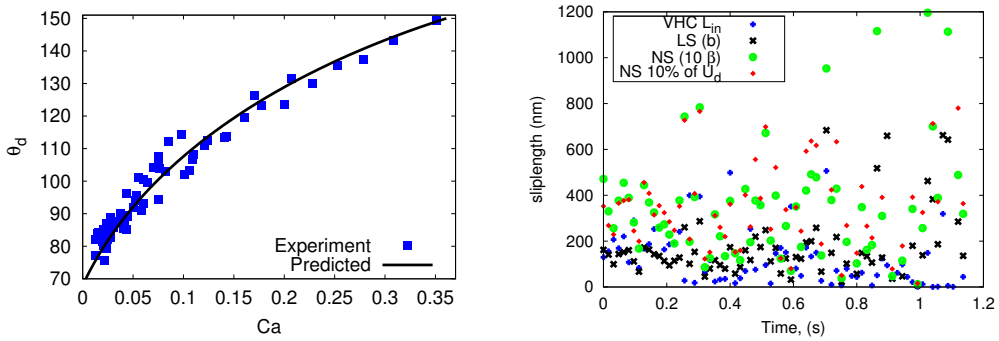

Figure 5.13: Left: dynamic contact-angle θ_d against Ca, as measured and predicted by Voinov-Hocking-Cox (VHC) model, where $\theta_m = \theta_e$, $L_{in} = b$ and L_{out} is the viscous bending length. Right: L_{in} needed to make the VHC model match the experimental data exactly. Slip-lengths b for LS and β for NS conditions with the energy balance (equation 5.24) satisfied at each frame. The slip-length for the NS model is multiplied by ten for visual purposes. The length along the solid-liquid boundary at which the velocity is 10% of the contact-line velocity is shown for the NS boundary condition (NS 10%).

from the full simulations increases.

5.10 Concluding Remarks

The change-of-state that occurs when a drop spreads on a solid surface is driven by a decrease in potential surface energy. The rate of surface energy change is expressed equivalently as the rate of work done by the interface using a purely geometric equation. This power exerted has two components, one from viscous bending, and another due to an unbalanced Young-Dupré force. From a macroscopic view, where no viscous bending is observed, the loss of energy is equivalent to the velocity multiplied by an unbalanced Young-Dupré force at the contact-line. On a closer look at the contact-line, viscous bending will

be observed and the microscopic angle will decrease as the contact-line is approached. In the hydrodynamic model, the contact-angle will decrease to (at least) the equilibrium contact-angle. At this location the unbalanced Young-Dupré force is zero, and the energy decay can be expressed entirely as a viscous bending rate of work.

Through a thermodynamic argument as well as an energy balance on a control volume along the interfaces, it has been shown that the surface energy decay rate is equal to the viscous dissipation within the fluid. This 'overall' balance adds an extra equation to the hydrodynamic equations that govern the bridge dynamics. For slip models with a single parameter, such as the local slip-length b or the Navier slip-length β, the overall balance can be used to find the slip-length. The overall balance cannot determine the type of slip, nor does the type of slip influence the macroscopic behavior of the contact-line.

The objective of this study is not to compute accurate slip-lengths, but we do learn that reasonable slip-lengths are needed to resolve the contact-line singularity. Using the boundary integral method, slip-lengths of $135nm$ for the local slip and $23nm$ for the Navier slip boundary condition are obtained. These constant slip-length values capture the rate of energy decay for all times throughout the change-of-state event. The slip-lengths reported are comparable to those reported on experiments of draining forces on a sphere for similar materials [75]. Simulations predict shear-rates as high as $28,000s^{-1}$; from the cone and plate experiment, shear-thinning effects become significant at $\sim 1,000s^{-1}$. Since high shear-rates occur very close to the solid boundary, it is appropriate to lump this effect into the apparent slip-lengths reported, which makes the true slip less than the apparent slip. The roughness of the surface is unknown, and a

rough surface can make the true slip greater than the apparent slip. [Spreading experiments are not ideal for measuring slip; the exponential dependence of slip-length on contact-line velocity (equation 5.1) results in large uncertainty in these measurements. Conversely, the contact-line velocity depends logarithmically on slip-length, therefore independent slip measurements would not need to be very precise in order to accurately predict contact-line velocities.]

The simulations of the fluid reveal properties of spreading. The majority of the fluid near the contact-line has a 'tank-treading' behavior as observed by Dussan [31]. The fluid within the slip region remained almost stagnant. Previous experiments which have tried to elucidate the flow in this region [31] were not at sufficiently high resolutions to be relevant to the prediction of a stagnant region here. The simulations predict significant viscous bending within a micrometer of the contact-line, although experiments show that viscous bending occurs as far as $25\mu m$ from the contact-line. The viscous bending causes negative pressure at the contact-line; this drives the fluid into the contact-line region. The normal traction diverges at the contact-line for NS, and converges to a value of $\sim 50,000Pa$ for LS. A possible effect of extremely low pressures is cavitation (cf. [25]); however, even the pressure for the NS boundary condition within $1nm$ of the contact-line is too small in magnitude for cavitation to occur. Due to the size of the polymer molecules, it is expected that the continuum model will break down at scales smaller than those simulated. The divergence of the normal traction for NS does not appear to have a significant effect on any other results in this work; since otherwise the results would have changed when the resolution of the simulation was changed.

The viscous dissipation was computed using the work done on the boundary

of the liquid. The majority of the work done happens in a region very close to the contact-line. Along the free interface work is primarily done in the viscous bending region. There is a small (negative) contribution to the energy decay due to the slip along the solid interface for NS; for LS this contribution is zero. Although $\mathcal{D}$ was evaluated using the work done on the liquid, the viscous dissipation of mechanical energy actually happens within the fluid. It was found that the amount of dissipation depends on the logarithm of the distance to the contact-line – as anticipated by a wedge model of the flow. Very little dissipation occurs in the stagnation region within the slip region.

The overall energy balance was used to analytically predict the microscopic contact-angle for both advancing and receding contact-lines. For the local slip condition the microscopic angle was shown to be equal to the equilibrium contact-angle for all contact-line velocities; this is consistent with the way in which the microscopic contact-angle has been chosen in previous studies [4, 82]. For the Navier slip condition the microscopic angle was bounded by the equilibrium angle. The microscopic angle bends in the opposite direction of the advancing angle, that is $\theta_m \leq \theta_e < \theta_d$ for advancing and $\theta_d < \theta_e \leq \theta_m$ for receding contact-lines.

With the knowledge of the microscopic contact-angle, the slip predicted from the LS and NS boundary conditions can be compared with the inner region (L_{in}) of the Voinov-Hocking-Cox model. When the length over which viscous bending occurs is used as the outer length scale, then slip-regions similar to slip-lengths predicted by the simulations were obtained. For late times in the change-of-state, when the contact-line velocities were small, the slip-length predicted by the Voinov-Hocking-Cox model decreased, whereas those from the

simulation increased.

This work has presumed that the contact-line movement phenomenon can be explained entirely by classical hydrodynamics using a slip for regions of high shear-rates. Calculated values of slip-lengths, shear-rates, pressures at the interfaces and flow profiles were found to be consistant with literature values and self-consistant given the approximations of the model. This need not always be the case. Other experiments, such as those for completely wetting fluids [24] or experiments with hydrodynamic assist [5] include other forces that may be important depending on context. All the parameters used in this study can be found using independent auxiliary experiments, and this was done for all parameters except the slip-length. Auxiliary experiments could be done to predict the contact-line motion in advance of the contact-line measurements.

CHAPTER 6

SUMMARY AND FUTURE WORK

6.1 Stability of coupled drops (Chapter 2)

The fixed points and stability of a network of coupled drops was found analytically for systems where the average volume was larger than hemispherical for an arbitrary number of drops N (see chapter 2). A simple extention of this problem is to remove the volume restriction and study drops with average volumes less than hemispherical. Also, the pressure-drop response could be changed so that it corresponds to a different physical problems, such as liquid bridges or rubber balloons. Bridges and rubber balloons have more complicated pressure-volume responses, therefore finding the stability analytically may be more difficult, however it may be worthwhile for a given application, such as the switchable adhesion device [97]. Complicated response diagrams may make it difficult to gain insight into simpler principles that may be more apparent for the drops. The pressure-drop response could also be changed without regard to physical application; for example, a different single turning-point response, or a response with two turning points. Such 'toy' responses could be used to probe if the number of small elements is always equal to the number of stable eigenvalues of a fixed point - it is seen from Appendix D that this does not have an obvious solution.

It was shown in section 2.4 that the dynamic and energy stability results for a system with a Lyapunov function are equivalent. This was proven using the result by McLachlan [68]. In this paper the Lyapunov function is not explicitly defined as being a strictly decreasing quantity, yet all the examples are

done with strictly decreasing Lyapunov functions. Proving the McLachlan result for a decreasing function would confirm that dynamic and energy stability are always the same for the drop systems, without the need to appeal to the unisignant. Geometric insight into this result could be gained by changing the metric tensor so that the fixed point is locally a gradient system.

6.2 Volume-scavenging (Chapter 3)

Volume-scavenging of drops determines to which of the basins-of-attraction an initial condition will travel. The basins-of-attraction are found for systems of three drops. For higher dimensional systems without symmetry the probability of winning is found by a heuristic argument - the two most connected drops each have a 50% chance of winning. Making this result more rigorous could help identify the domains of attraction for systems with symmetry. In systems with symmetry the invariant manifolds may be $N-1$ dimensional or less. Predicting the effect of a low-dimensional manifold is necessary to determine the domains-of-attraction close to the most unstable fixed point. Ideally, if the domains of attraction can be found and labeled, then the change-of-winner could be found analytically using higher-order expansions of the manifold using center manifold theory.

6.3 Coarsening dynamics (Chapter 4)

The coarsening rate for drops coupled by a variety of networks is found using the LSW model. The LSW model predicts a single pre-exponential factor regard-

less of network - this does not match the simulations. An improved LSW model could perhaps account for the dimension of the connections between elements.

Rigorous energy bounds have been found on such coarsening processes ([56, 34]), however these use an $\mathcal{H}^{-1}$ norm. This norm is difficult to translate into the thermodynamic energy of the system (given by the surface area multiplied by the surface tension). Finding a way to bound the thermodynamic energy may add insight into the pre-exponential factors. Rigorous bounds on the thermodynamic energy could provide insight into other coarsening processes, where there is frequent disagreement between experiments and theory [83]. The drop system is attractive for searching for the energy bound due to its simplicity.

The self-similar distribution of the drop volumes is stable based on the simulations done. For an initial condition that does not follow the self-similar distribution of drops a self-similar distribution of drops developed over several coarsening time periods. It would be interesting if a stability analysis of this distribution were done analytically. The stability of the distribution was recently analyzed numerically for the coarsening of thin films [42].

It may be possible to perform experiments to find the coarsening rate. The image acquisition would be easiest if this was done for a linear array. This may be somewhat tedious as it requires doing the same experiment about 100 times.

6.4 Bridge-drop change-of-state (Chapter 5)

The thermodynamic cycle for bridge-drop cycle is shown for constant volume, although it could also be presented for constant length (cf figure 1.1). The con-

stant volume or constant length cycles could be verified experimentally; although the theory for these cycles is quite standard. This could involve the measurement of force exerted by the liquid bridge.

The solid surface could be modified to observe some of the predicted results. The solid could be replaced with an elastic solid or a hydrogel to observe the normal traction close to the contact line (this would require a 2-d experiment in order to properly visualize). The slip-length could be modified by creating a patterned solid surface with known roughness. The liquid can also be modified so that it has a different contact-angle or slip-length. The choice of liquid is made difficult by the requirement that the Reynolds and Bond numbers remain small and that the liquid not be hygroscopic.

Limitations of the experimental apparatus could be overcome by changing the apparatus. The energy lost by the contact line can be found from the power, $mathcalP$ (as this expression has already been verified in this study). For example, for capillary-rise experiments the simulation of the fluid flow would be much simpler. The experiments in this study were only done for wetting fluids; de-wetting experiments would be a simple extension.

Bridge coalescence experiments could also be done with low viscosity liquids. Preliminary experiments show that capillary waves travel from the point of contact. The energy of these waves could be computed and added to the total energy balance. This could offer insights on how high Reynolds number contact lines move - is there the same mechanism of viscous dissipation or is the free interface going unstable and skipping along the surface? The fluid dynamics simulations of such bridges would require FEM, due to the mixture of high and low Reynolds number, which typically requires the full Navier-Stokes

equations.

Completely wetting fluids could be accounted for by adding intermolecular forces. The difficulty with such models is that the Haymaker constant may act as another 'fudge factor' - allowing this model to explain experimental results but not predict them. However, it would be interesting if the correct overall behavior of completely wetting fluids could be captured using a strictly hydrodynamic model.

APPENDIX A

EQUILIBRIUM AND STABILITY USING THE METHODS OF WEIERSTRASS AND POINCARE

The equilibrium of a variational problem can be found using the Euler-Lagrange equation. Two ways of finding the equilibrium are reviewed: using the second variation and the method of Poincare (Maddocks). A relation between the second variation and the method of Poincare is shown. Examples related to finding shapes of minimum area with constrained volume are given.

A.1 Equilibrium minimizing area with a conserved volume

In this section the equilibrium of a liquid bridge or drop are found. This section is a review of the results found in [7, 50, 37]. Consider the function that minimizes the functional

$$A = \int_{t0}^{t1} F(x, y, x', y')dt \tag{A.1}$$

with a constant value of

$$V = \int_{t0}^{t1} G(x, y, x', y')dt \tag{A.2}$$

where the prime indicates differentiation with respect to t. By introducing a Lagrange multiplier (λ), the integral of a new integrand

$$E \equiv F - \lambda G \tag{A.3}$$

can be minimized to find the minimum of A with constant V.

The functions $x(t), y(t)$ which minimize E are interpreted as a curve which is independent of the parametrization t. The variables x and y are intensive variables of E and x' and y' are extensive variables of E, therefore

$$E(x, y, kx'', ky') = kE(x, y, x', y'). \tag{A.4}$$

The Euler equation $E = E_{x'}x' + E_{y'}y'$ is obtained by differentiating with respect to k and setting $k = 1$. Due to the arbitrary nature of the parametrization, the limits of t will be set to 0 and 1 from now on.

The function that minimizes E is given by the Euler-Lagrange equation

$$0 = E_x - \frac{d}{dt}E_{x'} = E_y - \frac{d}{dt}E_{y'} \tag{A.5}$$

where the differentiation in the x or y coordinate is arbitrary due to the independence of the parametrization. Using equation A.4 the first variation was written by Weierstrass [7] as

$$0 = E_{xy'} - E_{yx'} + E_1(x'y'' - x''y') \tag{A.6}$$

where $E_1 = \frac{E_{x'x'}}{y'^2} = -\frac{E_{x'y'}}{x'y'} = \frac{E_{y'y'}}{x'^2}$.

For an axisymmetric surface-tension dominated shape the functional to minimize is the area, therefore

$$F = 2\pi y\sqrt{x'^2 + y'^2} \tag{A.7}$$

where x is the vertical coordinate and y is the radial coordinate. For a surface-tension dominated shape with a constrained volume, the integrand of the volume constraint is

$$G = \pi y^2 x'. \tag{A.8}$$

The first variation in the x-direction is given by equation A.5, which simplifies to

$$0 = 0 - \frac{d}{dt}\left[2\pi y \frac{x'}{\sqrt{x'^2 + y'^2}} - \lambda \pi y^2\right]. \tag{A.9}$$

From this equation we find that

$$\lambda = \frac{x'}{y\sqrt{x'^2 + y'^2}} + \frac{y'x'' - x'y''}{(x'^2 + y'^2)^{\frac{3}{2}}} = -2\mathcal{H} \tag{A.10}$$

where $2\mathcal{H}$ is the sum of the two principle curvatures. From the Young-Laplace equation, λ can be interpreted as the thermodynamic pressure (scaled by the surface tension) of a static fluid.

Integration of equation A.9 with respect to t gives

$$-\frac{2\pi y x'}{\sqrt{x'^2 + y'^2}} + \lambda \pi y^2 = C \tag{A.11}$$

where C is a constant. The solution to this equation is given by [50, 37] as

$$x = \alpha - \frac{2}{\lambda(1 + cos(\beta))}(E(\beta, (t_1 - t_0)t + t_0) + cos(\beta)K(\beta, (t_1 - t_0)t + t_0)) \tag{A.12}$$

$$y = \alpha - \frac{2}{\lambda(1 + cos(\beta))}\Delta(\beta, (t_1 - t_0)t + t_0) \tag{A.13}$$

where K and E are incomplete elliptic integrals of the first and second kind, β, α, t_0 and t_1 are undetermined coefficients and t is the parameter which goes from 0 to 1. The four undetermined coefficients can be found based on the boundary conditions of the problem. For example, for a liquid drop pinned at a radius R_0 the boundary conditions are

$$x(0) = R_0 \tag{A.14}$$

$$x(1) = 0 \tag{A.15}$$

$$y(0) = 0 \tag{A.16}$$

$$y'(1) = 0. \tag{A.17}$$

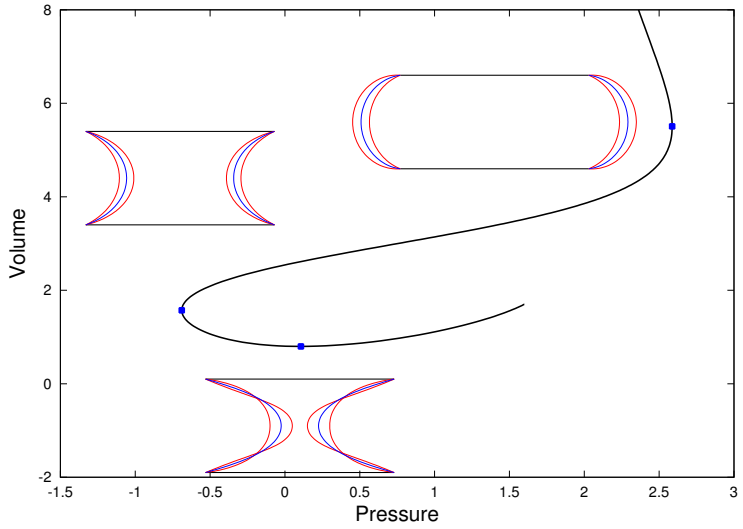

Figure A.1: Pressure-volume response of a liquid bridge. Inset figures show disturbances which make the bridge go unstable.

For a liquid bridge pinned at the top and bottom at a radius R_0 and having a height H

$$x(0) = R_0 \tag{A.18}$$

$$x(1) = R_0 \tag{A.19}$$

$$y(0) = 0 \tag{A.20}$$

$$y(1) = H. \tag{A.21}$$

The boundary conditions will determine the relation between λ and V. The solution in λ-V space (known as distinguished diagram), for the bridge is shown in figure A.1. The Lagrange multiplier has been labeled by its physical interpretation as pressure.

A.2 Method of Weierstrass

The stability of a solution is determined by the second variation. Weierstrass shows a simple way to express the change in stability in terms of determinants. This section is a review of the methods shown in [7, 50]; the results of this section were used in [37]. The determinants are related to the turning points in the preferred diagram, as was shown by [50].

A.2.1 Determinant criterion

Consider a disturbance u to the equilibrium shape x, y found in section A.1. This disturbance must satisfy the second variation. The second variation is given by Weierstrass ([7]) as

$$\delta^2 J = E_2 u - \frac{d}{dt}\left(E_1 \frac{du}{dt}\right) \tag{A.22}$$

where $E_2 = \frac{E_{xx}}{y'^2} - E_1 - \frac{1}{y'^2}\frac{d}{dt}\left(E_{xx'} - y'y''E_1\right)$ (which can be written in several other equivalent forms using the independence of parameter property). Differentiation of Weierstrass' form of the Euler-Lagrange equations (equation A.6) with respect to α and β shows that changes in stability, ($\delta^2 J = 0$) correspond to solutions

$$u = \theta_1(t) \equiv x'y_\alpha - y'x_\alpha \tag{A.23a}$$

$$u = \theta_2(t) \equiv x'y_\beta - y'x_\beta. \tag{A.23b}$$

A third solution $u = 0$ also satisfies equation A.22.

For a constant pressure (constant λ) disturbances, the only constraint on u is that its endpoints pass through zero; no volume constraint is necessary. The

solution $u = 0$ satisfies the boundary condition on the disturbance, therefore a non-trivial solution to A.22 is only necessary up to a point t (called the conjugate point), after which we can append the trivial solution. The nontrivial solution was stated in equation A.23, we seek solutions such that $u(0) = 0$ and $u(t) = 0$; that is, we seek the constants c_1 and c_2 such that

$$\begin{bmatrix} \theta_1(0) & \theta_2(0) \\ \theta_1(t) & \theta_2(t) \end{bmatrix} \begin{bmatrix} c_1 \\ c_2 \end{bmatrix} = \begin{bmatrix} 0 \\ 0 \end{bmatrix}. \tag{A.24}$$

A conjugate point occurs for each t where these equations have a non-trivial solution, that is each time the determinant of the matrix

$$DP(0,t) \equiv \begin{bmatrix} \theta_1(0) & \theta_2(0) \\ \theta_1(t) & \theta_2(t) \end{bmatrix} \tag{A.25}$$

is zero. Following a solution curve in λ-V space, the constant pressure stability must change when a new conjugate point is introduced or eliminated in the domain of t, that is when

$$0 = |DP(0,1)|. \tag{A.26}$$

According to Morse ([71]), the number of conjugate point in the domain of t is equal to the number of unstable directions.

For constrained disturbances we seek solutions to

$$E_2 u - \frac{d}{dt}\left(E_1 \frac{du}{dt}\right) = \mu U \tag{A.27}$$

where $U = G_{xy'} - Gx'y + G_1(x'y'' - x''y')$ and μ is an undetermined eigenvalue. The disturbance u must satisfy the constraint $\int_0^1 U u dt = 0$. The solutions shown in equation A.23 satisfy equation A.27 with zero eigenvalue. Taking the derivative of the Euler-Lagrange equation (equation A.6 with respect to λ gives a third

possible non-trivial solution

$$u = \theta_3(t) \equiv x'y_\lambda - y'x_\lambda. \tag{A.28}$$

As was done for the constant pressure disturbances, a non-trivial solution is appended to a trivial one. The conjugate points determine where the non-trivial solution ends. The conjugate point is determined by the location at which the matrix equation

$$\begin{bmatrix} \theta_1(0) & \theta_2(0) & \theta_3(0) \\ \theta_1(t) & \theta_2(t) & \theta_3(t) \\ \int_0^1 U\theta_1 dt & \int_0^1 U\theta_2 dt & \int_0^1 U\theta_3 dt \end{bmatrix} \begin{bmatrix} c_1 \\ c_2 \\ c_3 \end{bmatrix} = \begin{bmatrix} 0 \\ 0 \\ 0 \end{bmatrix} \tag{A.29}$$

has a non-trivial solution, indicated by a non-zero coefficients c_1, c_2 and c_3. Conjugate points are determined by singular matrices DV, where

$$DV(0,t) \equiv \begin{bmatrix} \theta_1(0) & \theta_2(0) & \theta_3(0) \\ \theta_1(t) & \theta_2(t) & \theta_3(t) \\ \int_0^1 U\theta_1 dt & \int_0^1 U\theta_2 dt & \int_0^1 U\theta_3 dt \end{bmatrix}. \tag{A.30}$$

The solution changes stability when a new conjugate point is introduced along the arclength of u, that is when

$$0 = |DV(0,1)| \tag{A.31}$$

We have two determinants which determine when the constant volume and constant pressure stability change.

A.2.2 Relation to turning points

The objective of this section is to relate the zero determinants of DP and DV to the turning points in the λ-V diagram. This section is a summary of the results presented in [50].

The parameters $\alpha, \beta, \lambda, t_0, t_1$ determine the value of V. In the distinguished diagram, let s be the arclength of the curve which represents the equilibrium solutions. The values of the parameters $\alpha, \beta, \lambda, t_0, t_1$ can be given as a function of the arclength s as well. The boundary conditions for the free interface shape are fixed, therefore

$$\dot{x}|_{t=0} = \dot{x}|_{t=1} = \dot{y}|_{t=0} = \dot{y}|_{t=1} = 0 \tag{A.32}$$

where the dot represents total differentiation with respect to t. The total volume does not depend on t as well, therefore $\dot{V} = 0$. The total derivatives can be expanded and the previous five relations are written in matrix form as

$$\begin{bmatrix} x_\alpha(0) & x_\beta(0) & x_\lambda(0) & x_{t_0}(0) & x_{t_1}(0) \\ x_\alpha(1) & x_\beta(1) & x_\lambda(1) & x_{t_0}(1) & x_{t_1}(1) \\ y_\alpha(0) & y_\beta(0) & y_\lambda(0) & y_{t_0}(0) & y_{t_1}(0) \\ y_\alpha(1) & y_\beta(1) & y_\lambda(1) & y_{t_0}(1) & y_{t_1}(1) \\ V_\alpha & V_\beta & V_\lambda & V_{t_0} & V_{t_1} \end{bmatrix} \begin{bmatrix} \dot{\alpha} \\ \dot{\beta} \\ \dot{\lambda} \\ \dot{t_0} \\ \dot{t_1} \end{bmatrix} = \begin{bmatrix} 0 \\ 0 \\ 0 \\ 0 \\ \dot{V} \end{bmatrix}. \tag{A.33}$$

This matrix equation simplifies because $x_{t_1}(0) = x_{t_0}(1) = y_{t_1}(0) = y_{t_0}(1) = 0$, $V_i = \int_0^1 U u_i dt$, and $V t_0 = V_{t_1} = 0$. Using Cramer's rule and the relation

$$\begin{vmatrix} x_\alpha(0) & x_\beta(0) & x_{t_0}(0) & x_{t_1}(0) \\ x_\alpha(1) & x_\beta(1) & x_{t_0}(1) & x_{t_1}(1) \\ y_\alpha(0) & y_\beta(0) & y_{t_0}(0) & y_{t_1}(0) \\ y_\alpha(1) & y_\beta(1) & y_{t_0}(1) & y_{t_1}(1) \end{vmatrix} = |DP(0,1)| \tag{A.34}$$

we find that

$$|DV(0,1)|\dot{\lambda} = |DP(0,1)|\dot{V} \tag{A.35}$$

Thus, if the curve in the distinguished diagram has no corners then we can let s be the arclength of the curve, so $\dot{\lambda}^2 + \dot{V}^2 = 1$, therefore $\dot{V}$ implies $|DV(0,1)| = 0$ and $\dot{\lambda} = 0$ implies $|DP(0,1)| = 0$.

A.3 Method of Poincare

Weierstrass's second variation (equation A.22) is a simplified version of the two dimensional version of the second variation,

$$\delta^2 J = \int_0^1 \zeta \cdot S(\zeta) dt \tag{A.36}$$

where $S(\zeta)$ is defined by

$$S(\zeta) = \begin{bmatrix} \left(-\frac{d}{dt}\left(E_{x'x'}\zeta_1' + E_{xx'}\zeta_1\right) + E_{xx'}\zeta_1' + E_{xx}\zeta_1\right) \\ \left(-\frac{d}{dt}\left(E_{y'y'}\zeta_2' + E_{yy'}\zeta_2\right) + E_{yy'}\zeta_2' + E_{yy}\zeta_2\right) \end{bmatrix}, \tag{A.37}$$

and $\zeta \equiv [\zeta_1, \zeta_2]$ where $zeta_1$ is the disturbance in the x direction and ζ_2 is the disturbance in the y direction. Note that S is a Sturm Liouville operator. The volume constraint applied to the disturbance is

$$0 = \int_0^1 \zeta \cdot T dt \tag{A.38}$$

where

$$T \equiv \begin{bmatrix} \left(G_x - \frac{d}{dt}(G_{x'})\right) \\ \left(G_y - \frac{d}{dt}(G_{y'})\right) \end{bmatrix} \tag{A.39}$$

For the unconstrained stability the stability changes when the eigenvalue problem

$$S(\zeta) = \rho\zeta \tag{A.40}$$

has a zero eigenvalue (ρ).

For the constrained problem the stability changes when the eigenvalue problem

$$\begin{aligned} &S(\zeta) = \rho T \\ &\int_0^1 \zeta \cdot T dt = 0 \end{aligned} \tag{A.41a}$$

has a zero eigenvalue.

Differentiating the Euler-Lagrange equation with respect to s and taking the inner product gives

$$\int_0^1 \dot{\zeta} \cdot S(\zeta) dt = \dot{\lambda} \dot{V} \tag{A.42}$$

Due to equation A.40 if there is a pressure turning point ($\dot{\lambda} = 0$) then the unconstrained stability must change. Due to equation A.41 the constrained stability will change when equation A.42 satisfies the volume constraint, that is when $\dot{V} = 0$. Equation A.42 and equation A.35 are identical.

The change of stability of these turning points can be read off the distinguished diagram [66]. For counter-clockwise turning points a stable direction is lost, whereas for clockwise turning points a stable direction is gained. This is derived in [66] by assuming we know the eigenvector ζ of S when a turning point occurs and then add a vector perpendicular to this vector. Taking appropriate inner products gives the result on the change in sign of the eigenvalue.

A.4 Equivalence of Weierstrass and Poincare results

The section on the Weierstrass stability gave the change in stability, but unlike the Poincare method it did not give the change in stability. Here the change in stability is shown to be the same for both methods for a one-dimensional problem (t is a constant value).

The first variation gives

$$\frac{dE}{dx_1} \equiv E_1 = 0 \quad \frac{dE}{dx_2} \equiv E_2 = 0 \ . \tag{A.43}$$

the second variation depends on the determinant of the two matrices DP and DV, which, for the one dimensional problem are

$$DP = \begin{bmatrix} E_{11} & E_{12} \\ E_{12} & E_{22} \end{bmatrix} \quad DV = \begin{bmatrix} E_{11} & E_{12} & V_1 \\ E_{12} & E_{22} & V_2 \\ V_1 & V_2 & 0 \end{bmatrix} . \tag{A.44}$$

Differentiating the first variation with respect to the arclength (s) in the distinguished diagram

$$\begin{bmatrix} E_{11} & E_{12} & V_1 \\ E_{12} & E_{22} & V_2 \\ V_1 & V_2 & 0 \end{bmatrix} \begin{bmatrix} \dot{x_1} \\ \dot{x_2} \\ -\dot{\lambda} \end{bmatrix} = \begin{bmatrix} 0 \\ 0 \\ \dot{V} \end{bmatrix}$$

By Cramer's rule $\dot{\lambda} \begin{vmatrix} E_{11} & E_{12} & V_1 \\ E_{12} & E_{22} & V_2 \\ V_1 & V_2 & 0 \end{vmatrix} = \dot{V} \begin{vmatrix} E_{11} & E_{12} \\ E_{12} & E_{22} \end{vmatrix}$ or $-\dot{\lambda}|DV| = \dot{V}|DP|$ Differentiating this expression with respect to arclength gives

$$-\ddot{\lambda}|DV| - \dot{\lambda}\dot{\overline{|DV|}} = \dot{V}\dot{\overline{|DP|}} + \ddot{V}|DP|$$

This relation allows the recovery of the Poincare results from the Weierstrass method. This equation can be re-arranged in a form appropriate for the given turning point:

- For a constant force turning point $\dot{\overline{|DP|}} = -\frac{\ddot{\lambda}|DV|}{\dot{V}}$
- For a constant length turning point $\dot{\overline{|DV|}} = -\frac{\ddot{V}|DP|}{\dot{\lambda}}$.

These expressions can be related to the invariants, of order one less than the determinant, of the DV and DP matrices. First we use the relations that tell us the change of stability for an $n \times n$ matrix when $I_n = 0$

I_{n-1}	+	+	-	-
$\dot{I}_n$	-	+	-	+
Stability	lose	gain	gain	lose

We can relate these invariants to the above relations using the two properties found through algebra:

1.) When $|DP| = 0$ then $I(DP)III(DV) = -(V_2E_{11}+E_{12}V_1)^2-(V_2E_{12}+E_{22}V_1)^2 < 0$

2.) When $|DV| = 0$ then $II(DP)II(DV) = (E_{11}V_2 - E_{12}V_1)^2 + (E_{22}V_1 - E_{12}V_2)^2 + (E_{11}E_{22} - E_{12}^2)^2 > 0$

These equations let us determine the change of stability at turning points. The results for constant pressure turning points is shown in figure A.2. The result for constant volume turning points is shown in figure A.3. These results match those [66].

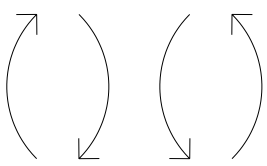

$\ddot{\lambda}$	+	-	+	-
$\dot{V}$	+	-	-	+
$\|DV\|$	+-	+-	+-	+-
$I(DP)$	-+	-+	-+	-+
$\dot{\overline{\|DP\|}} = -\frac{\ddot{\lambda}\|DV\|}{\dot{V}}$	-+	-+	+-	+-
Stability	gain	gain	lose	lose

Figure A.2: Change in stability for constant pressure turning points

				
$\ddot{V}$	+	-	+	-
$\dot{\lambda}$	+	-	-	+
$\lvert DP \rvert$	+-	+-	+-	+-
$II(DV)$	+-	+-	+-	+-
$\dot{\overline{\lvert DV \rvert}} = -\frac{\ddot{V}\lvert DP \rvert}{\dot{\lambda}}$	-+	-+	+-	+-
Stability	lose	lose	gain	gain

Figure A.3: Change in stability for constant volume turning points

APPENDIX B

EXAMPLE OF A COMPLETE TO RING NETWORK DEFORMATION

As an example, consider the homotopy of $N = 4$ networks $r\mathbf{C} + (1-r)\mathbf{R}$, where the network is complete when $r = 1$ and ring when $r = 0$, as illustrated in Fig B.1. Here the connectivity matrix is

$$c_{ij} = \begin{pmatrix} 0 & 1 & r & 1 \\ 1 & 0 & 1 & r \\ r & 1 & 0 & 1 \\ 1 & r & 1 & 0 \end{pmatrix} \tag{B.1}$$

and the unisignant matrix is

$$U_{ij} = \begin{pmatrix} 2+r & -1 & -r \\ -1 & 2+r & -1 \\ -r & -1 & 2+r \end{pmatrix}. \tag{B.2}$$

It is confirmed that the determinant of the unisignant matrix is positive

$$det(U_{ij}) = 4(r+1)^2 > 0. \tag{B.3}$$

The matrix tree theorem holds, since the ring network contains four spanning trees, and the complete network sixteen [46].

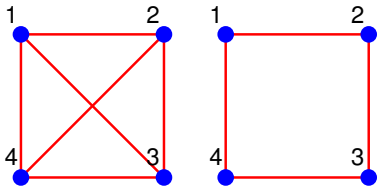

Figure B.1: Complete and ring networks for $N = 4$.

APPENDIX C

NUMBER OF FIXED POINTS

Let $V_S < 1$ be the volume of the n_S small drops and $V_L > 1$ for all $N - n_S = n_L$ large drops. Because all small drops cannot be a fixed point, we consider only $1 \leq n_L \leq N$. The dimensionless height $h = \tilde{H}/\tilde{B}$ (see figure 2.2) is introduced as a parameter of the variables,

$$P = 4/(h + 1/h) \tag{C.1}$$

$$V = h(h^2 + 3)/4. \tag{C.2}$$

For a fixed point, the pressures of all the drops must be equal, hence $P(V_S) = P(V_L)$, thus $h_S = 1/h_L$ where $0 < h_S < 1$ and $1 < h_L$. A super-hemispherical average volume constraint must also be satisfied, $(n_S/N)V_S + (n_L/N)V_L = V_T/N = \overline{V}$ for any $\overline{V} > 1$. In terms of h_L this can be expressed as

$$4N\overline{V} = f(h_L) = (N - n_L)(3h_L^{-1} + h_L^{-3}) + n_L(3h_L + h_L^3) \tag{C.3}$$

Notice that $f(1) = 4N$ and $f(+\infty) = +\infty$. Also $\frac{df}{dh} = 3(1+h_L^2)(n_L - (N-n_L)h_L^{-4})$, so the points of zero slope are $h_L = \pm\sqrt[4]{N/n_L - 1}$. When $1 \leq n_L \leq N/2$ then f decreases until it reaches $h_L = \sqrt[4]{N/n_L - 1}$ after which it strictly increases to infinity, thus there is only one solution to equation C.3. If $N/2 < n_L \leq N$ then f strictly increases from $4N$ to infinity – again there is only one value of h_L for which equation C.3 holds.

APPENDIX D

EIGENVALUES AND EIGENVECTORS OF THE STAR CONFIGURATION

For the star network, consider an arbitrary fixed point with n_L large drops and $n_S = N - n_L$ small drops. Due to the volume constraint there must be at least one large drop; let the center drop be large and label it N. Then, the drops can be labeled so that the Jacobian for the reduced system is

$$J_{jk} = -\frac{\partial^2 E}{\partial V_j \partial V_k} = -H_{ik} \tag{D.1}$$

$$= \begin{bmatrix} -P'_S - P'_L & \dots & & \dots & & \\ \vdots & \ddots & & & & \vdots \\ & & -P'_S - P'_L & & & \\ & & & -2P'_L & & \\ \vdots & & & & \ddots & \vdots \\ & \dots & & & \dots & -2P'_L \end{bmatrix}, \tag{D.2}$$

where all the off diagonal terms are $-P'_L$. There are n_S rows of the first type and $n_L - 1$ rows of the second type.

In order to simplify analytic calculations, the parametric form of pressure is used (2.3) to find $P' = 16(1-h^2)/(3(1+h^2)^3)$. Then, at a fixed point $h_L > 1$, $P'_L = 16(1-h_L^2)/(3((1+h_L^2)^3$ and at $h_L < 1$, $P'_S = -h_L^4 P'_L$.

The Jacobian matrix J_{jk} is symmetric, therefore the eigenvalues are real and the eigenvectors are linearly independent. All $N-1$ eigenvectors can be found by inspection. The $N-1$ eigenvalues for all possible fixed points are broken into three cases according to n_L, as summarized in Table D.1. All values are explicit except for $1 < n_L < N$ where there are two eigenvectors with entries equal q_1 and q_2 and eigenvalues λ_1, λ_2. The values of q and λ are determined by

the system

$$\lambda = -(P'_S + P'_L) - (n_S - 1)P'_L - (n_L - 1)P'_L q \tag{D.3a}$$

$$\lambda q = -n_S P'_L - n_L P'_L q, \tag{D.3b}$$

which can be simplified to a single quadratic equation. Using the super-hemispherical volume constraint $\overline{V} > 1$ it can be shown that there is one positive and one negative solution for λ.

n_L	Amount	Vector	Eigenvalue
$n_L = N$	$N-2$	$[1,0,...,0,-1,0,...,0]^T$	$-P'_L > 0$
	1	$[1,...,1]^T$	$-2P'_L - (N-2)P'_L > 0$
$1 < n_L < N$	$n_S - 1$	$[1,0,...,0,-1,0,...,0]^T$	$-P'_S < 0$
	$n_L - 2$	$[0,...,0,1,0,...,0,-1,0,...,0]^T$	$-P'_L > 0$
	2	$[1,...,1,q,...,q]^T$	$\lambda_1 > 0$, $\lambda_2 < 0$
$n_L = 1$	$N-2$	$[1,0,...,0,-1,0,...,0]^T$	$-P'_S < 0$
	1	$[1,...,1]^T$	$(h_L^4 - (N-1))P'_L < 0$

Table D.1: Eigenvalues and eigen-directions for a fixed point with n_L large drops in the reduced space ($N-1$ components). The vector type and the amount (number) of times that type of vector appears are listed. All eigenvectors of a given type have the same eigenvalue.

Since the linear network in Table 3.1 is also a star network, the listed eigenvector and eigenvalues must coincide with the $N = 3$ results from Table D.1. We verify this as an illustration of the use of the tables. Start with Table D.1 and read off the eigen-directions as $[1,-1]$, $[1,1]$ with eigenvalues $-P'_L$, $-3P'_L$, respectively. Using the volume constraint $0 = dV_1 + dV_2 + dV_3$, the full-space eigen-directions are recovered as $[1,-1,0]$, $[1,1,-2]$. Interchanging the identity of drops $N = 3$ and $N = 2$ (center and right drop exchange labels) yields eigen-directions $[1,0,-1]$, $[1,-2,1]$ from which the triangular reduced space eigen-directions are obtained by the mapping $(dx,dy) = (dV_1 - dV_3, \sqrt{3}dV_2)$, $[2,0]$, $[0,-2\sqrt{3}]$. Finally, normalizing these yields eigenvectors $[1,0]$, $[0,-1]$ with eigenvalues $-P'_L$, $-3P'_L$, respectively.

APPENDIX E

FLOW TYPES IN ADHESION DEVICE

In the low-resistance reservoir limit (i), the resistance through the reservoir is much less than the resistance to flow vertically through the frit $4\mu W/(H_R^3) \ll 2\mu H_F/(B\kappa)$ which is much less than resistance to flow horizontally through the frit $2\mu H_F/(B\kappa) \ll \mu W/(H_F\kappa)$. The liquid travels from a drop vertically through the frit to the reservoir and then through the frit again to another drop. In this case the resistance between drops is dominated by flow vertically through the frit. The resistance is independent of the distance between drops, therefore this type of flow is modeled as a complete network.

The flow travels only through the frit (ii) when the resistance to flow horizontally through the frit is much less than the resistance through the reservoir $\mu W/(H_F\kappa) \ll 4\mu W/(H_R^3)$ or much less than the resistance vertically through the frit $\mu W/(H_F\kappa) \ll 2\mu H_F/(B\kappa)$. Here, the resistance between drops depends on the distance between drops. Koplik [57] has shown that creeping flow through networks of conduits connecting cavities behaves effectively as flow through a porous medium on the large scale, and this is also true for our system (Sec. 4.3.2). For this reason, simulations of this type of flow will be modeled with a linear or square network of conduits.

The experiments can be more complicated than these limiting cases. With a thick frit, flow horizontally through the frit dominates at early times when the large drop distance is less than the thickness of the frit. Thereafter, the flow is dominated by the resistance perpendicular to the frit. A difficulty in fabricating these small-scale device is ensuring that there are no gaps between frit and top plate. Flow within this gap region could be modeled as two dimensional flow

through porous medium, as case (ii); however, the size and permeability of the gap are unknown.

APPENDIX F

REYNOLDS' TRANSPORT THEOREM ON A SURFACE

From Aris [1] (equation 10.12.10) at constant γ we obtain

$$\frac{d}{dt}\int dA = \int \frac{1}{2g}\frac{\partial g}{\partial t} dA + \oint V^{\alpha} m_{\alpha} d\ell \tag{F.1}$$

where g is the discriminant of the first fundamental form in the fixed coordinates, $V^{\alpha} \equiv \frac{du^{\alpha}}{dt}$ is the surface velocity and m_{α} is the unit normal to the curve within the plane. That is, $m_1 \equiv \sqrt{g}\frac{\partial u^2}{\partial s}$ and $m_2 \equiv -\sqrt{g}\frac{\partial u^1}{\partial s}$ where u^{α} are the fixed coordinates and s is the arclength of the curve. Here the Green's theorem on a surface was used (cf. [67]). The time derivative of the discriminant of the first fundamental form is related to the curvature of the interface using the relation from Aris [1] (Exercise 10.41.1)

$$V^{\alpha}{}_{,\alpha} + \frac{1}{2g}\frac{\partial g}{\partial t} = g^{\alpha\beta}\left(\boldsymbol{x}_{\alpha}\frac{d\boldsymbol{x}}{dt}\right)_{,\beta} - 2H\boldsymbol{n}\cdot\frac{d\boldsymbol{x}}{dt} \tag{F.2}$$

where the summation convention in two dimensions has been adopted, the subscripts with commas refer to covarient derivatives (cf. [58] section 70) and H is the arithmetic mean of the principal curvatures (cf. [58] section 41) and $\boldsymbol{n}$ is the outward normal. The relation for the change in area is given by

$$\frac{d}{dt}\int dA = \int g^{\alpha\beta}\left(\boldsymbol{x}_{\alpha}\frac{d\boldsymbol{x}}{dt}\right)_{,\beta} - 2H\boldsymbol{n}\cdot\frac{d\boldsymbol{x}}{dt} - V^{\alpha}{}_{,\alpha}\, dA + \oint V^{\alpha} m_{\alpha} d\ell \tag{F.3}$$

Expanding the total derivative of the surface ($\boldsymbol{x}$) gives

$$\frac{d}{dt}\int dA = \int g^{\alpha\beta}\left(\boldsymbol{x}_{\alpha}\frac{\partial\boldsymbol{x}}{\partial t}\right)_{,\beta} - 2H\boldsymbol{n}\cdot\frac{d\boldsymbol{x}}{dt} dA + \oint V^{\alpha} m_{\alpha} d\ell. \tag{F.4}$$

From the definition of fixed coordinates, a point is fixed in space if its velocity is wholly normal to the surface, therefore $\boldsymbol{x}_{\alpha}\cdot\frac{\partial\boldsymbol{x}}{\partial t} = 0$. The surface velocity and

the normal within the surface can be expressed in the three dimensional space as $\boldsymbol{U} \equiv V^{\alpha}\boldsymbol{x}_{\alpha}$ and $\boldsymbol{m} = m_{\alpha}\boldsymbol{x}_{\beta}g^{\alpha\beta}$. The change in area is then given as

$$\frac{d}{dt}\int dA = \int -2H\boldsymbol{n}\cdot\frac{d\boldsymbol{x}}{dt}dA + \oint \boldsymbol{U}\cdot\boldsymbol{m}d\ell. \tag{F.5}$$

If the surface moves along a plane at a velocity U and we define the angle between the surface and the plane through the enclosed volume to be θ then $\boldsymbol{U}\cdot\boldsymbol{m} = U\cos(\theta)$. The velocity of the surface is $\boldsymbol{v} \equiv \frac{d\boldsymbol{x}}{dt}$. The arithmetic mean of the principle curvatures is defined in terms of the radii of curvatures $2H = -\left(\frac{1}{r_1}+\frac{1}{r_2}\right)$ where the radii of curvature are positive if their centers are within the enclosed volume. The change in area is thus given by

$$\frac{d}{dt}\int dA = \int \left(\frac{1}{r_1}+\frac{1}{r_2}\right)\boldsymbol{n}\cdot\boldsymbol{v}dA + \oint U\cos(\theta)d\ell. \tag{F.6}$$

This agrees with the relation given by Dussan [28] (equation 4).

APPENDIX G

ANALYTIC EVALUATION OF TERMS IN BIM

The following analytic approximation were calculated in order to prevent round-off errors. The notation follows that from Lee [62]. All expressions were calculated using the computer algebra program Maxima.

When $k'^2 \equiv 1 - k^2 < 10^{-8}$ then the integrand for the velocity $\mathbf{C}$ (the double layer) was evaluated as

$$\mathbf{C}_{rr} = \frac{8}{3}\frac{n_r(x_r-\eta_r)^3 + n_z(x_z-\eta_z)(x_r-\eta_r)^2}{C^5 k'^4}\eta_r \tag{G.1}$$

$$\mathbf{C}_{rz} = \frac{8}{3}\frac{n_r(x_r-\eta_r)^2(x_z-\eta_z) + n_z(x_r-\eta_r)(x_z-\eta_z)^2)}{C^5 k'^4}\eta_r \tag{G.2}$$

$$\mathbf{C}_{zr} = \frac{8}{3}\frac{n_r(x_r-\eta_r)^2(x_z-\eta_z) + n_z(x_r-\eta_r)(x_z-\eta_z)^2}{C^5 k'^4}\eta_r \tag{G.3}$$

$$\mathbf{C}_{zz} = \frac{8}{3}\frac{n_r(x_r-\eta_r)(x_z-\eta_z)^2 + n_z(x_z-\eta_z)^3}{C^5 k'^4}\eta_r \tag{G.4}$$

When the point $\boldsymbol{x} \approx \boldsymbol{\eta}$ the following analytic forms were used for the double layer

$$\mathbf{C}_{rr} = \frac{2}{3}\dot{x}_r\ddot{x}_z - \frac{(2\dot{x}_r^2 + 3\dot{x}_z^2)\dot{x}_z}{3x_r} \tag{G.5}$$

$$\mathbf{C}_{rz} = \frac{2}{3}\dot{x}_z\ddot{x}_z + \frac{\dot{x}_r\dot{x}_z^2}{3x_r} \tag{G.6}$$

$$\mathbf{C}_{zr} = \frac{2}{3}\dot{x}_z\ddot{x}_z + \frac{\dot{x}_r\dot{x}_z^2}{3x_r} \tag{G.7}$$

$$\mathbf{C}_{zz} = -\frac{2}{3}\dot{x}_z\ddot{x}_r + \frac{\dot{x}_z^3}{3x_r} \tag{G.8}$$

Analytic evaluations of the single layer were not needed for small k'. However, the integrand of the single layer has a logarithmic singularity, the follow-

ing expressions were used when $\boldsymbol{x} \approx \boldsymbol{\eta}$,

$$\mathbf{B}_{rr} = -2ln(ds) + 2ln(8x_r) - 2 - 2\dot{x}_z^2 \tag{G.9}$$

$$\mathbf{B}_{rz} = 2\dot{x}_r\dot{x}_z \tag{G.10}$$

$$\mathbf{B}_{zr} = 2\dot{x}_r\dot{x}_z \tag{G.11}$$

$$\mathbf{B}_{zz} = -2ln(ds) + 2ln(8x_r) + 2 + 2\dot{x}_z^2 \tag{G.12}$$

where ds is the arclength along which the analytic integration is done.

BIBLIOGRAPHY

[1] R. Aris. *Vectors, tensors, and the basic equations of fluid mechanics*. Dover Pubns, 1989.

[2] VI Arnold. *Ordinary Differential Equations (Translated and edited by RA Silverman)*.

[3] J.C. Berg. *Wettability*. CRC, 1993.

[4] T.D. Blake. The physics of moving wetting lines. *Journal of colloid and interface science*, 299(1):1–13, 2006.

[5] TD Blake, M. Bracke, and YD Shikhmurzaev. Experimental evidence of nonlocal hydrodynamic influence on the dynamic contact angle. *Physics of fluids*, 11:1995, 1999.

[6] TD Blake and JM Haynes. Kinetics of liquid/liquid displacement. *Journal of Colloid and Interface Science*, 30(3):421–423, 1969.

[7] O. Bolza. *Lectures on the calculus of variations*. 1904.

[8] D. Bonn, J. Eggers, J. Indekeu, J. Meunier, and E. Rolley. Wetting and spreading. *Reviews of Modern Physics*, 81(2):739–805, 2009.

[9] A. J. Bray. Theory of phase-ordering kinetics. *Advances in Physics*, 51(2):481–587, 2002.

[10] F. Brochard-Wyart and PG De Gennes. Dynamics of partial wetting. *Advances in Colloid and Interface Science*, 39:1–11, 1992.

[11] L. C. Brown. A new examination of classical coarsening theory. *Acta Metallurgica*, 37(1):71–77, 1989.

[12] J. W. Cahn. Spinodal Decomposition. *Transactions of the metallurgical society of AIME*, 242.

[13] JW Cahn and JE Hilliard. Free energy of a nonuniform system. I. Interface free energy. *J. Chem. Phys*, 28(2):258–267, 1958.

[14] H.B. Callen. *Thermodynamics and an Introduction to Thermostatistics*. Wiley, 1985.

[15] J. Carr. *Applications of centre manifold theory*. Springer, 1981.

[16] MK Chaudhury and MW George. How to make water run uphill. *Science*, 256(5063):1539–1541, 1992.

[17] W.K. Chen. On unisignants and their evaluation. *SIAM Journal on Applied Mathematics*, 16(3):603–619, 1968.

[18] C.C. Chicone. *Ordinary differential equations with applications*. Springer Verlag, 2006.

[19] C.H. Choi, K.J.A. Westin, and K.S. Breuer. Apparent slip flows in hydrophilic and hydrophobic microchannels. *Physics of fluids*, 15:2897, 2003.

[20] RG Cox. The dynamics of the spreading of liquids on a solid surface. Part 1. Viscous flow. *Journal of Fluid Mechanics*, 168:169–194, 1986.

[21] S. Daniel, M.K. Chaudhury, and J.C. Chen. Fast drop movements resulting from the phase change on a gradient surface. *Science*, 291(5504):633, 2001.

[22] R.H. Davis. Buoyancy-driven viscous interaction of a rising drop with a smaller trailing drop. *Physics of Fluids*, 11:1016, 1999.

[23] S.H. Davis. Moving contact lines and rivulet instabilities. Part 1. The static rivulet. *Journal of Fluid Mechanics*, 98(02):225–242, 1980.

[24] P.G. de Gennes. Wetting: statics and dynamics. *Reviews of Modern Physics*, 57(3):827–863, 1985.

[25] P.G. Debenedetti. *Metastable liquids: concepts and principles*. Princeton Univ Pr, 1996.

[26] W.M. Deen. *Analysis of transport phenomena*. Oxford University Press New York, 1998.

[27] E.J. Doedel, RC Paffenroth, AR Champneys, TF Fairgrieve, YA Kusnetsov, B. Sandstede, B. Oldeman, XJ Wang, and C. Zhang. AUTO 07P–Continuation and bifurcation software for ordinary differential equations. *Department of Computer Science, Concordia University, Montreal, QC*, 2007.

[28] EB Dussan V. Hydrodynamic stability and instability of fluid systems

with interfaces. *Archive for Rational Mechanics and Analysis*, 57(4):363–379, 1975.

[29] E.B. Dussan V and S.H. Davis. On the motion of a fluid-fluid interface along a solid surface. *Journal of Fluid Mechanics*, 65(01):71–95, 1974.

[30] EB Dussan V and SH Davis. Stability in systems with moving contact lines. *Journal of Fluid Mechanics*, 173:115–130, 1986.

[31] EB Dussan V, E. Ramé, and S. Garoff. On identifying the appropriate boundary conditions at a moving contact line: an experimental investigation. *Journal of Fluid Mechanics*, 230:97–116, 1991.

[32] A. Einstein. Über die von der molekularkinetischen Theorie der Wärme geforderte Bewegung von in ruhenden Flüssigkeiten suspendierten Teilchen. *Annalen der physik*, 322(8):549–560, 1905.

[33] T. Eisner and D. J. Aneshansley. Defense by foot adhesion in a beetle (Hemisphaerota cyanea). *Proceedings of the National Academy of Sciences of the United States of America*, 97(12):6568–6573, 2000.

[34] S. Esedoḡlu and D. Slepčev. Refined upper bounds on the coarsening rate of discrete, ill-posed diffusion equations. *Nonlinearity*, 21:2759–2776, 2008.

[35] S. Fordham. On the calculation of surface tension from measurements of pendant drops. *Proceedings of the Royal Society of London. Series A, Mathematical and Physical Sciences*, 194(1036):1–16, 1948.

[36] G. Gilboa, N. Sochen, and Y.Y. Zeevi. Forward-and-backward diffusion processes for adaptive image enhancement and denoising. *Image Processing, IEEE Transactions on*, 11(7):689–703, 2002.

[37] RD Gillette and DC Dyson. Stability of fluid interfaces of revolution between equal solid circular plates. *The Chemical Engineering Journal*, 2(1):44–54, 1971.

[38] RD Gillette and DC Dyson. Stability of static configurations with applications to the theory of capillarity. *Archive for Rational Mechanics and Analysis*, 53(2):150–177, 1974.

[39] K. B. Glasner and T. P. Witelski. Coarsening dynamics of dewetting films. *Physical review E*, 67(1):16302, 2003.

[40] M. Golubitsky and I. Stewart. *The symmetry perspective*. Birkhäuser, 2002.

[41] M. B. Gratton and T. P. Witelski. Coarsening of unstable thin films subject to gravity. *Physical Review E*, 77(1):16301, 2008.

[42] M. B. Gratton and T. P. Witelski. Transient and self-similar dynamics in thin film coarsening. *Physica D: Nonlinear Phenomena*, 238(23-24):2380–2394, 2009.

[43] J. Guckenheimer and P. Holmes. *Nonlinear Oscillations, Dynamical Systems, and Bifurcations of Vector Fields (Applied Mathematical Sciences vol 42)*.

[44] N.G. Hadjiconstantinou. Hybrid atomistic-continuum formulations and the moving contact-line problem. *Journal of Computational Physics*, 154(2):245–265, 1999.

[45] P.J. Haley Jr and M.J. Miksis. Dissipation and contact-line motion. *Physics of Fluids A: Fluid Dynamics*, 3:487, 1991.

[46] F. Harary. *Graph Theory. 1971*. Addison-Wesley, Reading, MA.

[47] J. Harris, J.W. Harris, and H. Stöcker. *Handbook of mathematics and computational science*. Springer Verlag, 1998.

[48] M.W. Hirsch and S. Smale. *Differential equations, dynamical systems, and linear algebra*. Academic Press, 1974.

[49] LM Hocking and AD Rivers. The spreading of a drop by capillary action. *Journal of Fluid Mechanics*, 121:425–442, 1982.

[50] W. Howe. *Die Rotations-flächen welche bei vorgeschriebener Flächengrosse ein möglichst grosses oder kleines Volumen enthalten*. C. Koepsel, 1887.

[51] C. Huh and SG Mason. The steady movement of a liquid meniscus in a capillary tube. *Journal of fluid mechanics*, 81(03):401–419, 1977.

[52] C. Huh and LE Scriven. Hydrodynamic model of steady movement of a solid/liquid/fluid contact line. *Journal of Colloid and Interface Science*, 35(1):85–101, 1971.

[53] DD Joseph. Stability of fluid motions II. *Springer Tracts in Natural Philosophy*, 28:274, 1976.

[54] G. Kirchhoff. Über die Auflösung der Gleichungen, auf welche man bei der Untersuchung der linearen Vertheilung galvanischer Ströme geführt wird. *Annalen der Physik*, 148(12):497–508, 1847.

[55] N. Kissi, JM Piau, P. Attané, and G. Turrel. Shear rheometry of polydimethylsiloxanes. Master curves and testing of Gleissle and Yamamoto relations. *Rheologica Acta*, 32(3):293–310, 1993.

[56] R. V. Kohn and F. Otto. Upper bounds on coarsening rates. *Communications in Mathematical Physics*, 229(3):375–395, 2002.

[57] J. Koplik. Creeping flow in two-dimensional networks. *Journal of Fluid Mechanics*, 119:219–247, 1982.

[58] E. Kreyszig. Differential geometry, 1991.

[59] OA Ladyzhenskaya. The mathematical theory of viscous incompressible flow. 1969.

[60] H. Lamb. *Hydrodynamics*. Dover, 1945.

[61] L.G. Leal. *Laminar flow and convective transport processes: scaling principles and asymptotic analysis*. Butterworth-Heinemann, 1992.

[62] SH Lee and LG Leal. The motion of a sphere in the presence of a deformable interface:: II. A numerical study of the translation of a sphere normal to an interface. *Journal of Colloid and Interface Science*, 87(1):81–106, 1982.

[63] I. M. Lifshitz and V. V. Slyozov. The kinetics of precipitation from supersaturated solid solutions. *Journal of Physics and Chemistry of Solids*, 19(1-2):35–50, 1961.

[64] J. R. Lister, J. M. Rallison, and S. J. Rees. The nonlinear dynamics of pendent drops on a thin film coating the underside of a ceiling. *Journal of Fluid Mechanics*, 647:239–264, 2010.

[65] J. Lowndes. The numerical simulation of the steady movement of a fluid meniscus in a capillary tube. *Journal of Fluid Mechanics*, 101(03):631–646, 1980.

[66] JH Maddocks. Stability and folds. *Archive for Rational mechanics and Analysis*, 99(4):301–328, 1987.

[67] A.J. McConnell. Applications of the absolute differential calculus. *Bull. Amer. Math. Soc*, 38(Part 1):615–616, 1932.

[68] R.I. McLachlan, GRW Quispel, and N. Robidoux. Geometric integration using discrete gradients. *Philosophical Transactions of the Royal Society of London. Series A: Mathematical, Physical and Engineering Sciences*, 357(1754):1021, 1999.

[69] D. Meer, K. Weele, and D. Lohse. Coarsening dynamics in a vibrofluidized compartmentalized granular gas. *Journal of Statistical Mechanics: Theory and Experiment*, 2004:P04004, 2004.

[70] I. Meyvantsson, J. W. Warrick, S. Hayes, A. Skoien, and D. J. Beebe. Automated cell culture in high density tubeless microfluidic device arrays. *Lab on a Chip*, 8(5):717–724, 2008.

[71] M. Morse. *Introduction to Analysis in the Large*. Institute for Advanced Study, 1951.

[72] T. Muir. *A Treatise on the Theory of Determinants. 1960*. Dover, New York.

[73] I. Müller and P. Strehlow. *Rubber and rubber balloons: paradigms of thermodynamics*. Springer Verlag, 2004.

[74] C. Navier. Mémoire sur les lois du mouvement des fluids Mem. *Acad. Sci. Inst. Fr*, 6(2):389–440, 1823.

[75] C. Neto, VSJ Craig, and DRM Williams. Evidence of shear-dependent boundary slip in newtonian liquids. *The European Physical Journal E: Soft Matter and Biological Physics*, 12:71–74, 2003.

[76] M. Nitsche, HD Ceniceros, AL Karniala, and S. Naderi. High order quadratures for the evaluation of interfacial velocities in axi-symmetric Stokes flows. *Journal of Computational Physics*, 229(18):6318–6342, 2010.

[77] F.K.G. Odqvist. Über die randwertaufgaben der hydrodynamik zäher flüssigkeiten. *Mathematische Zeitschrift*, 32(1):329–375, 1930.

[78] D. Painter et al. Localization in lattice and continuum models of reinforced random walks 1. *Applied Mathematics Letters*, 16(3):375–381, 2003.

[79] P. Perona and J. Malik. Scale-space and edge detection using anisotropic diffusion. *IEEE Transactions on pattern analysis and machine intelligence*, 12(7):629–639, 1990.

[80] J. Perrin. Mouvement brownien et réalité moléculaire. In *Annales de Chimie et de Physique*, volume 18, 1909.

[81] E. Ramé and S. Garoff. Microscopic and macroscopic dynamic interface shapes and the interpretation of dynamic contact angles. *Journal of colloid and interface science*, 177(1):234–244, 1996.

[82] E. Ramé, S. Garoff, and KR Willson. Characterizing the microscopic physics near moving contact linesusing dynamic contact angle data. *Physical Review E*, 70(3):31608, 2004.

[83] L. Ratke and P. W. Voorhees. *Growth and coarsening*. Springer, 2002.

[84] J.S. Rowlinson and B. Widom. *Molecular theory of capillarity*. Dover Pubns, 2002.

[85] B.B. Sauer and G.T. Dee. Molecular weight and temperature dependence of polymer surface tension: comparison of experiment with theory. *Macromolecules*, 24(8):2124–2126, 1991.

[86] L.A. Segel and GH Handelman. Mathematics applied to continuum mechanics. 1977.

[87] Y.D. Shikhmurzaev. Moving contact lines in liquid/liquid/solid systems. *Journal of Fluid Mechanics*, 334:211–249, 1997.

[88] E. D. Siggia. Late stages of spinodal decomposition in binary mixtures. *Physical Review A*, 20(2):595–605, 1979.

[89] J.C. Slattery, L. Sagis, and E.S. Oh. *Interfacial transport phenomena*. Springer Verlag, 2007.

[90] S. H. Strogatz. *Nonlinear dynamics and chaos: With applications to physics, biology, chemistry, and engineering*. Westview Pr, 1994.

[91] U. Thiele, M. G. Velarde, K. Neuffer, M. Bestehorn, and Y. Pomeau. Sliding drops in the diffuse interface model coupled to hydrodynamics. *Physical Review E*, 64(6):61601, 2001.

[92] C. Truesdell. *A first course in rational continuum mechanics: General concepts*. Academic Pr, 1991.

[93] J. Van Brakel. Pore space models for transport phenomena in porous media review and evaluation with special emphasis on capillary liquid transport. *Powder technology*, 11(3):205–236, 1975.

[94] D. Van Der Meer, K. Van Der Weele, and D. Lohse. Sudden collapse of a granular cluster. *Physical Review Letters*, 88(17):174302, 2002.

[95] H. B. van Lengerich, M. J. Vogel, and P. H. Steen. Dynamics and stability of volume-scavenging drop arrays: Coarsening by capillarity. *Physica D: Nonlinear Phenomena*, 238(5):531–539, 2009.

[96] M.J. Vogel, P. Ehrhard, and P.H. Steen. The electroosmotic droplet switch: Countering capillarity with electrokinetics. *Proceedings of the National Academy of Sciences of the United States of America*, 102(34):11974, 2005.

[97] M.J. Vogel and P.H. Steen. Capillarity-based switchable adhesion. *Proceedings of the National Academy of Sciences*, 107(8):3377, 2010.

[98] O.V. Voinov. Hydrodynamics of wetting. *Fluid Dynamics*, 11(5):714–721, 1976.

[99] O.V. Voinov. Motion of line of contact of three phases on a solid: thermodynamics and asymtotic theory* 1. *International Journal of Multiphase Flow*, 21(5):801–816, 1995.

[100] O.V. Voinov. Wetting: Inverse dynamic problem and equations for microscopic parameters. *Journal of Colloid and Interface Science*, 226(1):5–15, 2000.

[101] K. Vorvolakos and M.K. Chaudhury. The effects of molecular weight and temperature on the kinetic friction of silicone rubbers. *Langmuir*, 19(17):6778–6787, 2003.

[102] C. Wagner. Theorie der alterung von niederschlägen durch umlösen

(Ostwald-reifung). *Zeitschrift für Elektrochemie, Berichte der Bunsengesellschaft für physikalische Chemie*, 65(7-8):581–591, 1961.

[103] G.M. Walker and D.J. Beebe. A passive pumping method for microfluidic devices. *Lab on a Chip*, 2(3):131–134, 2002.

[104] DE Weidner and LW Schwartz. Contact-line motion of shear-thinning liquids. *Physics of Fluids*, 6:3535, 1994.

[105] S.J. Weinstein and K.J. Ruschak. Coating flows. *Annual Review of Fluid Mechanics*, 36(1):29, 2004.

[106] T.P. Witelski, D.G. Schaeffer, and M. Shearer. A discrete model for an ill-posed nonlinear parabolic PDE. *Physica D: Nonlinear Phenomena*, 160(3-4):189–221, 2001.

[107] T. Young. An essay on the cohesion of fluids. *Philosophical Transactions of the Royal Society of London*, 95:65–87, 1805.

[108] GK Youngren and A. Acrivos. Stokes flow past a particle of arbitrary shape: a numerical method of solution. *Journal of fluid Mechanics*, 69(02):377–403, 1975.

[109] C. Zettner and M. Yoda. Particle velocity field measurements in a near-wall flow using evanescent wave illumination. *Experiments in Fluids*, 34(1):115–121, 2003.